EVALUATION OF ELASTIC IMPEDANCE ATTRIBUTES IN OFFSHORE HIGH ISLAND, GULF OF MEXICO

A Thesis

Presented to

the Faculty of the Department of Earth and Atmospheric Sciences

University of Houston

In Partial fulfillment

of the Requirements for the Degree

Master of Science

By

Oladotun Oluwaseun Awosemo

May 2012

EVALUATION OF ELASTIC IMPEDANCE ATTRIBUTES IN OFFSHORE HIGH ISLAND, GULF OF MEXICO

……...

Oladotun Oluwaseun Awosemo

APPROVED:

……

Dr. Fred Hilterman, Advisor

……

Dr. Robert Stewart, Chairman

……

Dr. Evgeny Chesnokov, Member

……

Dean, College of Natural Sciences and Mathematics

ACKNOWLEDGEMENTS

My special thanks go to God Almighty for his provision, gift of life, and strength during the course of my study. My sincere appreciation goes to my advisor, Dr. Fred Hilterman for his advice, patience, unequalled support, and assistance throughout the period of this research.

I would also like to thank the chairman of my committee, Dr. Robert Stewart, and Dr. Evgeny Chesnokov for their guidance, technical support, and encouragement. I really appreciate the assistance given to me by Dave Reynolds of Fairfieldnodal Industries during the period of this research. I acknowledge all the professors whose classes I took and which enabled me to carry out this research. I really appreciate all the members of my family; my dad, Mr. Felix Awosemo (late), who I dedicate this thesis to; my mum, Mrs. Bosede Awosemo; my siblings, Dr. Ronke Awosemo, Ayo, Toyin, and Lolade, and my uncle, Dr. Segun Awosemo, for their financial and moral support during the period of my study at University of Houston.

I am very grateful for the help rendered by Dr. Haitao Ren, Dr. Gboyega Ayeni, Dr. Sunday Amoyedo, Afolabi Babalola, Charles Inyang, and Olumide Ibikunle during the period of this research and preparation for my thesis defense. For all those whose names I did not mention, it wouldn't have been possible without you all.

EVALUATION OF ELASTIC IMPEDANCE ATTRIBUTES IN OFFSHORE HIGH ISLAND, GULF OF MEXICO

An Abstract of a Thesis

Presented to

the Faculty of the Department of Earth and Atmospheric Sciences

University of Houston

In Partial Fulfillment

of the Requirements for the Degree

Master of Science

By

Oladotun Oluwaseun Awosemo

May 2012

ABSTRACT

In certain areas, seismic AVO alone is not sufficient for interpretative purposes. This necessitates the use of other seismic attributes. The High Island Field, a Tertiary basin in the Gulf of Mexico, has values of acoustic impedance for shale and gas-saturated sands that are approximately equal. Conventional 3-D seismic data has had limited success in detecting hydrocarbons in this area. Also, synthetic seismograms are difficult if not impossible to tie to seismic data. To solve these problems, I employed the elastic impedance and extended elastic impedance attributes. Results from this research show significant amplitude increase with offset for a gas-saturated reservoir as compared to brine-saturated reservoir. The elastic impedance volume derived from the far-angle stack delineates the reservoir better than the elastic impedance volume from the near-angle stack. With respect to reservoir characterization, the five seismic attributes (V_p/V_s, bulk modulus, shear modulus, Lamé, and shear impedance) generated from the extended elastic impedance inversion helped to determine the lithology and predict the pore-fluid type of the reservoir. In conclusion, the use of additional seismic attributes (elastic impedance and extended elastic impedance) helps to achieve a better reservoir characterization especially in a Class 2 environment.

TABLE OF CONTENTS

LIST OF FIGURES

CHAPTER 1

INTRODUCTION

1.1 Background

Various interpretation techniques have been published on the use of seismic amplitude for reservoir characterization. These include amplitude-variations-with-offset (AVO) and seismic attribute analysis. Large reflection amplitudes known as "bright spots" were recognized in the early 1970s as potential hydrocarbon indicators. In 1973, the Geophysical Society of Houston organized a symposium on direct hydrocarbon indicators, and numerous field examples and theoretical synthetics were presented that tied seismic amplitude to hydrocarbon-charged reservoirs. The bright spot technology of the 1970s established the first era of seismic amplitude interpretation for the estimation of a reservoir's composition (Hilterman, 2001). The use of these bright spots or any kinds of amplitude anomalies is based on the premise that the introduction of gas or high GOR oil to a porous sand unit generally decreases the reservoir's acoustic impedance relative to the surrounding formations. However, bright spots may also be caused by the presence of unusual lithologies such as coal, over-pressured shale, and high-porosity sand (Sen, 2006).

On the petrophysical side, Domenico (1976) considered the effect of a brine-gas mixture on the P-wave velocity of an unconsolidated sand reservoir. He concluded that unconsolidated reservoirs encased in shale usually result in a large increase in seismic reflection amplitude when gas saturated, but the reflection amplitude appeared to be non-linear with respect to water saturation. From this early work, the conclusion was drawn that amplitude is not always a sensitive estimator of gas saturation. Ostrander (1984) introduced the AVO theory and he drew two basic conclusions: (1) Poisson's ratio has a strong influence on changes in reflection coefficient as a function of angle of incidence; and (2) analysis of seismic reflection amplitude

versus shot-to-group offset can in many cases distinguish between gas-related amplitude anomalies and other types of amplitude anomalies. This created a new avenue of examining pre-stack amplitude data for estimating pore-fluid content, lithology, and gas saturation. As seismic amplitude depends on changes in velocity, density and Poisson's ratio across a reflection boundary, AVO is often used in the detection of gas since gas generally decreases Poisson's ratio which normally increases the reflection magnitude with offset/angle (Sheriff, 2002). AVO has proven to be more effective at reducing exploration risk than relying on structural information alone. While an AVO anomaly associated with an amplitude increase with offset is often associated with a hydrocarbon reservoir, this is not always the case. Hydrocarbon-related "AVO anomalies" and brine-saturated "background" rocks may show increasing or decreasing amplitude with offset (Castagna and Swan, 1997).

1.2 Classes of AVO Signatures

Zoeppritz (1919) introduced the reflection-coefficient equations as a function of incident angle, which are the basis of AVO technology. The Zoeppritz equations are normally cast in a 4-by-4 matrix that involves the rock properties of the two media around the boundary, the reflected and transmitted angles and the reflected and transmitted amplitude ratios. Rutherford and Williams (1989) classified the various AVO trends as they vary with increasing incident angle for the top of gas-saturated reservoirs. Based on field studies, they developed an AVO anomaly classification scheme for gas-saturated reservoirs. The Rutherford and Williams classification is:

Class 1. Gas-sand reservoir has larger impedance than the impedance of the encasing shale. Typically, normal-incident values (NI) are greater than +0.03. Class 1 seismic anomalies

normally have the largest change of amplitude with increasing incident angle, that is, they have the largest AVO gradient.

Class 2. Gas-sand reservoir has nearly the same impedance as the encasing shale. NI typically ranges between ±0.03.

Class 3. Gas-sand reservoir has lower impedance than the encasing shale. NI is normally less than -0.03.

Rutherford and Williams also indicated that the slope of the reflection-coefficient curve is normally negative for all classes and the magnitude of the gradient decreases from Class 1 to Class 3 anomalies. The gradient for Class 3 AVO anomalies is normally flat so that the stack is a robust estimate of NI (Hendrickson, 1999). Castagna et al. (1998) added Class 4 to the Rutherford and Williams set. They concluded that certain Class 3 gas-saturated anomalies have slowly decreasing amplitudes with offset and may even reverse polarity within the CDP gather. It is a reservoir with a negative AVO intercept and positive AVO gradient. Their classification demonstrates that reflection coefficients do not always have negative gradients for gas sands. However, they however cautioned that the AVO gradient for a Class 4 brine-saturated sand may be almost identical to the AVO gradient from a Class 4 gas-saturated sand, hence the gas may be difficult to detect by partial offset stacks.

1.2.1 Class 2 AVO Signature

The hydrocarbon-charged reservoirs that I am studying are Tertiary sediments, which as will be demonstrated later, typically exhibit an AVO Class 2 signature. The reservoir sand is characterized by acoustic impedance values that are approximately equal to that of the encasing shale medium and the relative reflection amplitude is large on the far offsets when compared to the near offsets. The Class 2 sand formations are generally moderately compacted and consolidated (Rutherford and Williams, 1989). The normal incident reflection coefficient of a Class 2 sand is usually close to zero, and large fractional changes in reflectivity from near to far offset can occur and this enhances the discrimination of pore fluid in these sand formations. The gradients associated with Class 2 sand are usually large in magnitude but are generally less than those of Class 1 sand. The small-offset reflectivity from a Class 2 sand formation is close to zero and is often undetectable in the presence of noise. In some cases, the reflections seem to suddenly appear at larger offsets when the reflection amplitudes rise above the noise level (Rutherford and Williams, 1989).

Hilterman (2001) observed the following properties exhibited by Class 2 anomalies:

1. "There is little indication of the gas sand on the near-angle stack.
2. The gas sand event increases amplitude with increasing angle.
3. The gas sand event may or may not be evident on the full stack, depending on the far-angle amplitude contribution to the stack.
4. Wavelet character on the stack may or may not be trough-peak for a hydrocarbon-charged thin bed.
5. Wavelet character is trough-peak on the far-angle stack.
6. Inferences about lithology are contained in the amplitude variation with incident angle.

7. AVO alone, unless carefully calibrated, cannot unambiguously distinguish a clean wet sand from a gas sand, because both have similar (increasing) behavior with offset".

1.3 Applications of AVO

The relationship between rock properties and reflection amplitude is not obvious from the Zoeppritz equations. Koefoed (1955) provided insight when he related Poisson's ratio to the amplitude of the reflected P-wave (PP) as a function of the incident angle. In essence, Koefoed inferred that changing Poisson's ratio was equivalent to changing lithology, although he did not mention changes in pore fluid content. In 1961, Bortfeld presented linear approximations of Zoeppritz's equations that made it easy to relate seismic amplitude to rock properties. Other approximations to the PP Zoeppritz equation have been developed that are of the type $R(\theta) = A + B\sin^2\theta + C\sin^2\theta\tan^2\theta$, where A is NI, B is a slope of the amplitude, and C is the amplitude curvature. There are three linear approximations often referenced in the AVO literature. The authors are Aki and Richards (1980), Shuey (1985) and Smith and Gidlow (1987). For ease in relating rock properties to AVO, Verm and Hilterman (1995) modified Shuey's equation to

$$RC(\theta) \approx NI.\cos^2\theta + PR.\sin^2\theta, \qquad 1.1$$

where:

NI = Normal incident reflectivity = $(\rho_2 v_2 - \rho_1 v_1)/(\rho_2 v_2 + \rho_1 v_1)$,

PR = Poisson's reflectivity = $(\sigma_2 - \sigma_1)/(1-\sigma_{avg})^2$;

$\sigma_{avg} = (\sigma_2 + \sigma_1)/2$, and

ρ, v, and σ are density, P-wave velocity, and Poisson's ratio respectively. The numbers 1 and 2 refer to the upper and lower media respectively.

With this modified form of Shuey's equation, it is easy to note that the seismic amplitude at large incident angles is influenced by Poisson's ratio, the same concept Koefoed suggested in 1955.

In an AVO inversion of a CMP gather, Smith and Gidlow's linear approximation equation yields estimates of NIP and NIS, where NIS is the shear-wave normal incidence and NIP is the same as NI. NIS has the same functional relationship to rock properties as NIP but with the S-wave velocity replacing the P-wave velocity. From NIP and NIS, Smith and Gidlow introduced a new attribute called the fluid factor, which theoretically for hydrocarbon reflections is related to the difference in reflection amplitude between a gas-saturated and brine-saturated reservoir [NIP(gas saturated) – NIP(brine saturated)] (Hilterman, 2001). Other authors have extended Smith and Gidlow's theory to suggest that estimates of water saturation (Sw) are possible (Berryman et al., 2002 and Li et al., 2005). Russell et al., (2003) considered AVO from the Gassmann perspective by combining basic rock physics and Smith and Gidlow's AVO inversion to show fluid discrimination is possible with pre-stack seismic data. However, a low-frequency trend of the rock properties was required during inversion.

Zimmerman and Duran (1992) introduced the Seismic Range Equation (SRE) for AVO analysis to detect low-gas saturation (fizz). Their result showed that AVO can be used to distinguish amplitude anomalies caused by gas sands from those caused by brine sands, but they concluded that SRE is not a useful tool to distinguish low-gas saturation from economic gas saturation since their seismic responses are indistinguishable.

With both negative and positive successes for discriminating full-gas saturation from fizz reported in the literature, the question, "Can AVO determine fizz from economic gas saturation?" is still an active research topic. Various studies have been carried out especially in the deep-water Gulf of Mexico, where a number of wells have been classified as dry holes because they encountered low-gas saturated reservoirs. In their deep-water study, Hilterman and Liang (2003)

noted that AVO alone could not discriminate fizz-saturated reservoirs from economic gas-saturated reservoirs since fizz can have an identical AVO response to a fully charged reservoir with less porosity. They suggested rock-property calibrations are required to determine saturation. In a continuation of this study, Zhou et al. (2005) developed two transforms from a rock-property database provided by Geophysical Development Corporation. Zhou's lithology transform utilizes a relationship between the 30-degree reflection co-efficient and normal incidence (NI). The second transform, the pore-fluid transform, expresses NI for sands with different gas saturations in terms of the NI of the brine-saturated sand. Another point in Zhou's work is that the seismic amplitude of the prospect is calibrated to the down-dip brine response of the reservoir and in doing so converts the seismic amplitude to its "true" normal-incident equivalent.

Connolly (1999) came up with the idea of Elastic Impedance (EI) which is a generalization of acoustic impedance (AI) for variable incidence angles. It provides a framework to calibrate and invert non zero offset seismic data, just as AI does for zero-offset seismic data. Hydrocarbon zones in Class II and III AVO are known to have lower EI values than AI as EI values decrease with increasing angle. EI is derived from the linear approximation of the Zoeppritz's equations and is a function of P-wave velocity, S-wave velocity, density and incident angles (Connolly, 1999). It was invented to capture potential AVO effects since in some parts of the North Sea; the near traces are highly contaminated with noise, which makes estimates of normal-incident reflectivity difficult (Hilterman, 2001).

Whitcombe et al. (2002) introduced extended elastic impedance (EEI) which is an extension to elastic impedance. EEI provides a maximum discrimination between either fluids or lithologies and it is computed from constant angle seismic sections. EEI helps to approximate several elastic parameters like bulk modulus, shear modulus, shear impedance and Lamé's parameter by using appropriate incident angle values. This leads to the identification of different

areas of EEI space which tend to be good for fluid and lithology imaging (Whitcombe et al., 2002).

1.4 Research Objective

My research objective is to investigate the effectiveness of inverting seismic data to elastic and extended elastic impedances for predicting lithology and pore-fluid especially in areas where the acoustic impedance of shale and gas-saturated sand are approximately equal.

1.5 Available Data

Seismic data used for this research were provided by Fairfield Industries while well-log data were supplied by Geokinetics Inc. The seismic data include: pre-stack migrated CMP gathers (0-42°), and near- (2-15°) and far- (15-42°) angle-stack volumes (Figures 1.1, 1.2 and 1.3) respectively. A full-angle stack (0-42º) was also available. They were acquired and processed by Fairfield Industries using Kirchhoff pre-stack time migration, controlled phase and true amplitude algorithms. The processing steps applied to the raw seismic data are shown in Figure 1.4. The survey area has inlines (ILN) 1786-1965 (increment = 1) and crosslines (XLN) 3876-4382 (increment = 2). Other survey parameters are: inline spacing, 55 ft; crossline spacing, 110 ft; sample rate, 6 ms; and time processed, 7.8 s. The survey covers an area of about 29.3 mi^2 or 75.0 km^2. Well-log curves from 5 wells were available and the curves include: gamma ray, resistivity, P-wave sonic, pseudo S-wave sonic, density, caliper, neutron porosity, and spontaneous potential (SP). Check-shot data were also available for this research. The software available for this research included Schlumberger Petrel for amplitude extraction and three-dimensional (3D) seismic interpretation, Petroseismic TIPS for detailed AVO modeling,

Hampson-Russell (HR) Elog for log analysis, HR AVO for AVO modeling and analysis, HR PROMC for horizon attributes extraction and HR STRATA for seismic inversions.

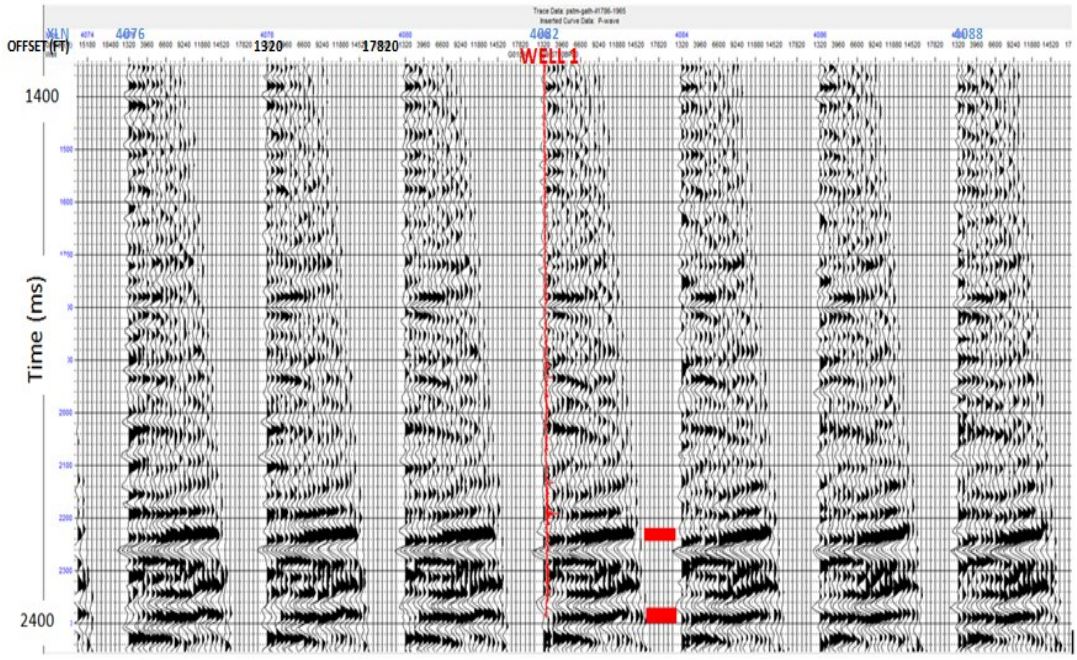

Figure 1.1: CMP gathers near Well 1 location (Inserted red curve is the P-wave sonic log while the red rectangles represent the gas intervals)

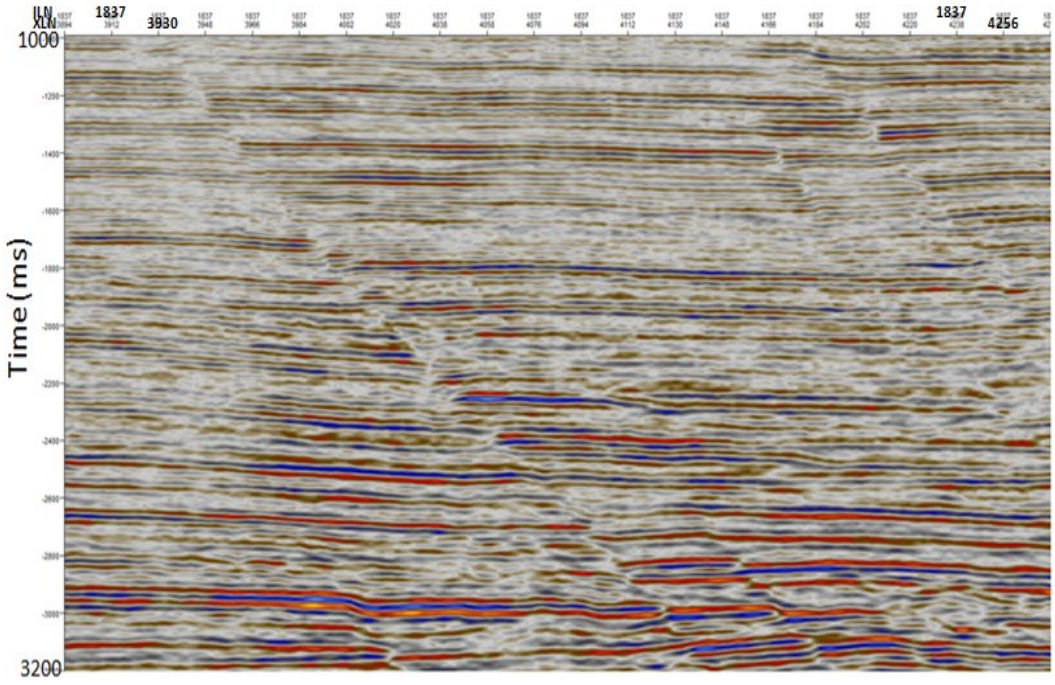

Figure 1.2: Near-angle stack (2-15°) between 1.0 s and 3.2 s

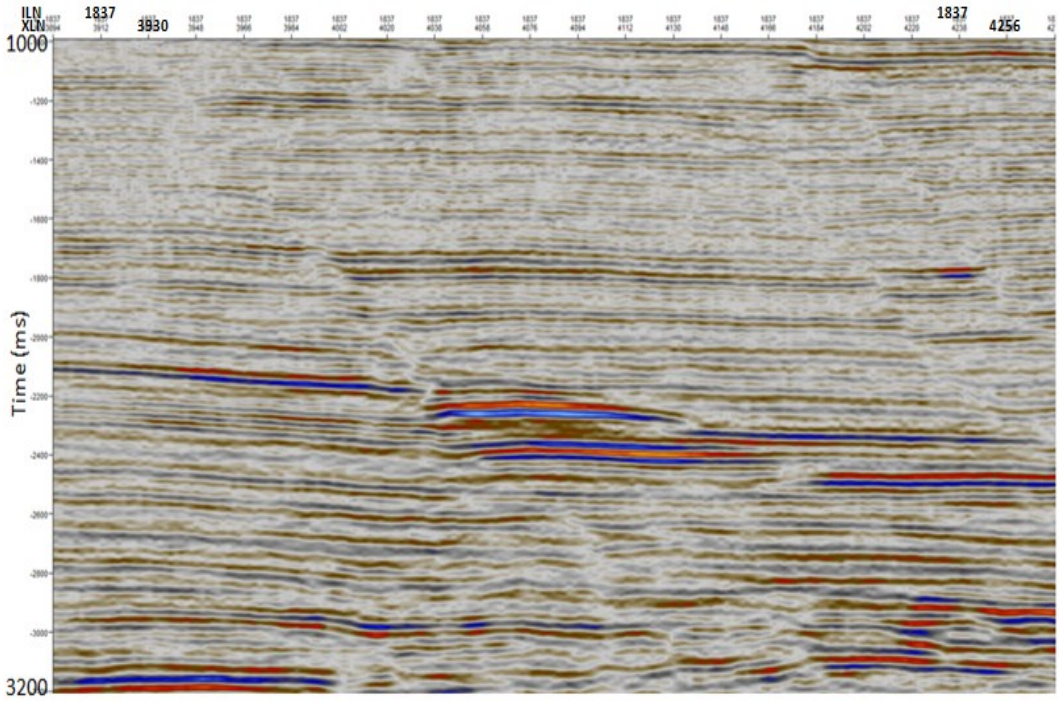

Figure 1.3: Far-angle stack (15-42°) at the same location as the near-angle stack displayed in Figure 1.2

1.6 Research methodology

The first part of this research focuses on the 3D interpretation of seismic data to understand the different structures present in the study area, and to identify potential hydrocarbon reservoirs.

This is followed by well-log interpretation to identify hydrocarbon zones and delineate lithology. Seismic-to-well ties were also carried out to match the hydrocarbon zones identified in the well-log data to the seismic data. The Elog module of the Hampson-Russell software was used for the well-log analysis and seismic-to-well tie.

AVO modeling with and without hydrocarbon saturation is carried out to investigate the effect of fluid on the seismic signature. AVO gas synthetics generated are compared to the seismic and the zone of interest is critically examined to check for similarities in AVO signatures. Models for brine-saturated reservoir and gas-saturated reservoir are also compared to each other.

The Hampson-Russell STRATA module does elastic impedance inversions using the angle stacks. Since STRATA does not do extended elastic impedance inversion (EEI), I have developed a methodology to do EEI with STRATA with elastic impedance inversion and additional standardizing steps. Model-based (elastic and extended elastic impedance) inversion is conducted using the near- and far-angle stacks along with P-wave sonic, S-wave sonic and density curves, picked horizons, and extracted wavelets.

The last research phase is the integration and interpretation of the results from seismic, logs, horizons, and inversions. The research workflow is shown in Figure 1.5.

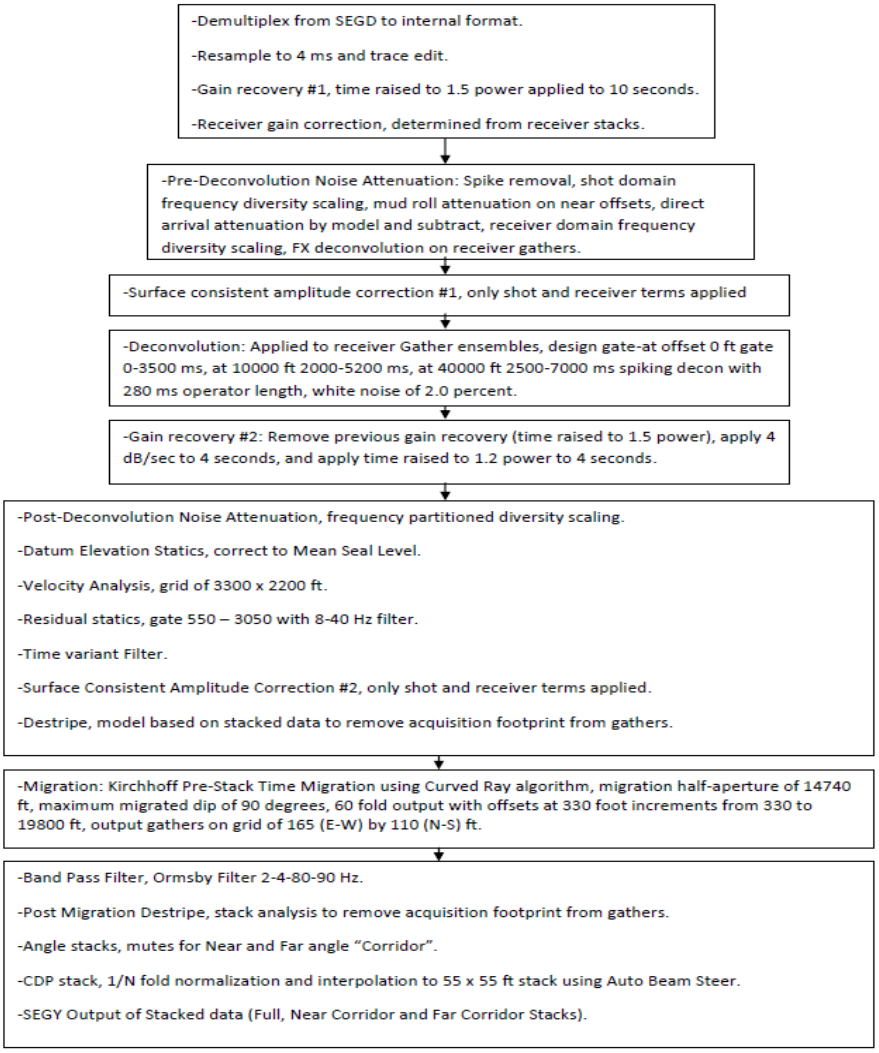

Figure 1.4: Processing workflow (Courtesy of Fairfieldnodal Industries).

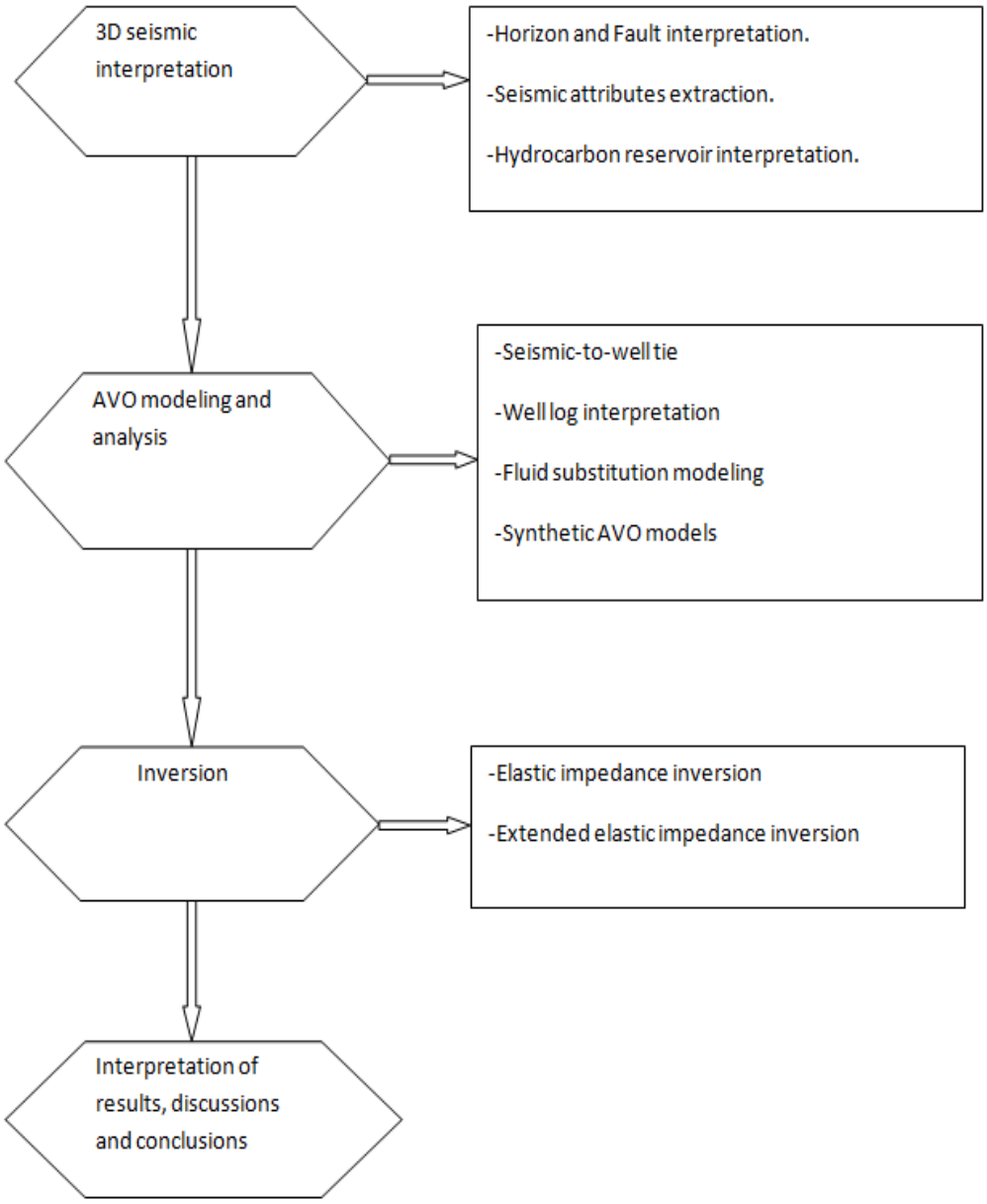

Figure 1.5: Research workflow.

CHAPTER 2

GEOLOGIC SETTING OF THE STUDY AREA

The study area is in the High Island area of offshore Texas Gulf of Mexico (GOM).The Gulf is bordered by the United States to the north, five Mexican states to the west, and the Island of Cuba to the southeast. The Gulf measures approximately 1,600 km from east to west, 900 km from north to south, and has a surface area of 1.5 million km^2. A GOM map is shown in Figure 2.1. A second map of the GOM (Figure 2.2) shows the approximate location of the study area in the northern part of the GOM.

The GOM basin is described as a roughly circular structural basin with up to 15km of sediments ranging in age from Late Triassic to Holocene (Boorman et al., 2006). Approximately 20% of the surface area lies in water depths greater than 3,000 m (9800 ft). The basic structural and stratigraphic framework of the GOM Basin was established during the Late Triassic and the Jurassic. The GOM began with the breakup of West Central Pangea, which involved northern South America and West Africa. During the Late Paleozoic, renewed orogenic activity associated with Gondwana-Larentia suture affected large segments of West Central Pangea and was followed by Mesozoic rifting. The activities of the Triassic period focused along the Western portions of the GOM, continuing into Eastern Mexico and South America; while the Jurassic rift trend followed along the separation between the Yucatan and northern South America (Boorman et al., 2006). The Jurassic rift produced the “Hispanic corridor” that permitted Tethyan and Pacific marine faunas to mix at a time when the GOM underwent continental sedimentation. The present-day GOM is a small ocean basin with its greatest water depth reaching approximately 3700 m (MMS, 2001). The GOM Basin is a gently dipping homocline that extends for almost 900 miles from the Ouachita Mountains of Arkansas and Oklahoma to the Sigsbee Deep at the base of

the continental slope. The complex stratigraphic and structural setting of the Gulf results from an interplay of high sedimentation and salt tectonics, which are also the major factors controlling depositional processes within the basin. Sediments that are deposited on the outer shelf and upper slope have the greatest potential for hydrocarbon accumulation on the continental shelf of the northern GOM (Boorman et al., 2006).

Figure 2.1: Map showing the Gulf of Mexico (www.worldatlas.com)

Figure 2.2: Map showing the approximate location of the study area in the High Island Area.

CHAPTER 3

3D SEISMIC DATA INTERPRETATION

3.1 Introduction

This chapter attempts to describe the structural and amplitude information derived from 3D seismic interpretation of the seismic volumes. For these purposes, attributes extracted from the near- and far-angle stack volumes are analyzed. The base map of the 3D seismic survey is shown in Figure 3.1.

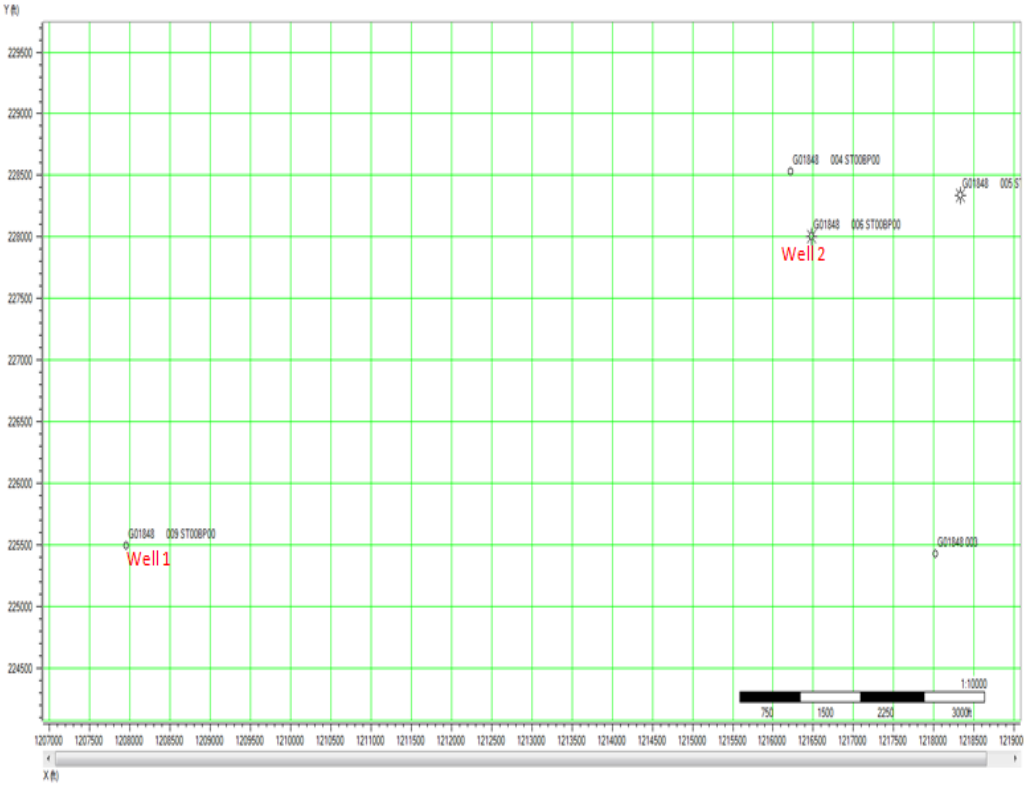

Figure 3.1: Base map of the study area (inlines are north-south while crosslines are east-west).

A summary of the steps used in analyzing these seismic volumes is shown below (not necessarily in the order listed):

- Horizon interpretation
- Fault interpretation
- Time structure maps on three horizons
- Interval-based Root-Mean-Square (RMS) amplitude and
- Variance attributes

3.2 Horizon interpretation

I picked three (3) horizons on the near-angle stack and far-angle stack volumes between the time interval of 1500 ms and 3200 ms. Horizon 1 was picked close to the gas-saturated reservoir time in Well 1 at about 2260 ms, Horizon 2 was picked at about 1860 ms and Horizon 3 was picked close to the gas-saturated reservoir time in Well 2 at about 2800 ms. Figures 3.2 through 3.4 show an inline and crossline from the far-angle stack with the interpreted horizons. The picking was based on peaks. These horizons reflect the structural features including faults, which serve as a trapping mechanism for the hydrocarbons (only the major faults in the area were picked). These picked horizons will also be used to guide the interpolation of the initial model during seismic inversion.

It is observed that reflection strength on the seismic reduces with depth as a result of the loss of high frequencies. Also, amplitudes on far-angle stack are larger than those on near-angle stack. A bright spot (strong reflection) is observed at about 2240 ms (Figure 3.4).

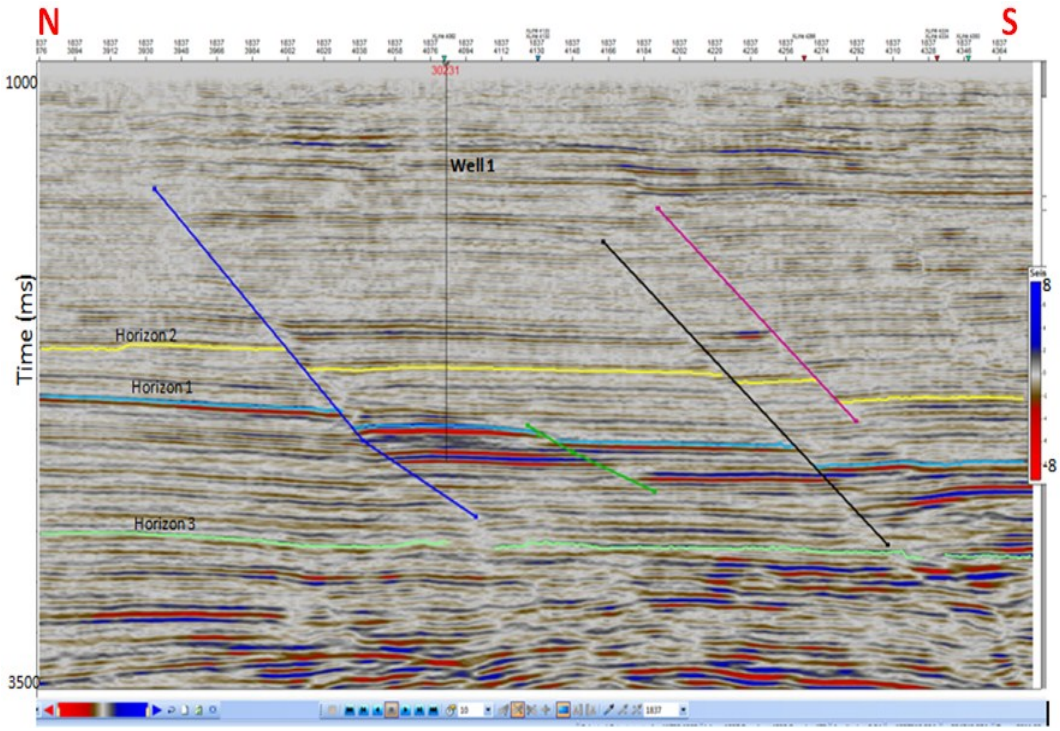

Figure 3.2: Inline 1837 from migrated far-angle stack volume.

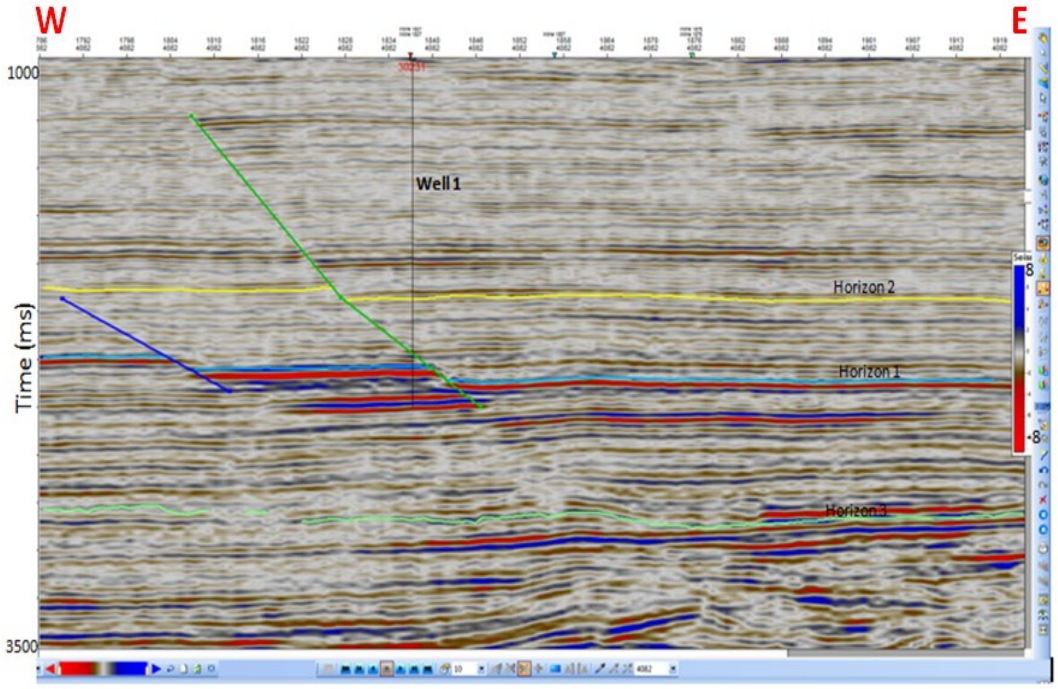

Figure 3.3: Crossline 4082 from migrated far-angle stack volume.

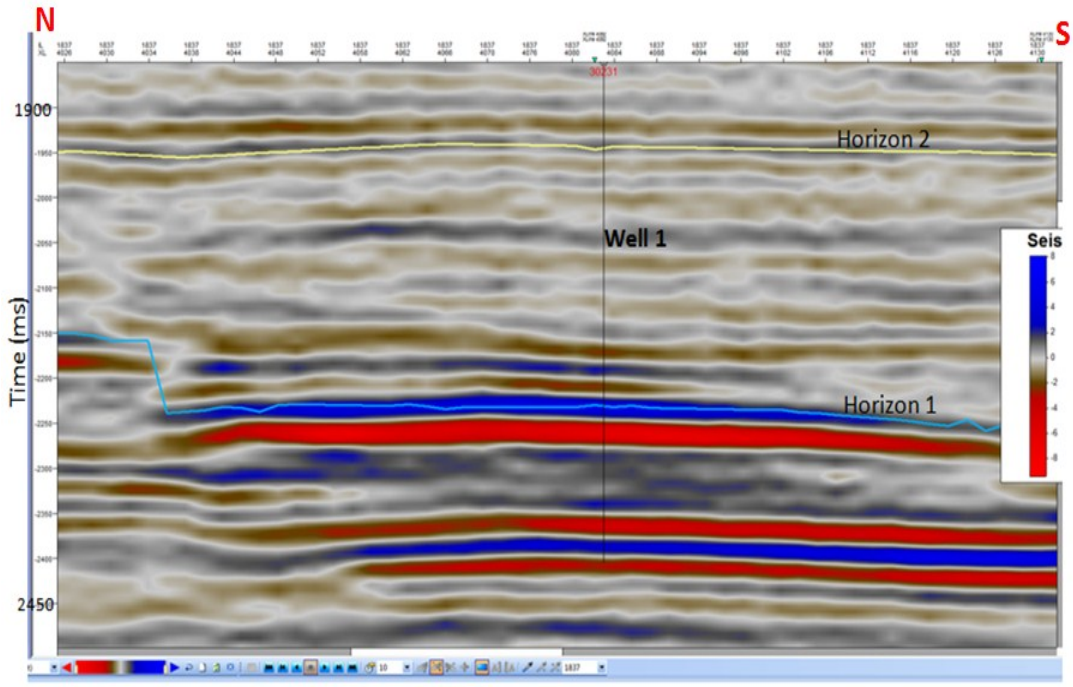

Figure 3.4: Expanded view of the strong reflection at 2240 ms shown in Figure 3.2.

3.3 Fault interpretation

Faults were picked on both the near- and far-angle stacks. These faults were used to guide the horizon interpretation. The faults in this area are normal faults as seen in Figures 3.2 and 3.3. At Well 1 (inline = 1837 and crossline = 4082), two faults bound the reservoir. Also, the same reservoir is shown bounded by faults on the amplitude map (Figures 3.14 and 3.15). Picking faults directly on the seismic section was difficult to follow on all the inline and crosslines and in order to have a better fault interpretation, I generated a variance attribute time slice at 2280 ms. Ten faults (A, B, C, D, E, F, G, H, I, and J) were picked on the variance time slice and this facilitated fault picking on the seismic sections (Figures 3.5 to 3.10). All ten faults are normal faults and their respective displacements increase downdip. Faults A, B, C, and D all meet at a point and initially, it was difficult to determine if there were four separate faults or two crossing

faults. After careful analysis though, it seems faults A and C are the same fault and fault B is an extension of fault D.

Also, fault G looks like a continuation of fault F but it is difficult to decipher. From my analysis, I believe they are two different faults though. Faults I and J are two separate faults.

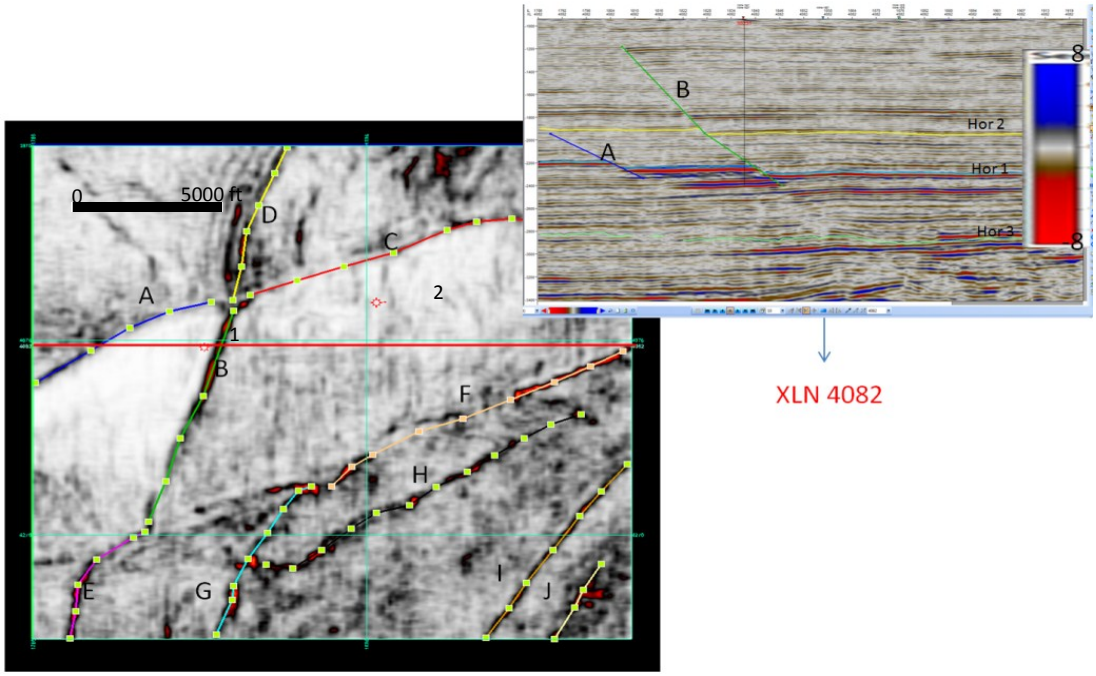

Figure 3.5: Faults picked on variance attribute time slice at 2280 ms (Crossline 4082 depicts the relationship of the faults and horizons.)

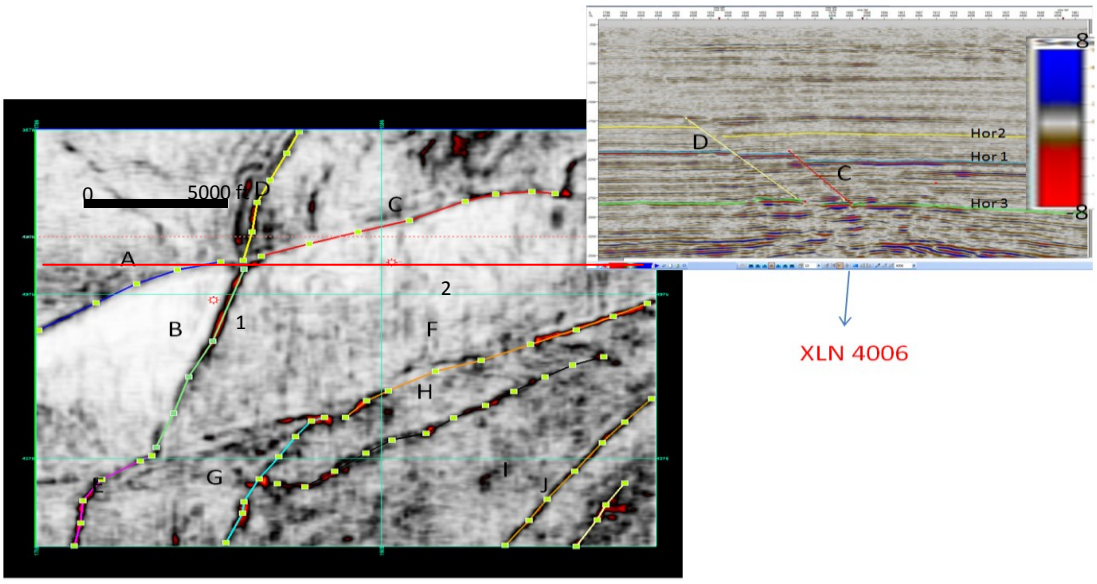

Figure 3.6: Faults picked on variance attribute time slice at 2280 ms (Crossline 4006 depicts the relationship of the faults and horizons.)

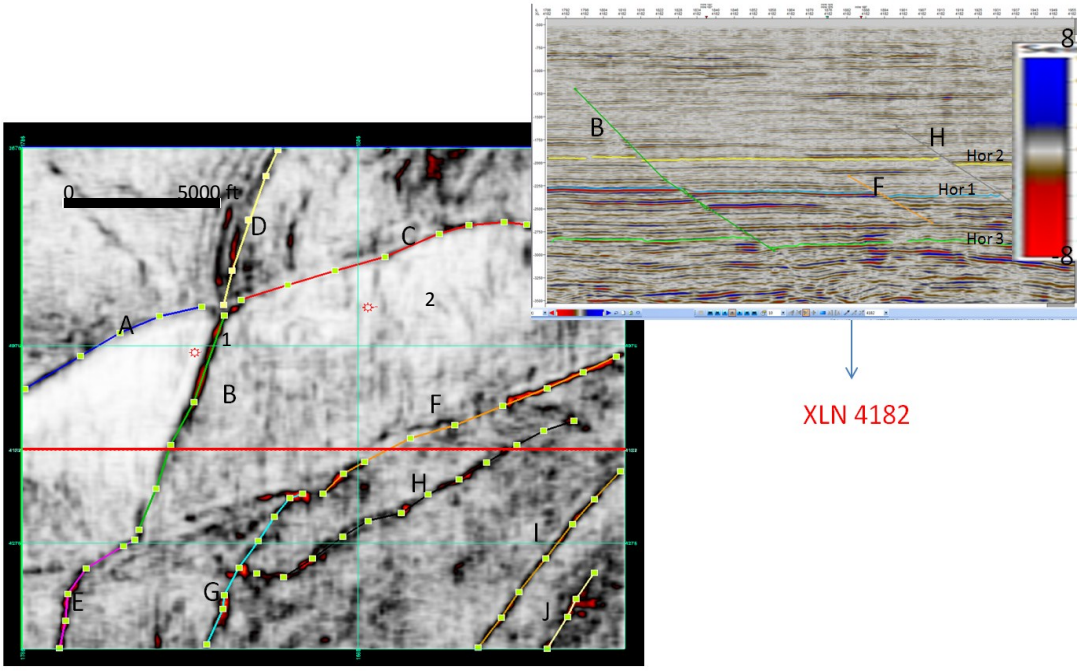

Figure 3.7: Faults picked on variance attribute time slice at 2280 ms (Crossline 4182 depicts the relationship of the faults and horizons.)

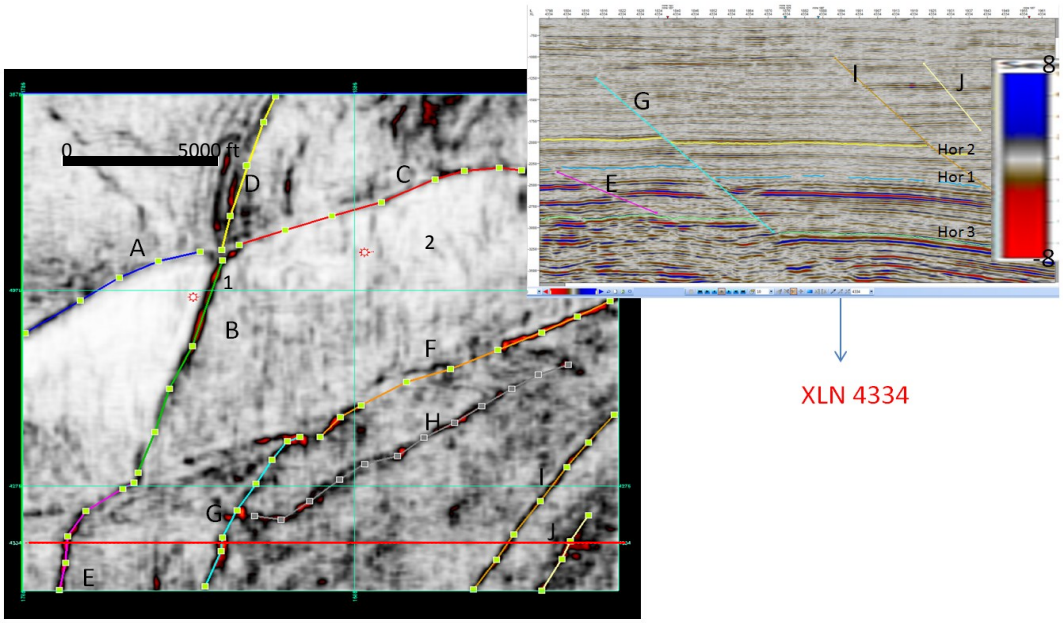

Figure 3.8: Faults picked on variance attribute time slice at 2280 ms (Crossline 4334 depicts the relationship of the faults and horizons.)

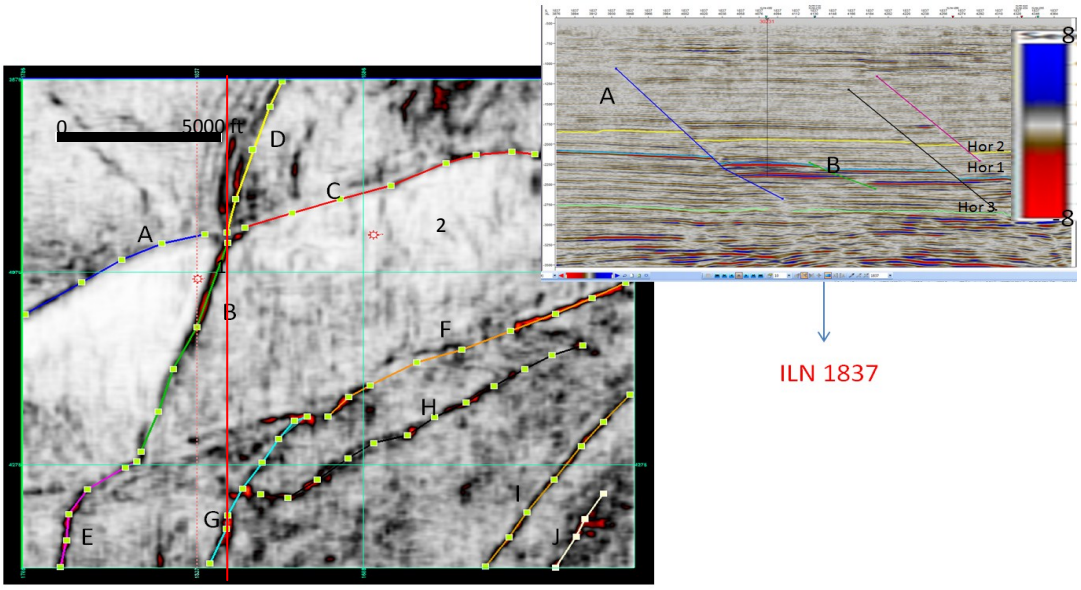

Figure 3.9: Faults picked on variance attribute time slice at 2280 ms (Inline 1837 depicts the relationship of the faults and horizons).

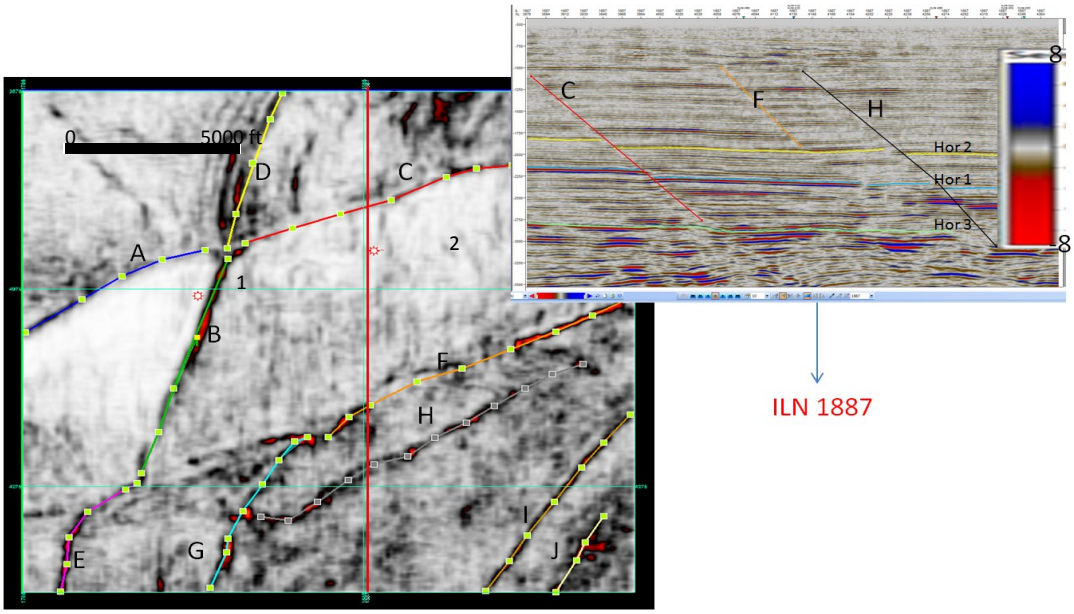

Figure 3.10: Faults picked on variance attribute time slice at 2280 ms (Inline 1887 depicts the relationship of the faults and horizons).

3.4 Seismic attributes

An attribute literally means a quality, property, or characteristic of somebody or something (Encarta, 2011). Meanwhile, a seismic attribute is a measurement derived from seismic data, usually based on measurements of time, amplitude, frequency, and/or attenuation (Sheriff, 2002). They may be time-based (related to structure) or amplitude-based (related to stratigraphy and reservoir characterization). Seismic attributes are also defined as specific quantities of geometric, kinematic, or statistical features derived from seismic data (Liner, 2004). These attributes are used to visually enhance or isolate features of prediction. The attributes generated during this research are shown below.

3.4.1 Time structure map

A structural map of Horizon 1, which includes a gas-saturated reservoir, is shown in Figure 3.11. Figures 3.12 and 3.13 show the time structure maps for Horizons 2 and 3 respectively.

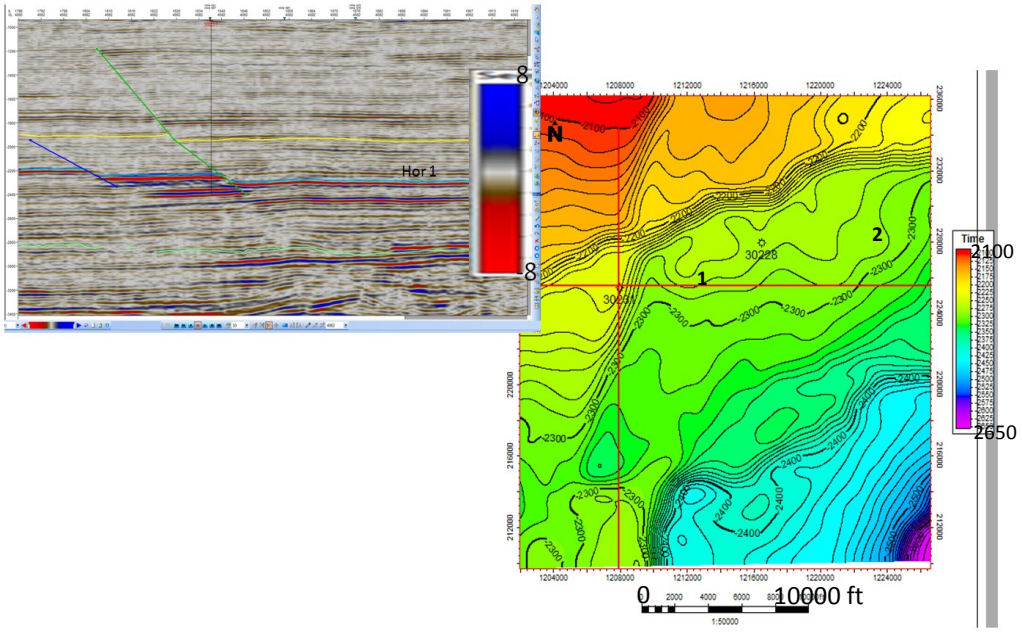

Figure 3.11: Time structure map for Horizon 1. E-W crossline 4082 depicts the relationship of the faults and time horizons.

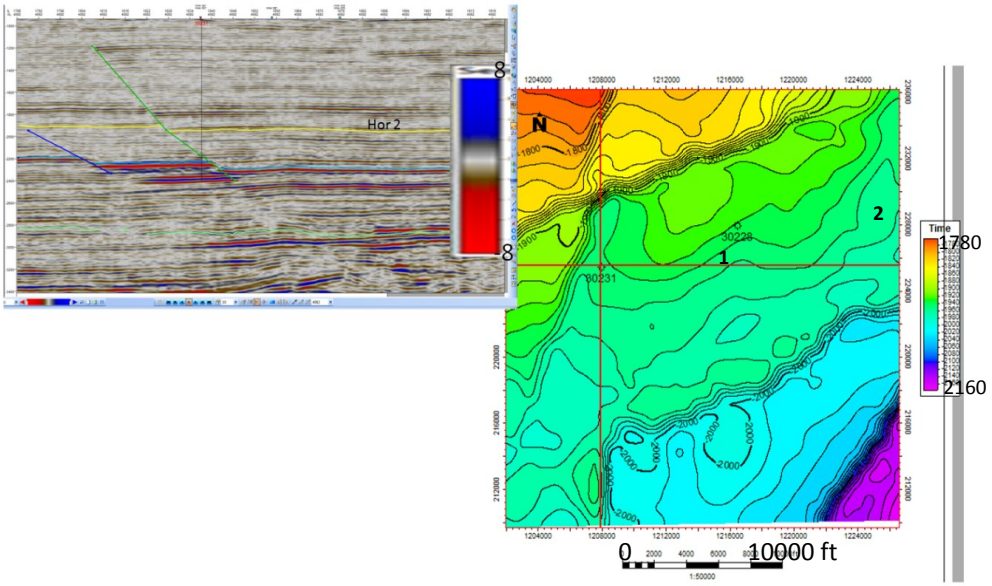

Figure 3.12: Time structure map for Horizon 2. E-W crossline 4082 depicts the relationship of the faults and time horizons.

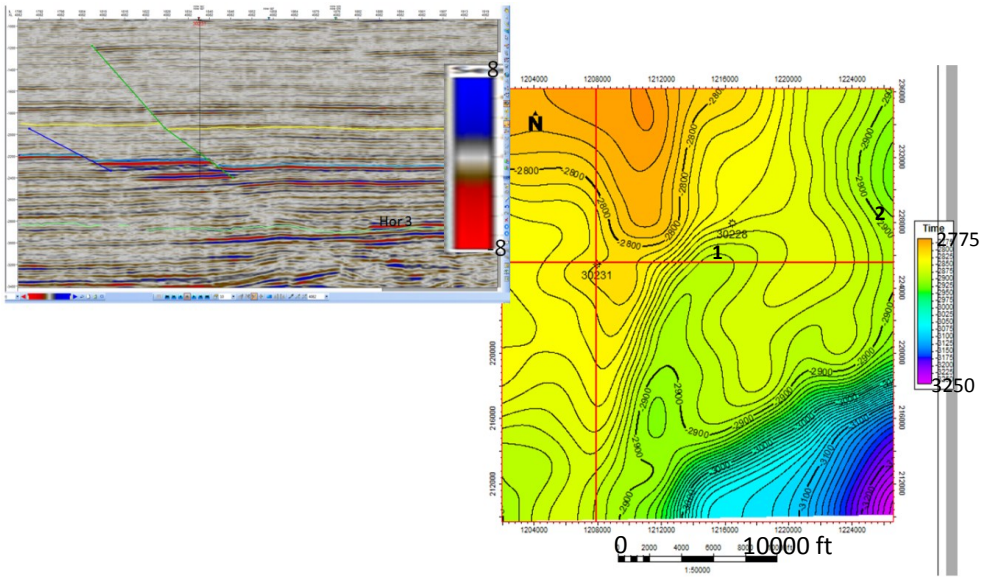

Figure 3.13: Time structure map for Horizon 3. E-W crossline 4082 depicts the relationship of the faults and time horizons.

3.4.2 RMS amplitude extraction

Seismic amplitude variation plays a major role in identifying potential hydrocarbon reservoirs and sediment direction from its source. In the environment where I am working, which happens to have a Class 2 AVO anomaly, amplitude extraction plays an important role for reservoir delineation. The RMS amplitude is extracted from both the near- and far-angle stack seismic volumes in the time intervals from 50 ms above to 50 ms below each horizon. Figures 3.14 to 3.19 contain RMS amplitude maps for all three horizons for both the near- and far-angle stack volumes. The amplitude maps are color coded with time-structure contours superimposed. These amplitude maps show the variations of amplitude on the near- and far-angle data especially at the known gas-saturated reservoir which exhibits larger amplitudes on the far-angle stack. Also, the faults that act as a trapping mechanism are well delineated.

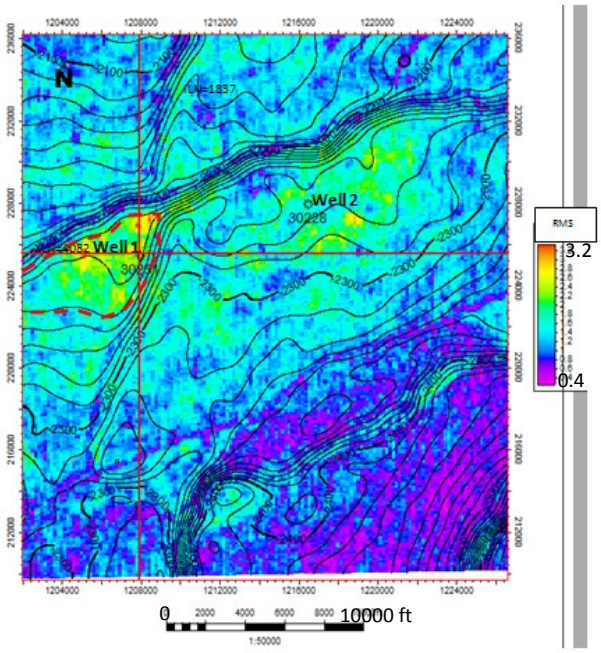

Figure 3.14: RMS Amplitude extraction on Horizon 1 from near-angle stack volume. The red dashed line is an interpretation of the gas-saturated reservoir's limit around Well 1.

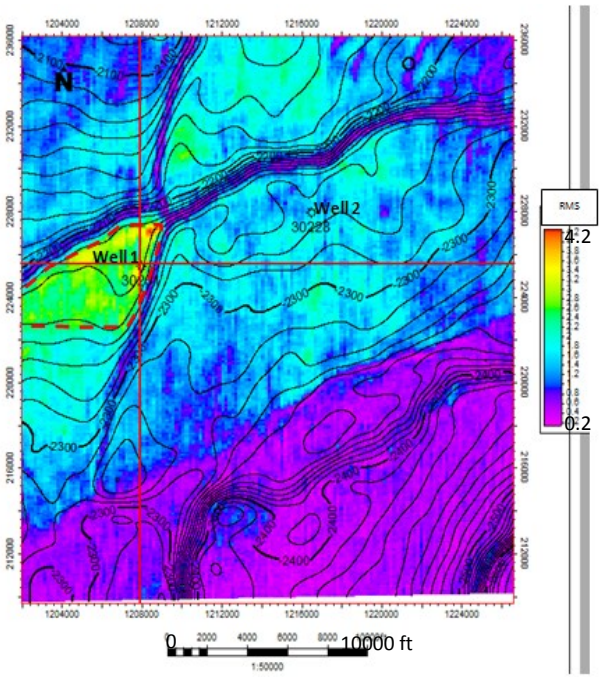

Figure 3.15: RMS Amplitude extraction on Horizon 1 from far-angle stack volume. The red dashed line is an interpretation of the gas-saturated reservoir's limit around Well 1.

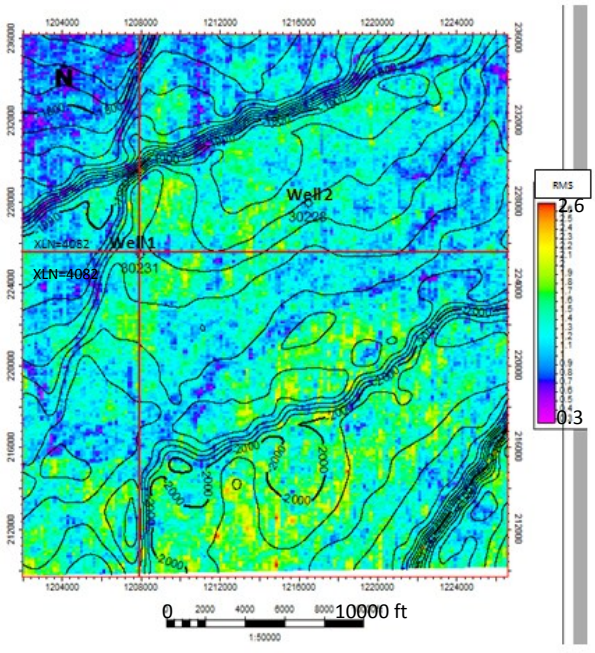

Figure 3.16: RMS Amplitude extraction on Horizon 2 from near-angle stack volume.

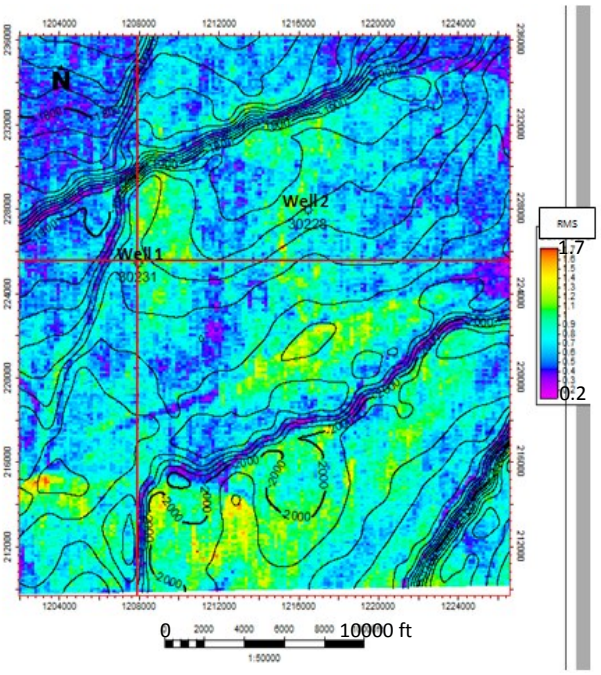

Figure 3.17: RMS Amplitude extraction on Horizon 2 from far-angle stack volume.

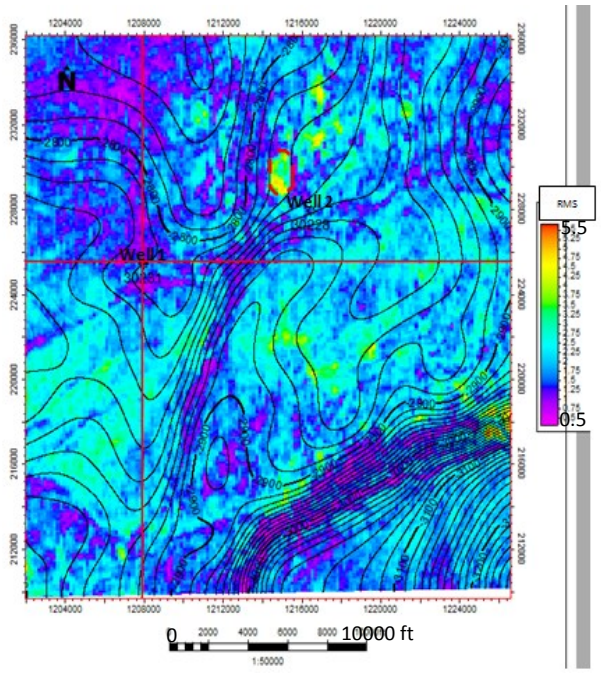

Figure 3.18: RMS Amplitude extraction on Horizon 3 from near-angle stack volume. The red dashed line is a preliminary interpretation of the gas-saturated reservoir's limit around Well 2.

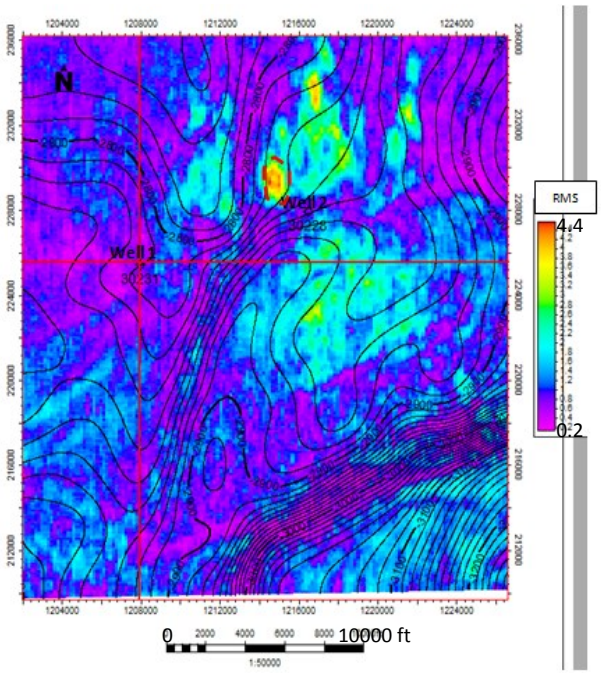

Figure 3.19: RMS Amplitude extraction on Horizon 3 from far-angle stack volume. The red dashed line is a preliminary interpretation of the gas-saturated reservoir's limit around Well 2.

3.5 Hydrocarbon reservoir interpretation

Seismic sections and amplitude maps have shown that the study area is characterized by different faults which control the trapping mechanism for the two hydrocarbon reservoirs around Well 1 and 2. Amplitude analysis have also shown that amplitudes on the far seismic is larger than on the near seismic especially around the hydrocarbon reservoir at Well 1 (Figures 3.14 and 3.15). These hydrocarbon reservoirs are classic examples of Class 2 AVO anomalies.

As seen in Figures 3.5 through 3.10, there are numerous faults (normal faults) in the study area that helped to define the hydrocarbon reservoirs. They cross over each other and their lateral identification can be confusing.

Figure 3.15 has red dashed outline that is interpreted to be the reservoir limits associated with the hydrocarbons found in Well 1. The updip limits are provided by bounding faults and the downdip limit is well defined by the correlation of the amplitude contours with a time structure contour, which is indicative of the gas-water contact. The far-angle stack shown in Figure 3.15 when compared to the near-angle stack in Figure 3.14 doesn't show as large an amplitude variation as the cross sections in Figures 1.2 and 1.3. This suggests that an RMS window of 100 ms might have been too large.

The interpretation of the reservoir limits associated with Well 2 is shown by the red dashed line in Figures 3.18 and 3.19. This amplitude interpretation of the reservoir limits is not as convincing as the previous for Well 1. It could be a timing problem that makes this interpretation around Well 2 difficult. The well was drilled in the early 1970s but the seismic was shot in the mid 1990s. Thus, it is possible the reservoir size was greatly diminished by the time the seismic was shot.

CHAPTER 4

AVO ANALYSIS AND MODELING

4.1 Seismic-to-well tie

Seismic-to-well tie is conducted on Well 1 and Well 2 using Hampson-Russell's Elog. I applied two methods for wavelet extraction; the first is the extraction of a zero-phase wavelet from the seismic while the second method is the extraction of a match-filter (best fit wavelet) after the seismic-to-well tie. The second method requires two steps of extraction; first step is the extraction of a match filter wavelet from an initial seismic-to-well tie. This first match filter wavelet is then used to generate another synthetic which is tied again to the angle-stack. A second match filter (best fit wavelet) is then extracted.

For Well 1, zero-phase wavelets are extracted from the near- and far-angle stacks using Fourier transforms of the seismic traces located near the well. To tie the well to the near-angle stack, I generated a synthetic at an incident angle of $\theta_1(8.5°)$ by convolving the reflectivity [$(r_1(t))$ derived from the density, P-wave and S wave logs of Well 1 (using the elastic impedance equation) with the zero phase wavelet ($w_1(t)$)] extracted from the near-angle stack. This synthetic is then stretched and squeezed so as to make events on the synthetic tie the events on the near-angle stack. After this, the first match filter wavelet is extracted. Then, I use the first match filter wavelet to generate another synthetic which I also tie to the near-angle stack again by the stretch and squeeze of the synthetic, a better tie with a higher correlation coefficient is then achieved at this point. Then, I extract the second match filter wavelet (best fit wavelet) and this leads to the generation of a new P-wave curve (time-depth function) which is saved. To tie Well 1 to the far-angle stack, the same procedure is applied as was done for the near-angle stack except an incident angle of $\theta_2(28.5°)$ was used to generate the elastic impedance reflectivity. The same procedure is carried out for Well 2.

The properties of the zero phase wavelet used for the well tie are 1000ms amplitude spectrum window, 200 ms wavelet length with a 25ms taper. The synthetic seismogram equations 4.1 and 4.2 illustrate that the reflectivity is a function of both time and incident angle.

$$s_1(t) = w_1(t) * r_1(t, \theta_1), \theta_1 = 8.5^o \quad (4.1)$$

$$s_2(t) = w_2(t) * r_2(t, \theta_2), \theta_2 = 28.5^o \quad (4.2)$$

Some assumptions involved in the generation of the synthetic include: the well bore is vertical, log readings are accurate, and the velocity only varies with depth (Liner, 2004). Figure 4.1 shows the extracted zero-phase wavelets from both the near- and far-angle stacks for Wells 1 and 2.

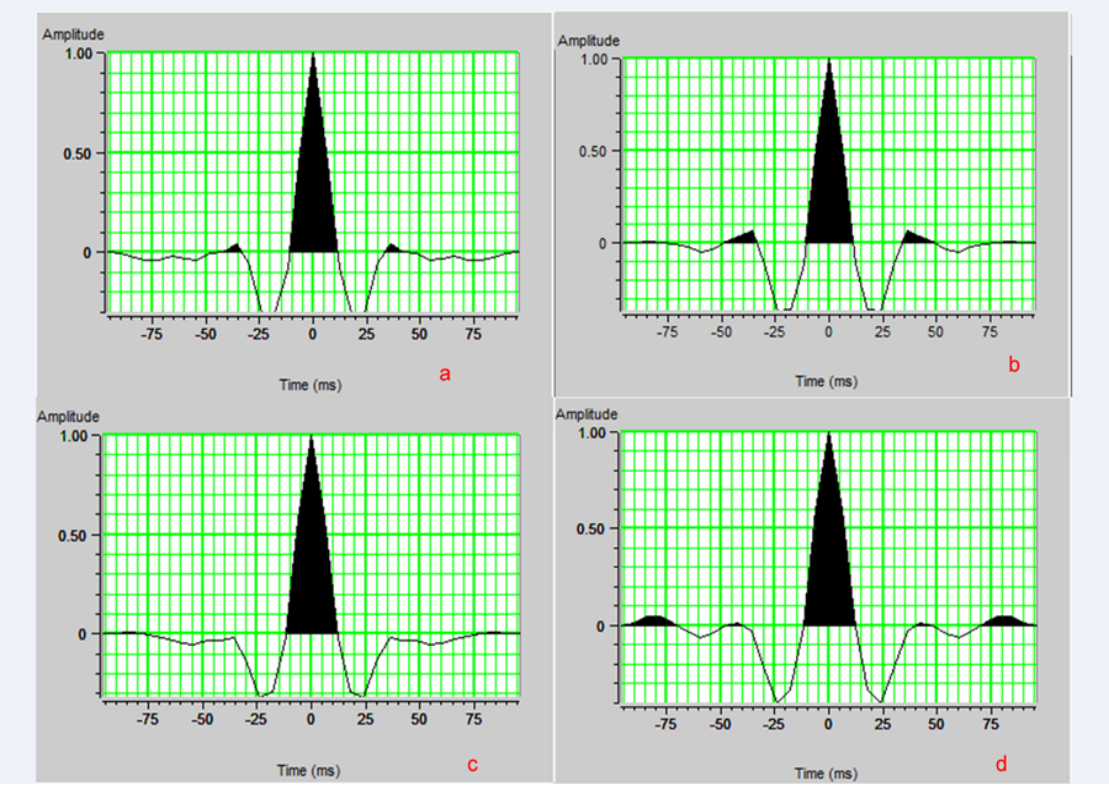

Figure 4.1: (a) Zero-phase wavelet extracted from near-angle stack for Well 1, (b) zero-phase wavelet extracted from far-angle stack for Well 1, (c) zero-phase wavelet extracted from near-angle stack for Well 2 and (d) zero-phase wavelet extracted from far-angle stack for Well 2.

Figure 4.2 shows how the synthetics tie to the angle stacks for Well 1. The blue traces are the synthetic data generated at incident angles of 8.5° and at 28.5° for both the near- and far-angle stacks respectively. The red traces are the composite traces from the angle stacks and the black traces are the angle stacks. The same procedure was carried out for Well 2 and the results of the seismic-to-well tie are shown in Figure 4.4. The final best-fit wavelets along with their amplitude and phase spectra extracted after the seismic-to-well-tie are shown in Figures 4.3 and 4.5.

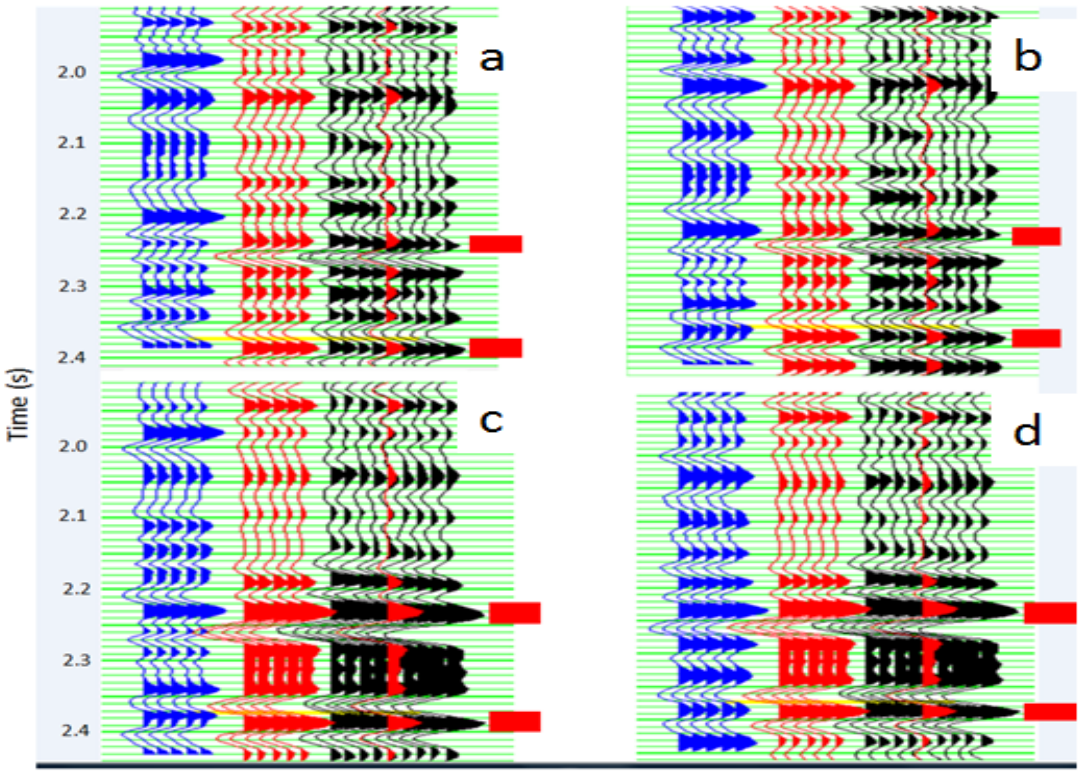

Figure 4.2: Well 1 synthetic tie. Blue traces represent the synthetic and the red, field data (a) Near-angle stack and synthetic (8.5°) (CC = 0.484) using zero-phase wavelet with no stretching, (b) Near-angle stack and synthetic after tie (CC = 0.761) using match filter wavelet (best fit wavelet) , (c) Far-angle stack and synthetic (28.5°) before tie (CC = 0.485) using zero-phase wavelet with no stretching and (d) Far-angle stack and synthetic after tie (CC = 0.772) using match filter wavelet (best fit wavelet). The red rectangles represent the gas zones and CC is correlation coefficient.

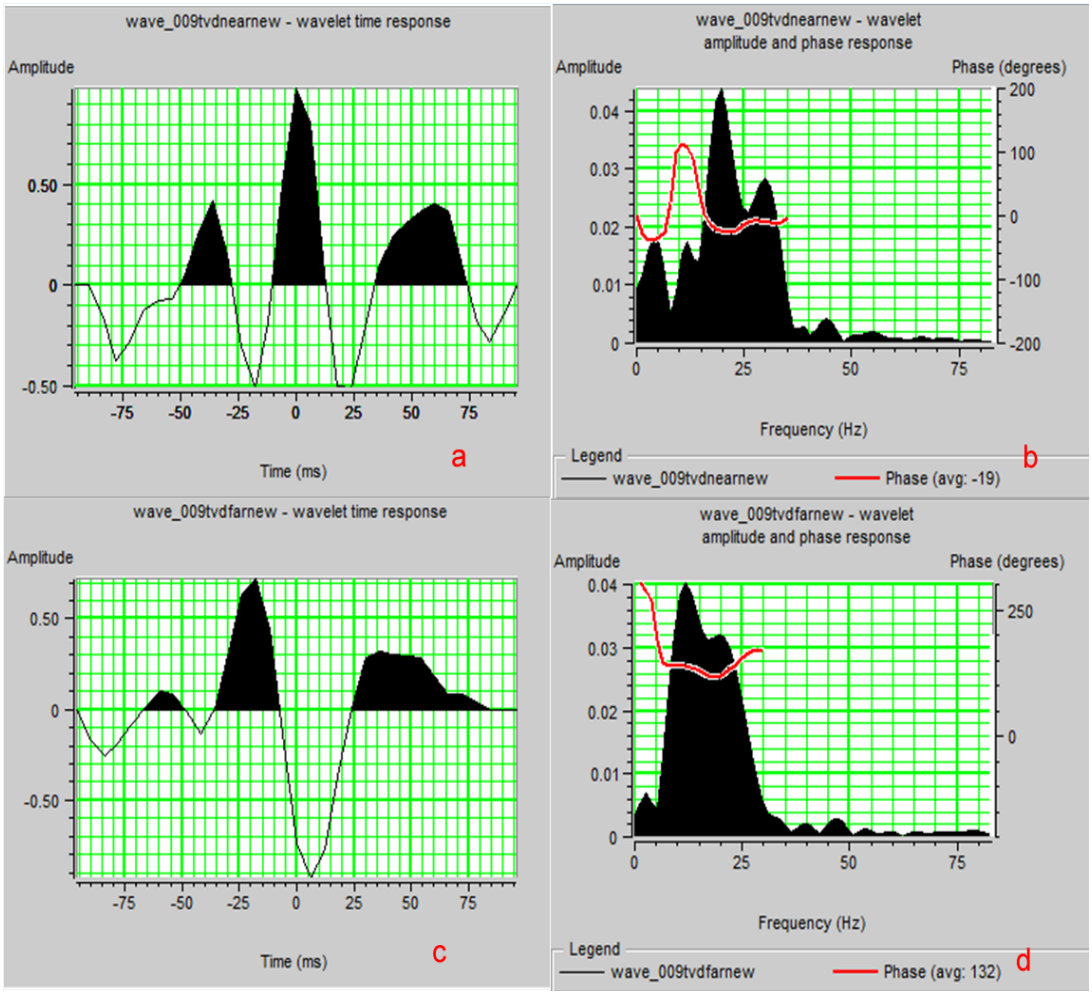

Figure 4.3: (a) Near-angle stack wavelet extracted from traces near Well 1, (b) amplitude and phase spectra of wavelet shown in (a), (c) far-angle stack wavelet extracted from traces near Well 1, and (d) amplitude and phase spectra for wavelet in (c). In (b) and (c), the red lines represent the phase of the wavelets.

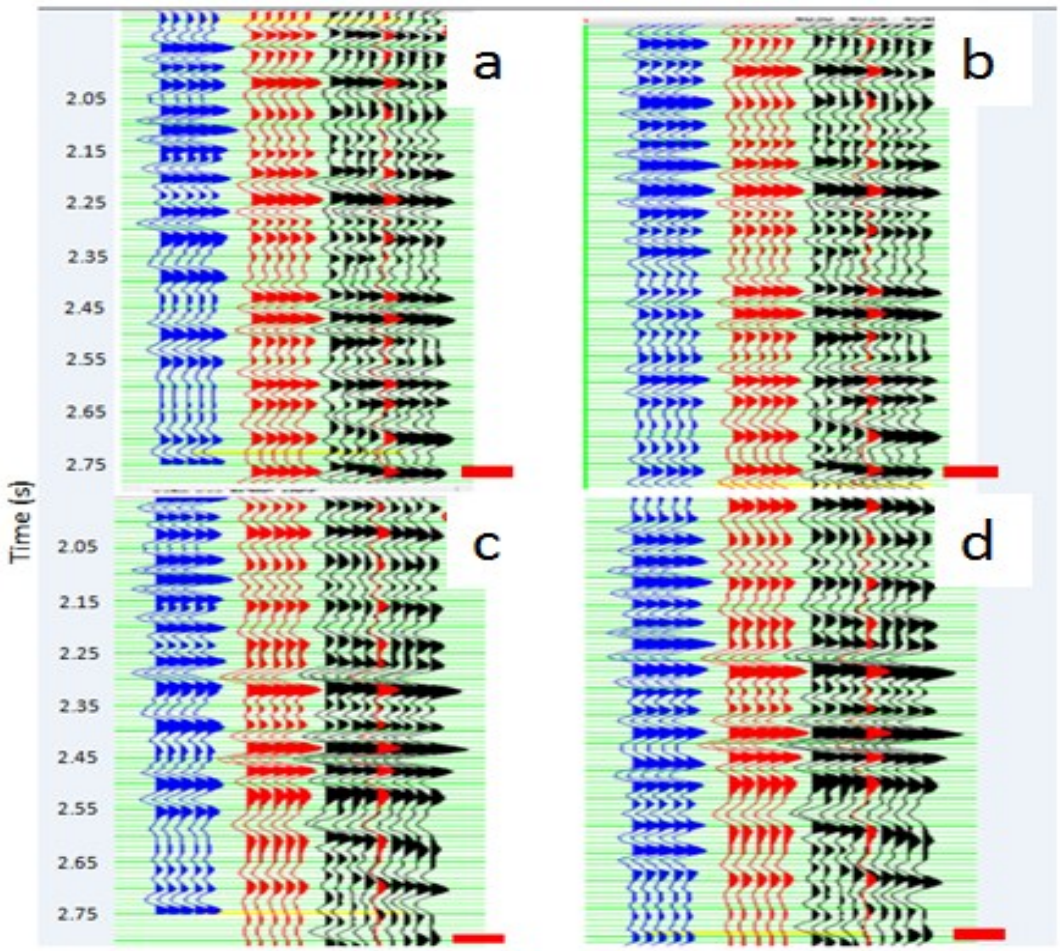

Figure 4.4: Well 2 synthetic tie. Blue traces represent the synthetic and red, field data (a) Near-angle stack and synthetic (8.5°) (CC = 0.233) using zero-phase wavelet with no stretching, (b) Near-angle stack and synthetic after tie (CC = 0.656) using match filter wavelet (best fit wavelet), (c) Far-angle stack and synthetic (28.5°) (CC = 0.453) using zero-phase wavelet with no stretching and (d) Far-angle stack and synthetic after tie (CC = 0.676) using match filter wavelet (best fit wavelet). The red rectangles represent the hydrocarbon zones and CC is correlation coefficient.

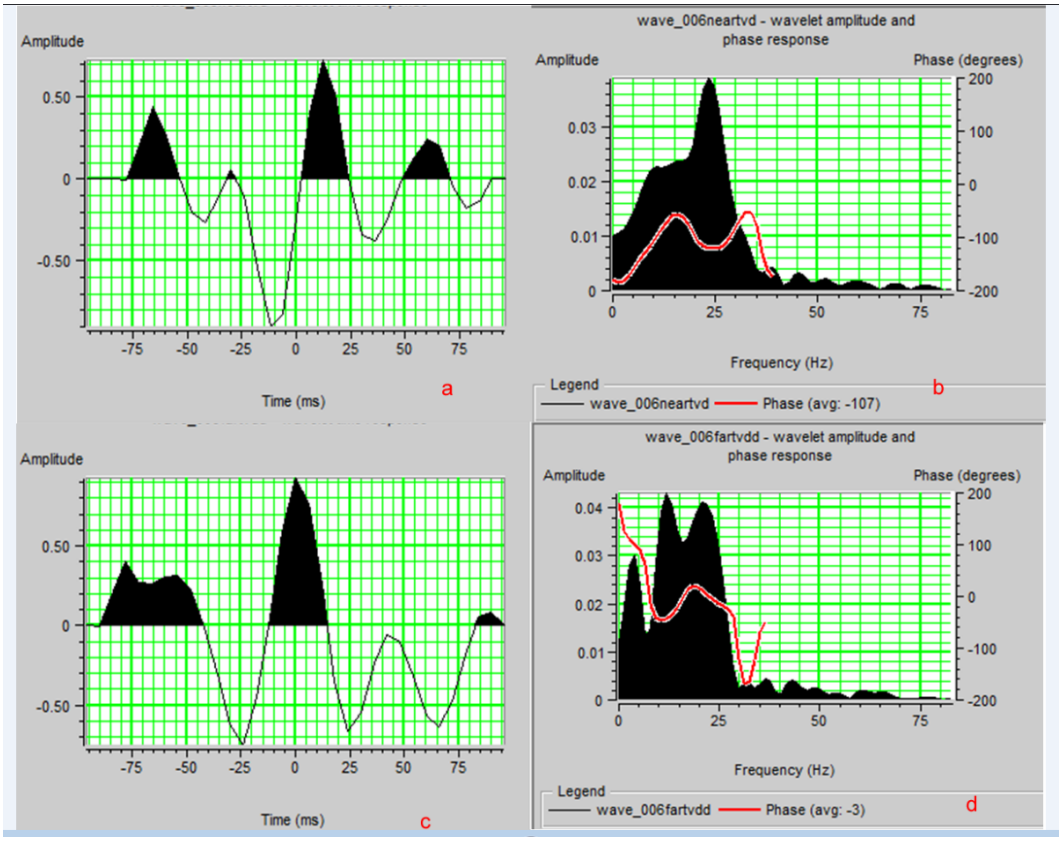

Figure 4.5: (a) Near-angle stack wavelet extracted from traces near Well 2, (b) amplitude and phase spectra of wavelet shown in (a), (c) far-angle stack wavelet extracted from traces near Well 2, and (d) amplitude and phase spectra for wavelet shown in (c). In (b) and (c), the red lines represent the phase of the wavelets.

The synthetics generated at the far angle (28.5º) match the field data better than the ones generated at the near angle (8.5°). This could be a result of more seismic noise present on the near-angle data as compared to the far-angle data or because amplitude increases with offset in my study area, hence, sand formations both wet and with hydrocarbons are better seen on the far offsets. Another reason for the poor well-tie match is the time gap between when the wells were

drilled (Well 1 in 1984 and Well 2 in 1975) and the time the seismic data were acquired (1994), i.e. the wells have been producing for years before the seismic data were acquired.

There are numerous other reasons that could be responsible for a poor well-to-seismic tie and some were enumerated by Liner (2004). These include: frequency differences between log and seismic; borehole problems such as washouts which affects sonic logs; wavelet estimation problems; data processing and transmission loss; geometric spreading, and frequency-dependent absorption.

4.2 Well log interpretation

This section focuses on the pore-fluid interpretation of the well logs. Figures 4.6 and 4.7 show the available logs and the hydrocarbon zones for Well 1 while Figures 4.8 and 4.9 show the available logs for Well 2 and its hydrocarbon zone(s). Two major hydrocarbon zones are identified in Well 1. The first gas-saturated reservoir occurs at 8114−8144 ft (~2473−2483 m) while the second (deepest) gas reservoir is between 8802−8835 ft (~2683−2693 m). Other hydrocarbon zones in Well 1 occur in the depth intervals of 8030−8060 ft (~2448−2457 m), 8540–8558 ft (~2603−2608 m) and 8610−8630 ft (~2624−2630 m) as seen in Figure 4.6. I concentrated on the two major reservoirs in Well 1. The pay intervals in the first reservoir of Well 1 are: 8114−8119 ft (~2473−2475 m), 8125–8132 ft (~2477−2479 m) and 8135–8144 ft (~2480−2482 m). The second gas-saturated reservoir has pay intervals of 8802–8820 ft (~2683−2688 m) and 8825−8835 ft (~2690−2693 m). The gross thicknesses of the first reservoir and second reservoir are 30 ft (~9 m) and 33 ft (~10 m) respectively. The depth interval for the hydrocarbon zone in Well 2 is at 9415–9436 ft (~2870−2876 m). The porosity and water saturation of the reservoir in Well 1 are approximately 30% and 0.15 respectively, while Well 2 has a porosity of 26% and water saturation of 0.29. All reservoirs are classified as thin beds with respect to the seismic resolution.

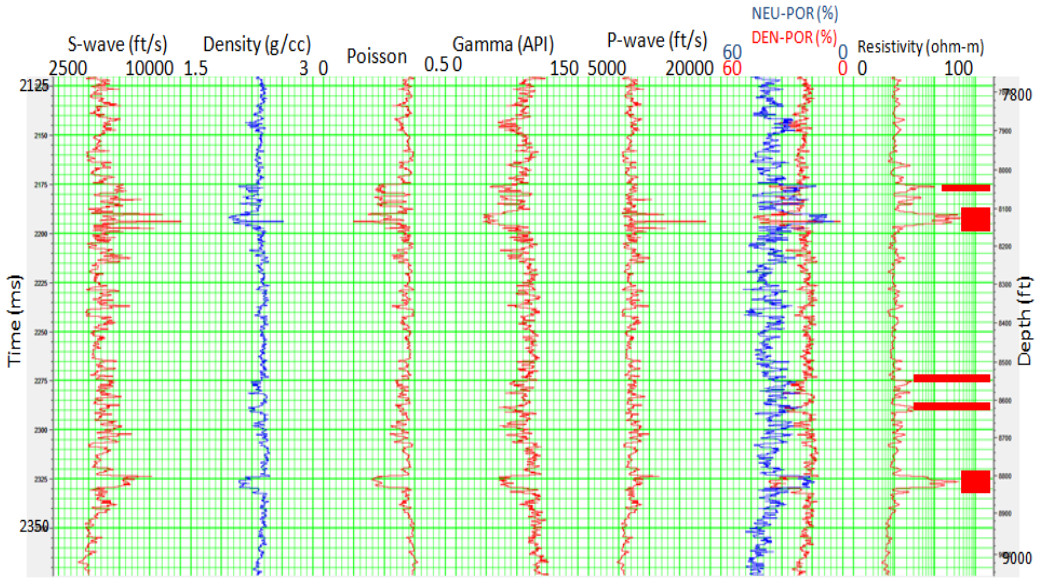

Figure 4.6: Available logs for Well 1. The red rectangles represent the hydrocarbon zones.

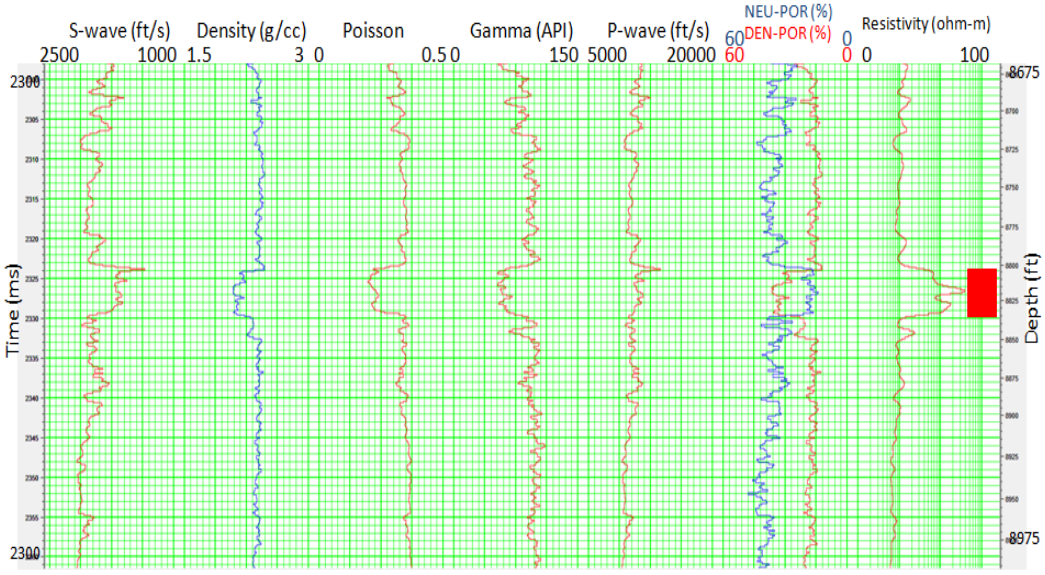

Figure 4.7: An expanded view from Figure 4.6 showing the deepest reservoir interval. The red rectangle represents the hydrocarbon zone.

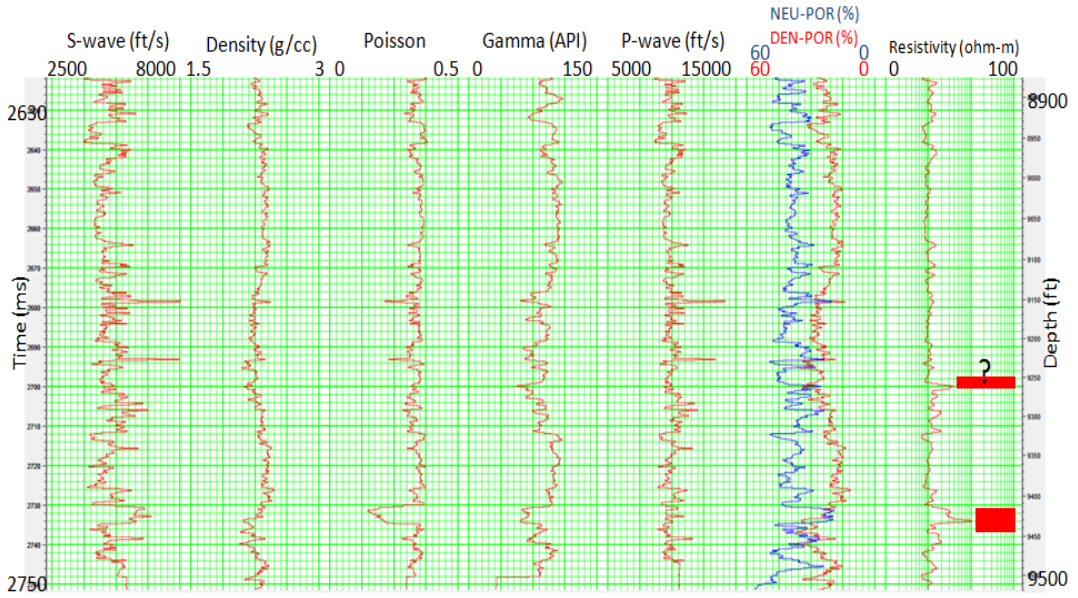

Figure 4.8: Available logs for Well 2. The rectangles represent the hydrocarbon zones.

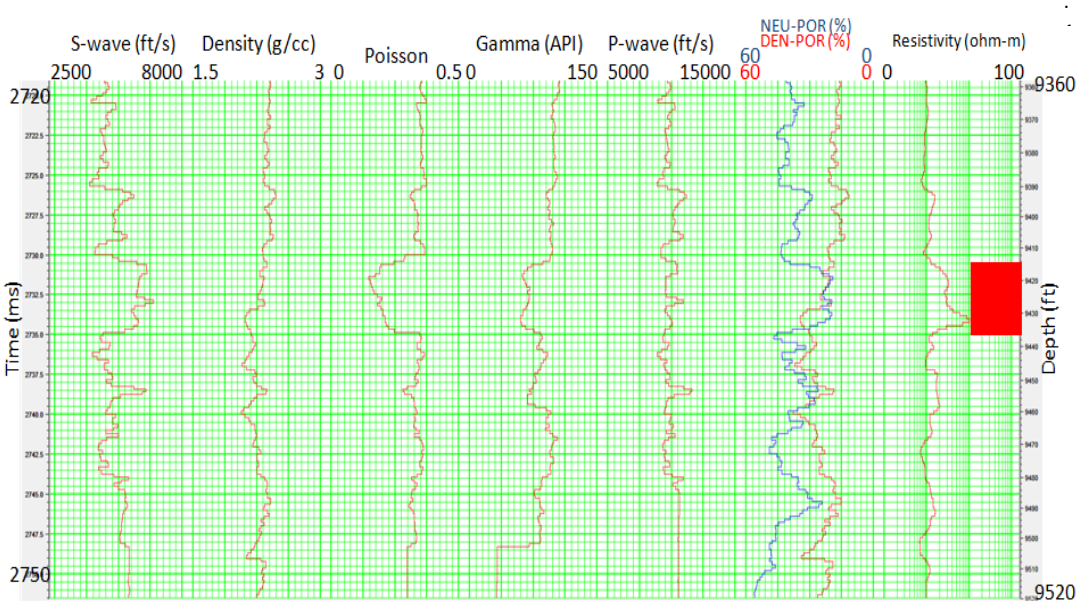

Figure 4.9: An expanded view from Figure 4.8 showing the reservoir interval. The red rectangle represents the hydrocarbon zone.

4.2.1 Gamma-ray log

The reservoirs show low gamma reading and deflection to the left as seen in Figures 4.7 and 4.9 which indicate sand formations. Generally, values for the gamma ray logs in clastic sediments vary from 0–150 API units and generally, readings below 75 indicate sand units and values above 75 indicate shale units. The lowest and highest readings on the gamma ray log for Well 2 are 44 and 126 respectively which indicates the sand reservoirs are shaly. The reservoir interval from 8114−8144 ft (~2473−2483 m) in Well 1 has a low value of 51.

4.2.2 Density and neutron logs

Well 1 records a high density of about 2.44 g/cc in the shale unit at 8710 ft (~2655 m) and decreases to about 2.08 g/cc in the sand reservoir at 8816 ft (~2687 m) as seen in Figure 4.7. Well 2 shows similar behavior. Although all sand units have low densities, the gas-saturated reservoirs record the lowest densities, illustrating the presence of hydrocarbons. Average density value for brine-saturated sand is about 2.25 g/cc. In Figure 4.6 for Well 1, there is significant crossover on the neutron-density plot for the 8120 and 8820 gas-saturated reservoirs along with a significant increase in the resistivity which suggest good gas saturation. However, in Figure 4.9, the deep gas-saturated reservoir does not exhibit a crossover in the upper portion of the reservoir and the resistivity curve in the upper portion of the reservoir is also suppressed compared to the deeper portion. This suggests that the Well 2 reservoir might have more than one compartment.

4.2.3 P-wave sonic log

The P-wave sonic log measures the transit time (Δt in μs/ft) of an acoustic waveform between a transmitter and a receiver (Veeken, 2007). Both wells show a general increase in velocity with depth, with a slight increase in velocity in the Well 1 reservoir (Figures 4.7) and an indeterminate velocity variation for the reservoir in Well 2 (Figure 4.9).

4.2.4 Pseudo S-wave sonic log

Shear waves have a slower velocity when compared to the P-waves. A pseudo-shear wave log was provided for this research and it was generated from the P-wave log using the Greenberg-Castagna equation (1992).

4.2.5 Resistivity log

Resistivity is "the property of a material that resists the flow of an electric current" (Sheriff, 2002). A brine-saturated rock is expected to have a lower resistivity than hydrocarbon-saturated rock, as it is more conductive. Resistivity logs available in the area show higher values at the reservoir as compared to lower values in the surrounding formation (shale). Values of resistivity in the gas-saturated reservoir of Well 1 range between 20 and 30, 1 to 3 in the surrounding shale and 0.3 to 0.7 in brine-saturated sand formations (Figures 4.6 and 4.7). These resistivity values help in calculating water saturation in the reservoir as shown in the next section.

4.2.6 Water saturation (S_w)

This is the fraction of the pore volume filled with formation water (Sheriff, 2002) and is generally calculated by Archie's formula, which is

$$S_w = (a/\Phi^m * R_w/R_t)^{0.5} \quad (4.3)$$

where a is a constant, m is cementation factor, Φ is porosity, R_w is the resistivity of the formation water, and R_t is the true resistivity of the formation. Selley (1985) pointed out that this method is valid for clean, clay-free formations. Generally, a=1 and m=2; however, for unconsolidated sands (soft formations), a = 0.62 and m= 2.15 from the Humble formula (Selley, 1985). From equation (4.3), the only unknown is R_w which has to be calculated from a brine-saturated portion of the log as shown below:

$$S_w = (c * [R_w/R_t]^{0.5})/ \Phi \quad (4.4)$$

where c is a constant and has a value of 0.9 for sand formation and 1 for carbonates. The R_w (0.078 for Well 1 and 0.047 for Well 2) determined using equation 4.4 is substituted into equation 4.3 to calculate the water saturation, the approximate values for S_w in the gas-saturated reservoir for Well 1 is 0.15 and 0.29 for Well 2. Figures 4.10 and 4.11 show the water saturation curves for both wells.

4.2.7 Density porosity log

Porosity is the amount of pore or void spaces found in a rock which determines its capacity to store or hold fluids (Gluyas and Swarbrick, 2004). It is generally expressed as,

Porosity (%) = (volume of pore space/total volume of rock) x100 %

Because density logging tools do not directly measure porosity, it is estimated as,

$$\Phi = (\rho_b - \rho_m)/(\rho_f - \rho_m) \quad (4.2a)$$

where Φ is the porosity, ρ_b is the bulk density of the rock, ρ_m is the density of the matrix and ρ_f is the density of the fluid. The density porosities in Figures 4.10 and 4.11 are calculated by specifying ρ_b (observed on the log), and ρ_m (sandstone) which for quartz is 2.6 g/cc. In order to determine the ρ_f, I used the following:

$$\rho_f = (1 - S_w)\rho_{gas} + S_w(\rho_{water}), \quad (4.2b)$$

$\rho_{gas} = 0.29$ g/cc and

$\rho_{water} = 1.09$ g/cc

The approximate ρ_f values in Well 1 and Well 2 respectively are 0.4 g/cc and 0.5 g/cc. These ρ_f values are then substituted into equation 4.2a to determine the porosities. Well 1 has an average porosity value of 30% in the gas-saturated reservoir while Well 2 has an average porosity value of 26% in the gas-saturated reservoir. The porosity logs generated for both wells are shown in Figures 4.10 and 4.11.

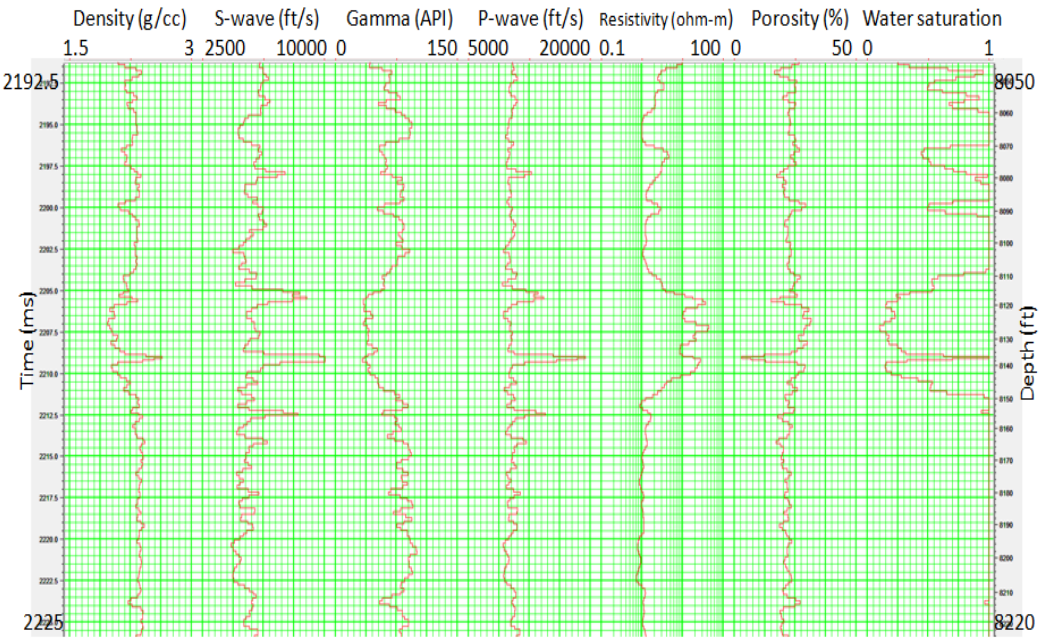

Figure 4.10: Logs showing the computed water saturation and porosity curves for Well 1.

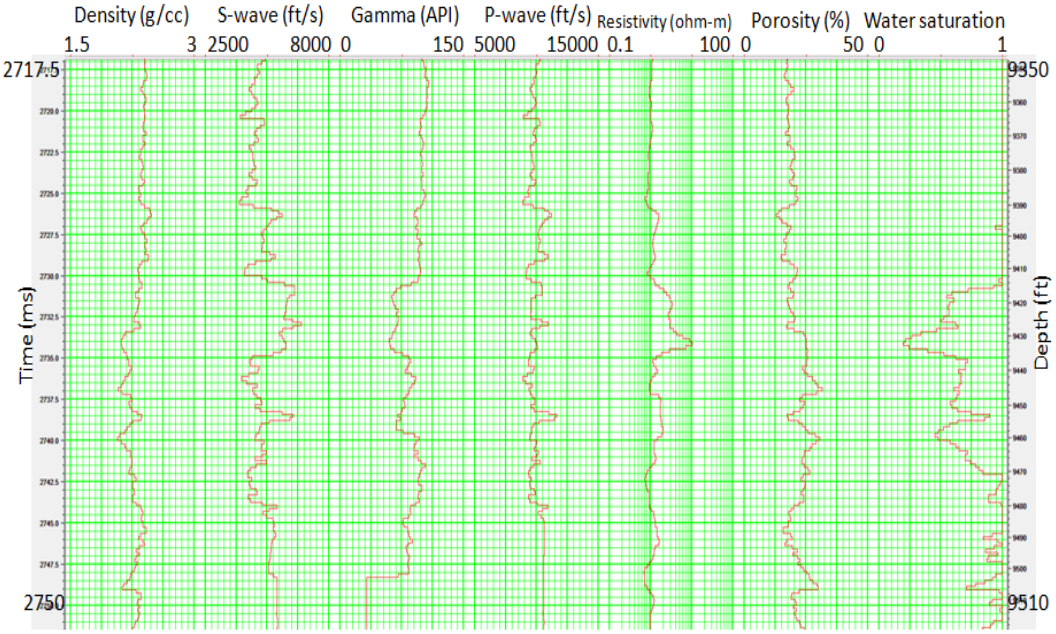

Figure 4.11: Logs showing the computed water saturation and porosity curves for Well 2.

4.3 Fluid-substitution modeling

Fluid-substitution modeling is an important part of seismic attribute studies because it provides the interpreter with a valuable tool for modeling the seismic responses for various fluid scenarios, which then assist to explain an observed AVO anomaly (Smith et al., 2003). In this research, fluid-replacement modeling (FRM) is carried out for brine- and gas-saturated reservoir sands. There are two sets of equations involved in fluid substitution. The first is Gassmann's equation, which relates the bulk moduli of the porous rock frame, mineral matrix, and the pore fluids. The second set is the Batzle and Wang equations (Batzle and Wang, 1992), which provide the bulk moduli and density of the pore fluids as a function of temperature, pore pressure, specific gravity and water salinity.

The use of Gassmann's equation is based on the following assumptions, explained by Smith et al. (2003) and Wang (2001). The rock is homogenous and isotropic, all pores are interconnected and communicating, pore pressure is equilibrated throughout the rock, the pore fluid does not interact with the solid in such a way that would soften or harden the frame, and the media is closed and no pore fluid leaves the rock volume.

In the zone of interest, the in-situ fluid is gas and water (Figures 4.10 and 4.11). The gas is replaced with brine during the fluid substitution modeling. V_p and ρ_b increase when the gas portion is replaced with brine while V_s drops slightly for the upper gas-saturated reservoir 8114–8144 ft (~2473−2483 m) in Well 1 (Figure 4.12). The same procedure was carried out for Well 2 for the depth interval 9415–9436 ft (~2870−2876 m) and the results are shown in Figure 4.13.

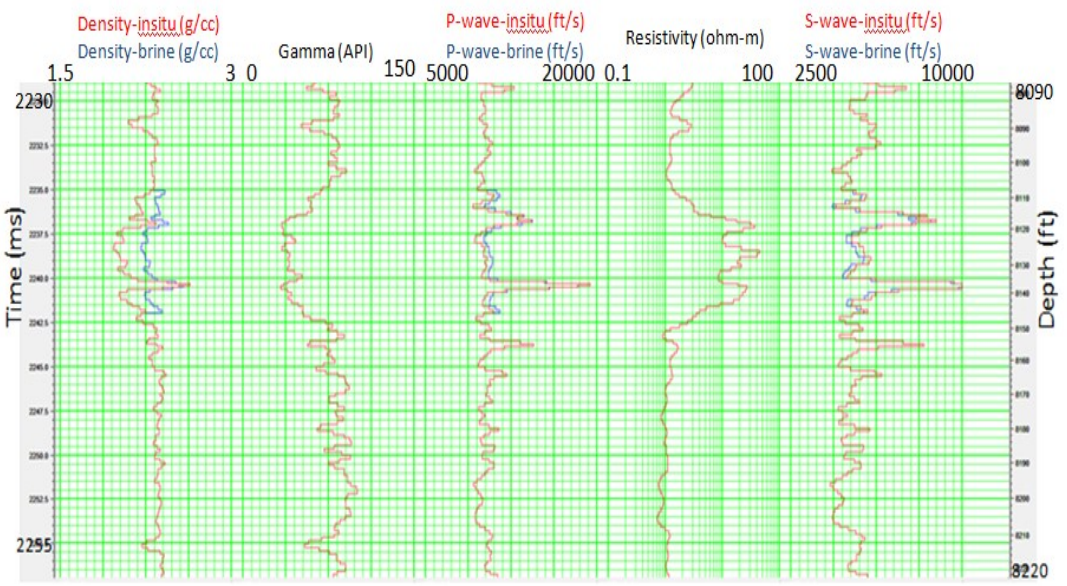

Figure 4.12: In-situ gas interval (red curve) is replaced with brine (blue curve) for Well 1.

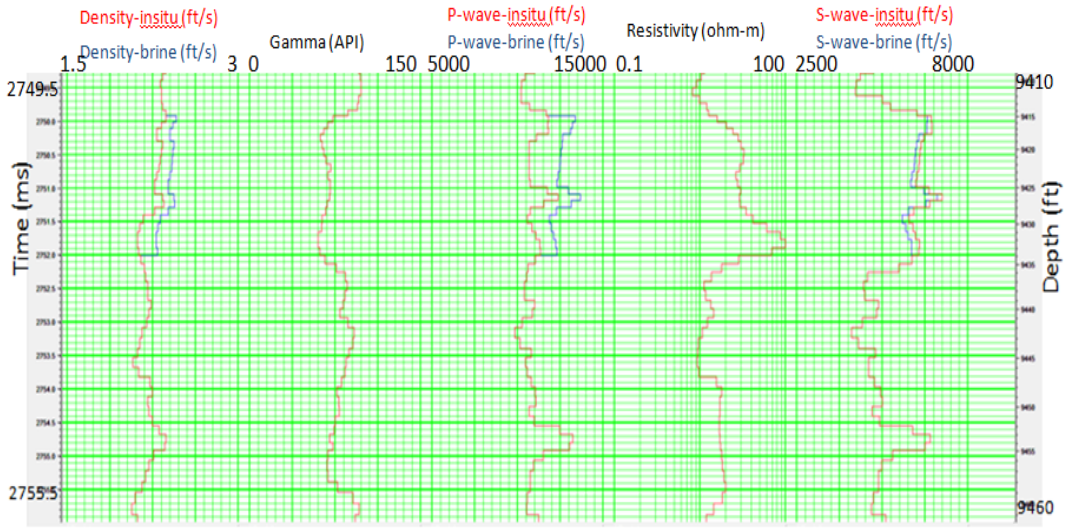

Figure 4.13: In-situ gas interval (red curve) is replaced with brine (blue curve) for Well 2.

4.4. Interpretation of results

4.4.1. V_p, V_s and ρ

In Well 1, brine substitution in the in-situ gas-saturated reservoir show a general increase in the V_p, ρ and a decrease in V_s; P-wave velocity increases from an average value of 10048 ft/s (~3063 m/s) to 10518 ft/s (~3206 m/s), S-wave velocity decreases from 5921 ft/s (~1805 m/s) to 5655 ft/s (~1724 m/s) and density increases from 2.01 g/cc to 2.23 g/cc.

4.4.2. V_p/V_s

Castagna et al. (1985) reported that the use of V_p/V_s as a lithology indicator was popularized years ago. They also reported the use of V_p, V_s and V_p/V_s in seismic exploration for estimation of lithology and saturating fluids in particular stratigraphic intervals. Because the P-wave velocity is more sensitive to fluid changes than the S-wave velocity, changes in fluid type result in changes in V_p/V_s. Here, it is observed that V_p/V_s ratio for hydrocarbons is generally lower than brine. In Well 1, the values of V_p/V_s in the upper and lower gas-saturated reservoir are approximately 1.60 and 1.61 respectively while brine-saturated sand has a V_p/V_s ratio value of 1.92.

4.4.3. Impedance

Acoustic impedance (AI) is the product of P-wave velocity and density. Generally, acoustic impedance values can help in identifying reservoir pore fluid type because the addition of gas to a reservoir lowers both the P-wave velocity and density and thus AI. Hence, a gas-filled reservoir is expected to have a lower AI value as compared to the surrounding shale, however, this is not the case in my study area. Gas-saturated reservoir AI values in Class 2 AVO environment are approximately equal to the surrounding shale and this makes AI a bad fluid indicator in this environment. Figures 4.14 and 4.15 show the AI logs for wells 1 and 2.

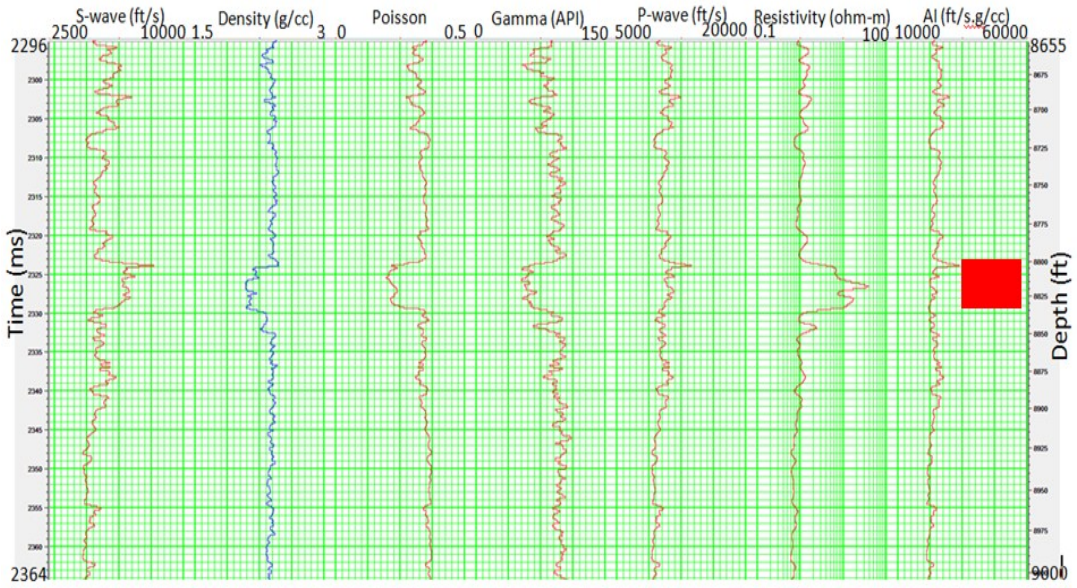

Figure 4.14: Well-log curves including AI for Well 1. The red rectangle represents the hydrocarbon zone.

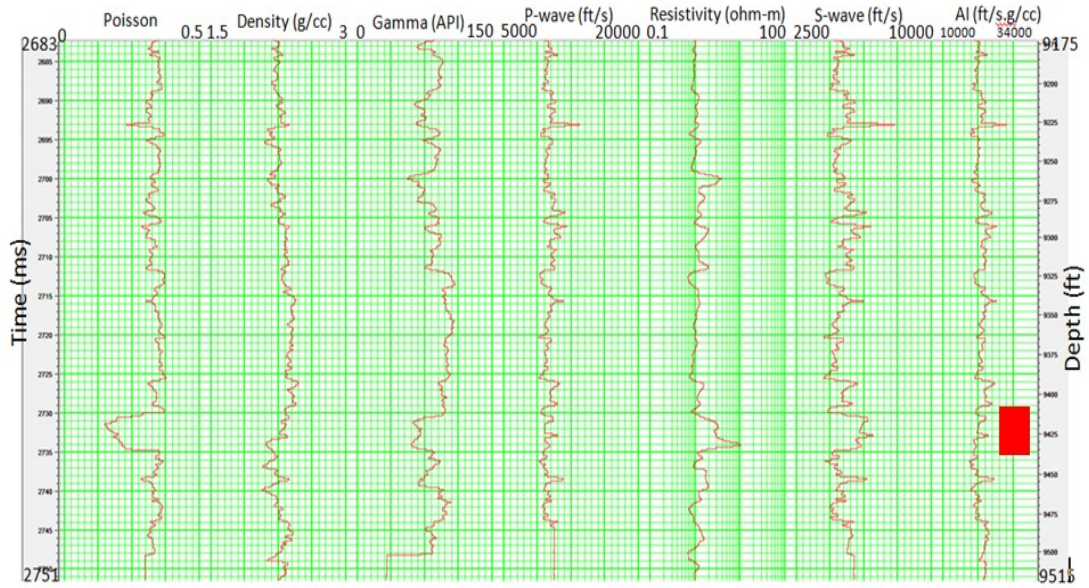

Figure 4.15: Well-log curves including AI for Well 2. The red rectangle represents the hydrocarbon zone.

4.5. Synthetic AVO models

Chiburis et al. (1993) stated that "the key to using AVO for fluid identification is comparison of real data with a synthetic seismogram". In this research, Hampson-Russell's AVO is used in the generation of AVO synthetic seismograms both for Well 1 and Well 2. Synthetics are generated for two offset ranges i.e. between 1000−11476 ft (~305−3498 m) and 1000–15483 ft (~305−4719 m) with the use of the linear approximation of Zoeppritz equations. The results are compared to the CMP field gathers at the well locations (Figures 4.16 and 4.17). The Zoeppritz equation calculates the amplitudes of seismic waves and considers only plane-wave amplitudes of reflected P-waves and ignores interbed multiples and mode converted waves (Hampson and Russell, 1999). The generation of the synthetics also takes into account transmission losses and geometric spreading and requires as input the P-wave curve (time-depth function) generated after well-to-seismic tie, S-wave velocity, density, and final extracted wavelets.

The in-situ AVO synthetics for Well 1 and 2 are shown in Figures 4.16 and 4.17. Also, the overplots of the incident angles are displayed on the synthetics in increment of 10°. The seismic events of interest are the hydrocarbon intervals. Unfortunately, overall the in-situ AVO synthetics are a poor tie to the field CMP gather located at the well locations. However, the two hydrocarbon zones in Well 1 do have a resemblance to the field data in Figure 4.16.

Satisfactory fluid-substitution AVO modeling was not achieved in the H-R software and this is seen in the lack of difference between hydrocarbon-charged and brine-saturated AVO signatures. Due to this lack of difference, I decided to carry out a detailed modeling for the two reservoirs of interest in Well 1 and the one reservoir in Well 2 using the TIPS software. Figures 4.18 and 4.19 show the results of the detailed modeling for the two reservoirs in Well 1 and the AVO signature for the reservoir in Well 2 is shown in Figure 4.20. These AVO signatures show appreciable difference between reservoirs charged with and without hydrocarbons.

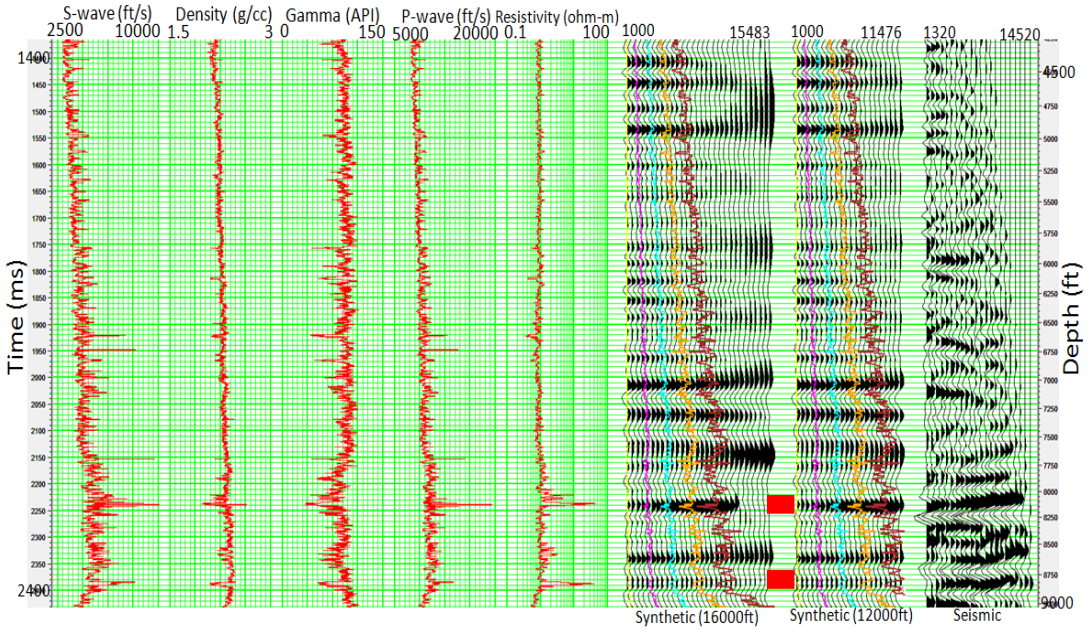

Figure 4.16: In-situ AVO gas synthetic with the incident angles in increments of 10° (5°- 45°) displayed on the offsets (Well 1). The red rectangles represent the hydrocarbon zones.

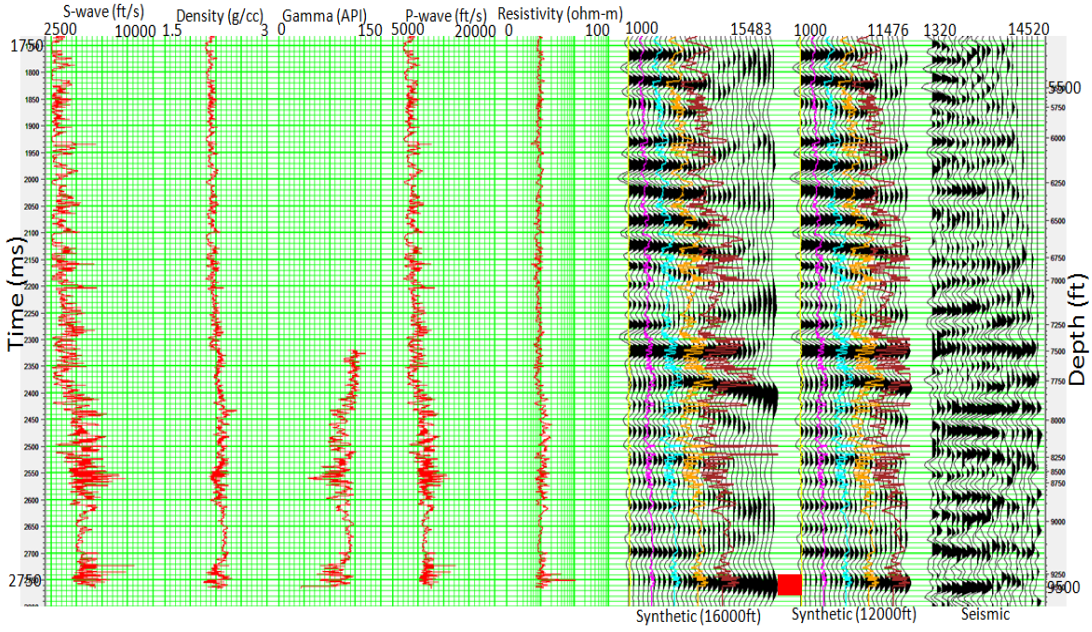

Figure 4.17: In-situ AVO gas synthetic with incident angles in increments of 10° (5°- 45°) displayed on the offsets (Well 2). The red rectangle represents the hydrocarbon zone.

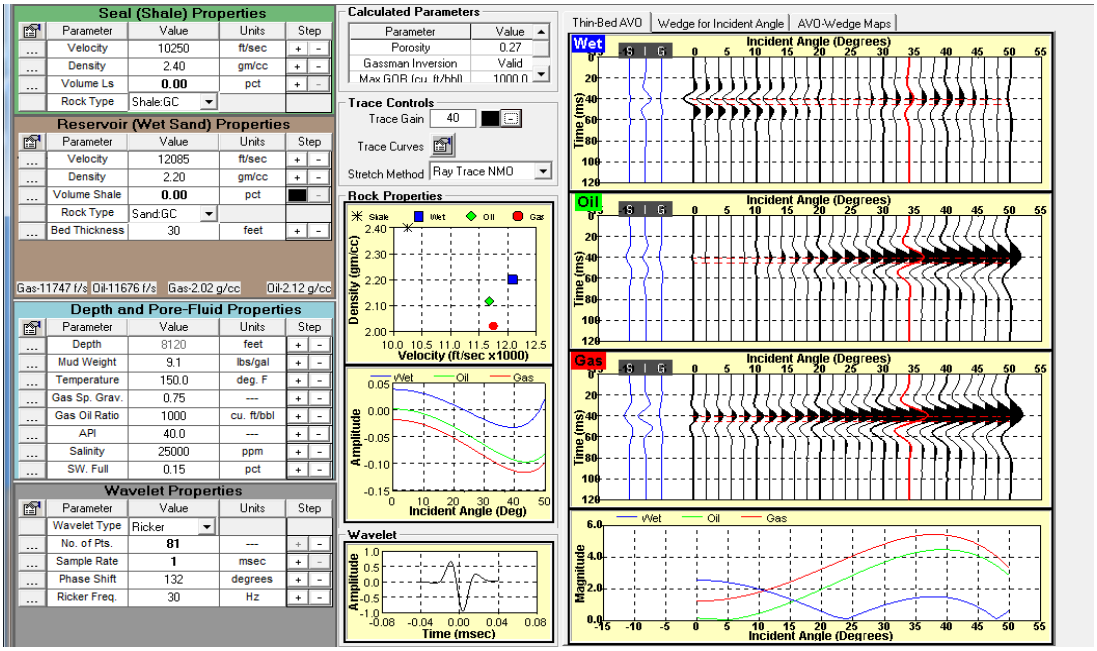

Figure 4.18: Detailed modeling of the upper reservoir in Well 1 showing the AVO signature for brine, oil and gas using a phase of 132°.

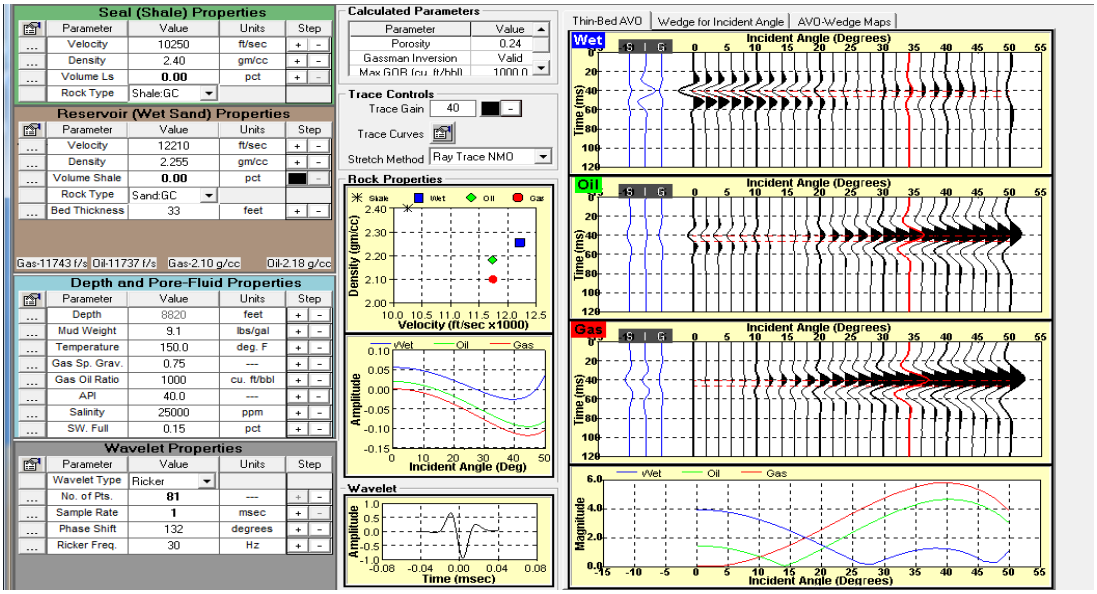

Figure 4.19: Detailed modeling of the lower reservoir in Well 1 showing the AVO signature for brine, oil and gas using a phase of 132°.

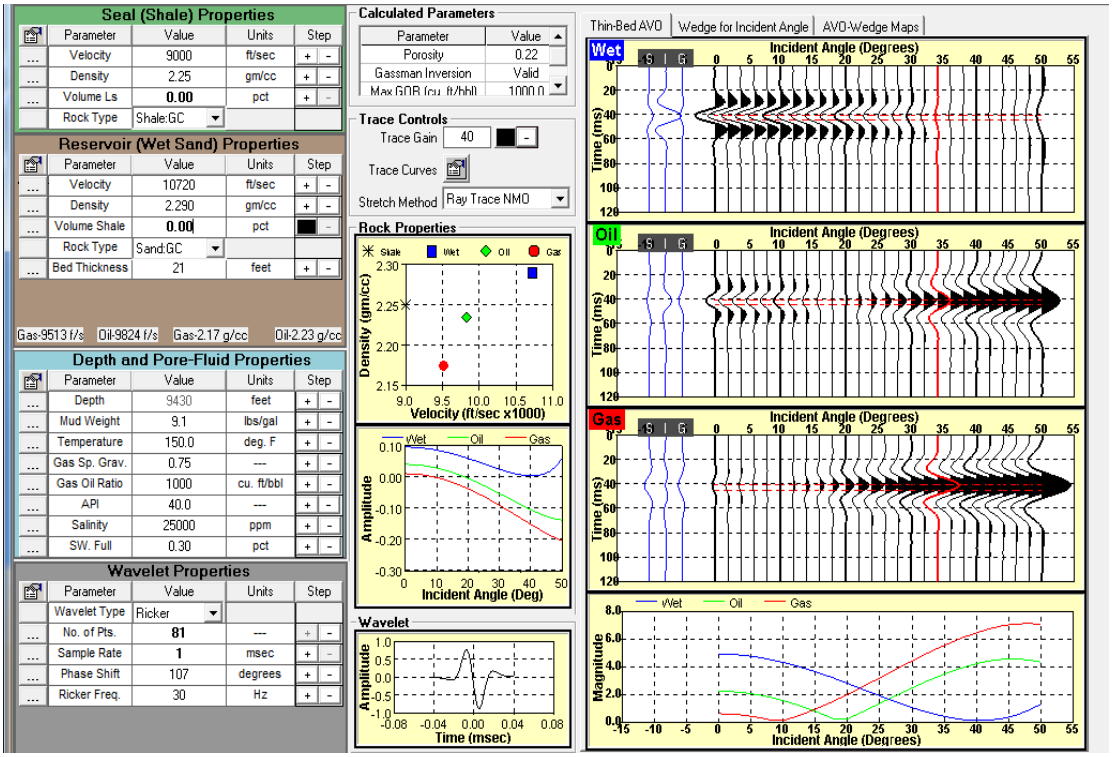

Figure 4.20: Detailed modeling of the deeper reservoir in Well 2 showing the AVO signature for brine, oil and gas using a phase of 107°.

CHAPTER 5

INVERSION OF SEISMIC DATA

5.1 Introduction

Inversion literally means to undo an operation (Veeken, 2007). Russell (2005) defined it as "the process of extracting from seismic data, the underlying geology which gave rise to that seismic". This process aims at reconstructing subsurface features from geophysical measurements such that the model response "fits" the observation with some measure of error (Trietel and Lines, 2001).

Acoustic Impedance (AI) is the product of density (ρ) and P-wave velocity (V_p) of a rock,

$$AI = \rho * V_p \tag{5.1}$$

The gas-saturated reservoir in my study area has approximately equal acoustic impedance values as the surrounding shale, this makes it difficult to discriminate between the reservoir and the surrounding shale on a zero-offset seismic data. As offset increases though, the gas-saturated reservoir should be easier to differentiate from the shale. Hence, there is a need to analyze non-zero offset seismic data. The derivation of the subsurface geology or elastic parameters from this non-zero offset data is achieved through elastic impedance.

Elastic Impedance (EI) is the generalization of "pseudo impedances" for variable incident angles (Connolly, 1999). Connolly added that it also enables one to calibrate and invert non-zero offset seismic data similar to AI inversion of zero offset data, and it is a function of P-wave velocity (V_p), S-wave velocity (V_s), density (ρ) and incident angle (θ). EI is expressed as,

$$EI(\theta) = V_p^{\,a} * V_s^{\,b} * \rho^c \tag{5.2}$$

where $a = 1 + \tan^2\theta$,

$b = -8K\sin^2\theta$,

$c = 1 - 4K\sin^2\theta$ and

K is a constant that is taken to be the average of $(V_s/V_p)^2$

EI decreases with increasing angle compared to AI at normal incidence as shown in Figure 5.1 (Connolly, 1999). Veeken (2007) pointed out that EI inversion exploits AVO effects on angle stacks and that the far offsets often give more details about the fluid content compared to the near-angle stack. EI is important especially in a Class 2 environment where the large amplitude increase is usually observed at the far offsets as compared to near offsets. To illustrate this AVO effect, I generated elastic impedance logs at three angles of incidence (0°, 20° and 40°) to show what happens at the reservoir and outside the reservoir (Figure 5.2). It can be observed that the value of elastic impedance decreases dramatically with increasing angle within the reservoir while the opposite is observed outside of the reservoir.

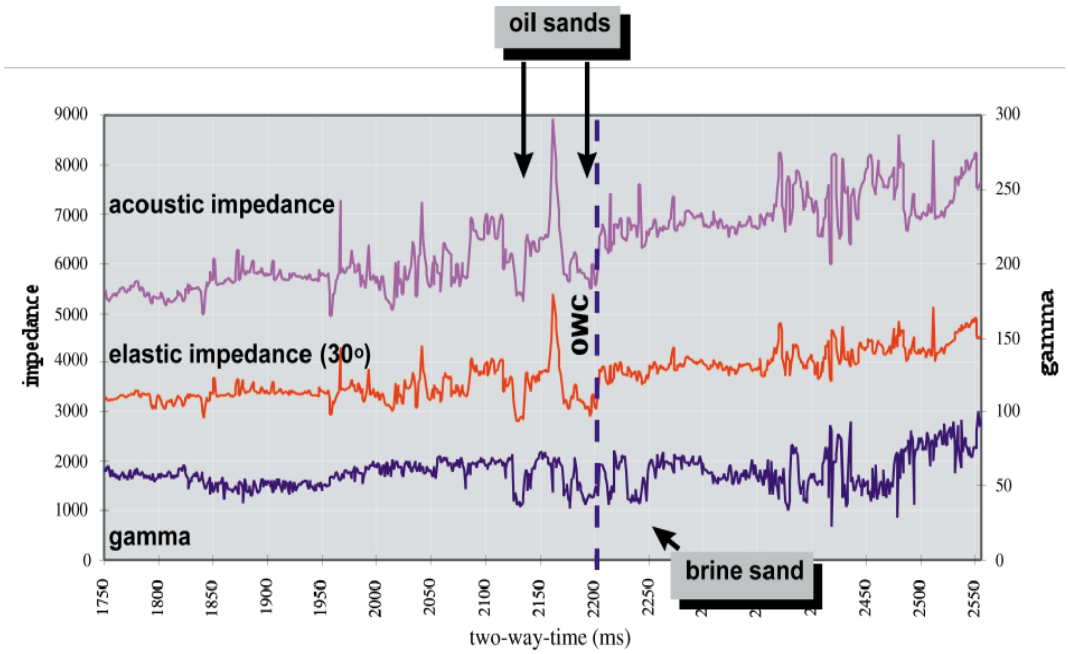

Figure 5.1: Comparison of elastic impedance and acoustic impedance (after Connolly, 1999).

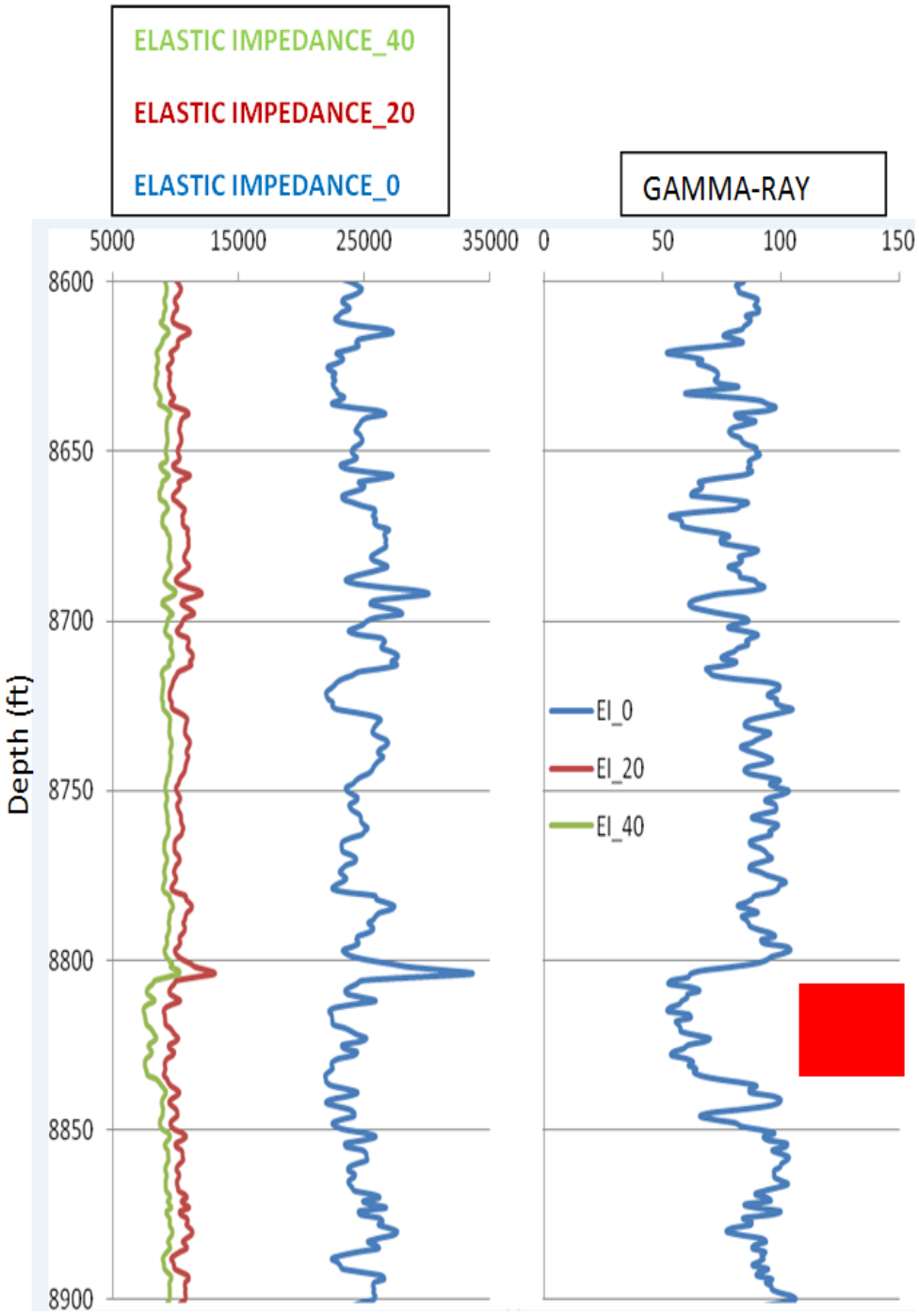

Figure 5.2: Plot of elastic impedance logs at 0, 20 and 40 degrees (the red rectangle represents the hydrocarbon zone).

5.1.1 Benefits of impedance data

As discussed by Veeken (2007), Latimer et al. (2000) and Savic et al. (2000), the benefits of impedance data are:

- Unlike seismic data, which is an interface property, AI is a rock property and it is presented as geologic layers.
- It contains essential data from the log (not applicable to relative impedance inversion) and all information from seismic. It also gets rid of the complexities such as false stratigraphy caused by wavelet side lobes.
- It is closely related to lithology and reservoir characteristics such as, porosity, pore fluid and hydrocarbon saturation.
- As a result of the broader bandwidth of the impedance data, vertical resolution is maximized, while wavelet tuning effect is reduced.

5.2 Inversion methods

Francis (2002) stated that most impedance inversion methods are deterministic, as they are based on minimizing the difference between the seismic trace and the convolution of the solution of the inversion with the estimated wavelet. In this research, two inversion methods: elastic impedance and extended elastic impedance inversions are carried out. The elastic impedance inversion is applied to both near- and far-angle stacks, and an extended elastic impedance inversion is carried out to generate five seismic attributes (V_p/V_s, bulk modulus, Lamé constant, shear modulus and shear impedance). Comparisons of these are made to ascertain the sensitivity of each method to reservoir fluid, dependence of inversion results on the initial model, and reliability of inversion results.

In Figure 5.1, the baseline value of the elastic impedance decreased with increasing incident angle. This offset occurs because EI does not always represent a physical property as AI does. When velocity is taken to a non-zero power or a power of one, the significance of a physical property is lost. This dilemma is overcome by EEI.

5.2.1 Elastic impedance inversion

Connolly (1999) stated that elastic impedance (EI) is a generalization of acoustic impedance for variable incident angle. EI provides a consistent and absolute framework to calibrate and invert nonzero-offset seismic data just as AI does for zero offset data. EI is a function of P-wave velocity, S-wave velocity, density, and incidence angle as seen in equation 5.2 and to relate it to seismic, angle stacks must be available. Generally Class 2 anomalies show a poor signal-to-noise ratio on near-trace data whereas the far-offset data are generally of better quality. EI allows the well data to be tied directly to the high-angle seismic which can then be calibrated and inverted without reference to the near offsets. A better relation to rock properties is achieved when AI and EI are combined together as opposed to using shear wave velocity or Poisson's ratio logs (Connolly, 1999).

In this research, near- and far- angle stacks are provided with an angle range of (2-15°) and (15-42°) respectively. After correlating the offset synthetics to the angle stacks as best as possible, I extracted wavelets for EI inversion. For Well 1, the synthetic generated at 8.5° using the elastic impedance equation (5.2) was tied to the near-angle stack and a near-angle wavelet is extracted between 1400 ms and 2400 ms. Also, a far-angle wavelet between the same time range was extracted from the tie of the synthetic generated at 28.5° with the far-angle stack. A post stack (model-based) inversion was then carried out on both stacks. This inversion requires building an initial low frequency model for each stack. For the near stack, the initial low-frequency model requires three log curves, P-wave generated after well to seismic tie (time-depth

function), S-wave, and density from Well 1, a smoothing filter that is applied to the modeled trace at Well 1 location (frequencies above 15 Hz were removed from the data), horizons picked (helps to interpolate for all traces over the whole seismic volume) and incident angle. I followed the same procedure for the far-angle stack except to change the incidence angle to 28.5°. Two separate models are thus created and each model requires the use of an individual wavelet. The wavelet I used for the near stack is the near wavelet I extracted earlier (2-15°) while I used the far wavelet (15-42°) for the far-angle stack. The models built are shown in Figures 5.3 and 5.4.

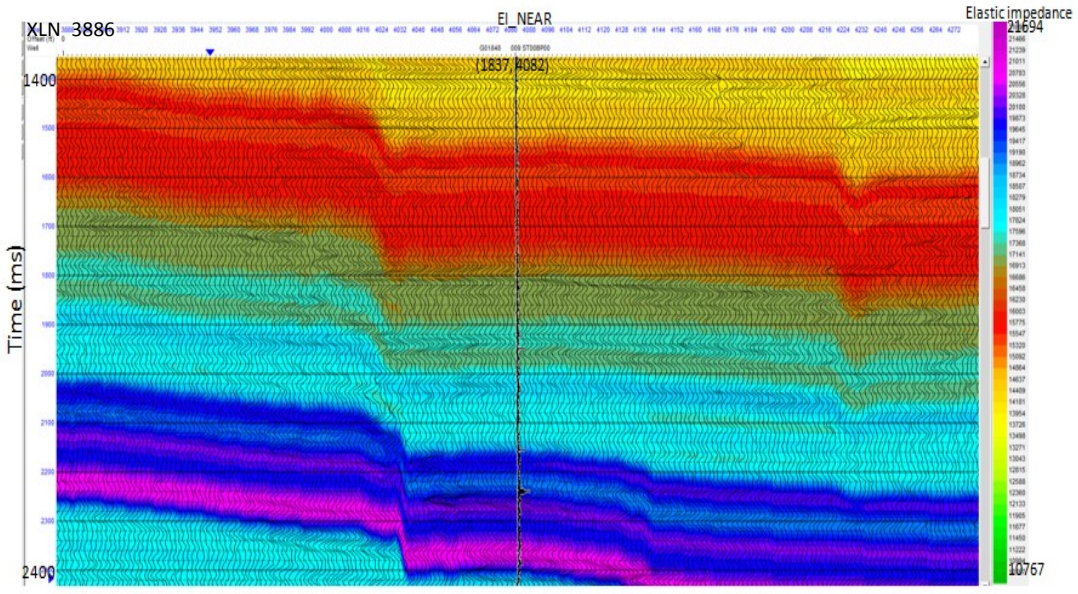

Figure 5.3: Initial EI model for the near-angle stack inversion that traverses Well 1 (Inline 1837).

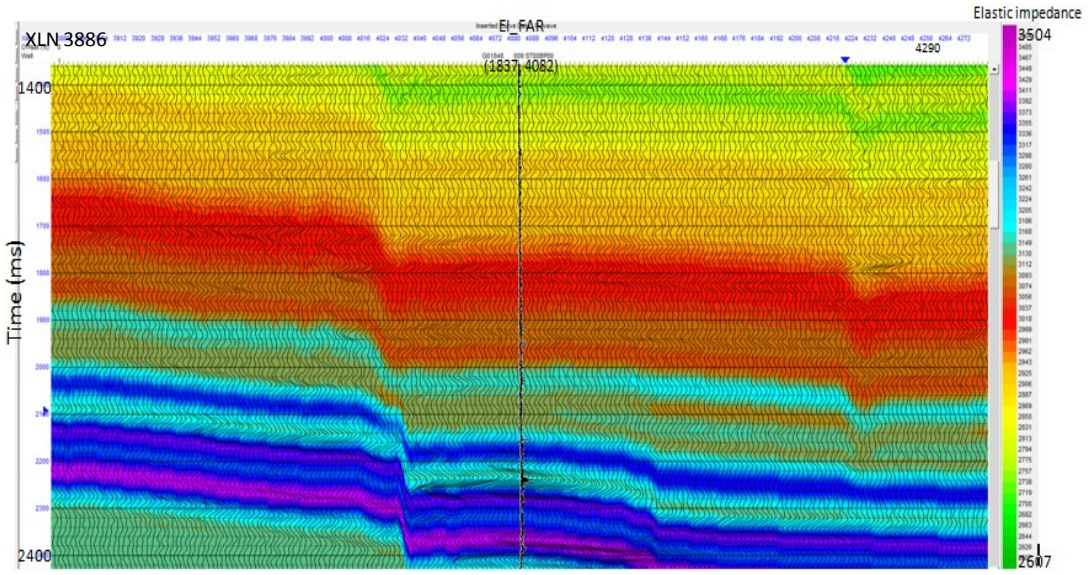

Figure 5.4: Initial EI model for the far-angle stack inversion that traverses Well 1 (Inline 1837).

The final step is the inversion of the near- and far- angle stacks at angles 8.5° and 28.5° respectively. This involves two separate inversions. The background information for the inversion is provided by the well-log curves (P-wave, S-wave, and density), additionally, the AVO information from the seismic data is required and this information is derived from the reflectivities that are assumed to be based on the approximations of the Zoeppritz's equation. The elastic inversion of the near- and far-angle seismic cubes provides the elastic impedance estimate at 8.5° and 28.5° respectively. The results of the inversions are shown in Figures 5.5 and 5.6. The far-angle EI inversion in Figure 5.6 is encouraging because both hydrocarbon reservoirs in Well 1 are discriminated by the low EI values at approximately 2240 and 2380 ms. However, the same discrimination was observed on the far-angle stack shown in Figure 3.2.

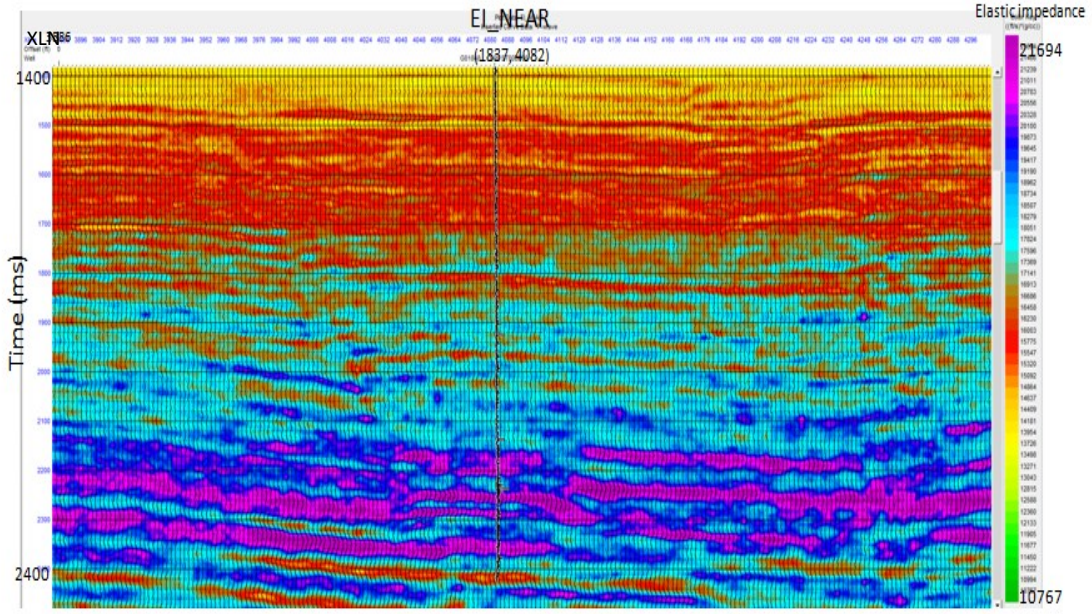

Figure 5.5: Elastic impedance volume from inversion of near-angle stack that traverses Well 1 (Inline 1837).

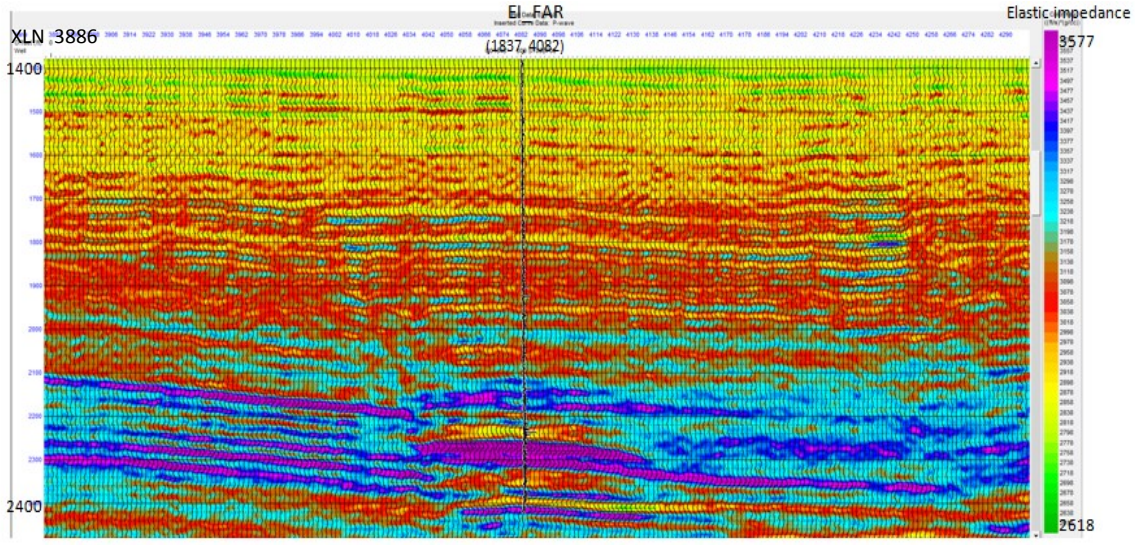

Figure 5.6: Elastic impedance volume from inversion of far-angle stack that traverses Well 1 (Inline 1837).

The second well was also inverted for elastic impedances at the near and far angles. The results of the inversion are shown in Figures 5.7 and 5.8.

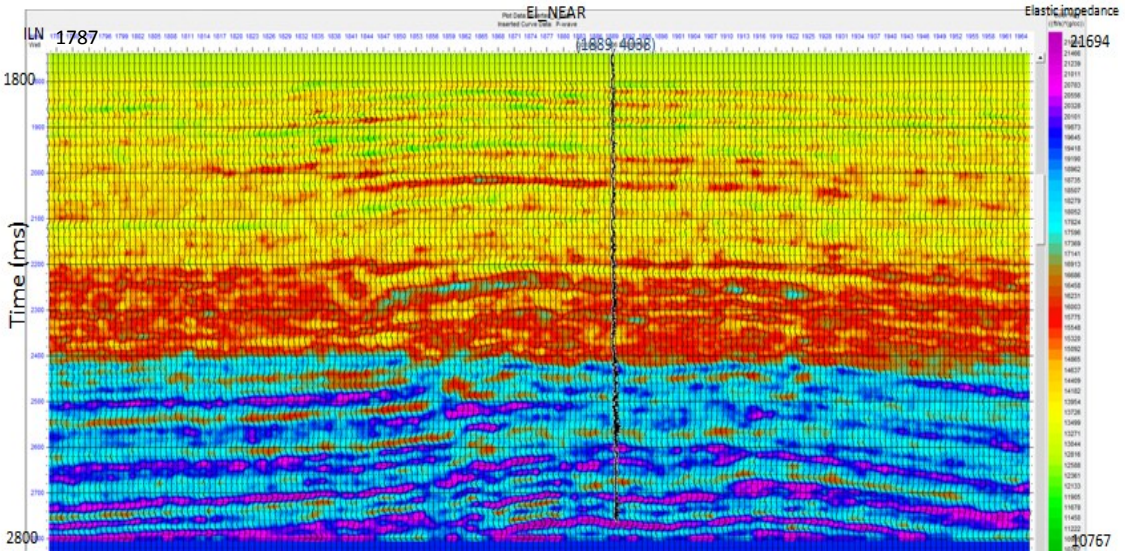

Figure 5.7: Elastic impedance volume from inversion of near-angle stack that traverses Well 2 (Crossline 4038).

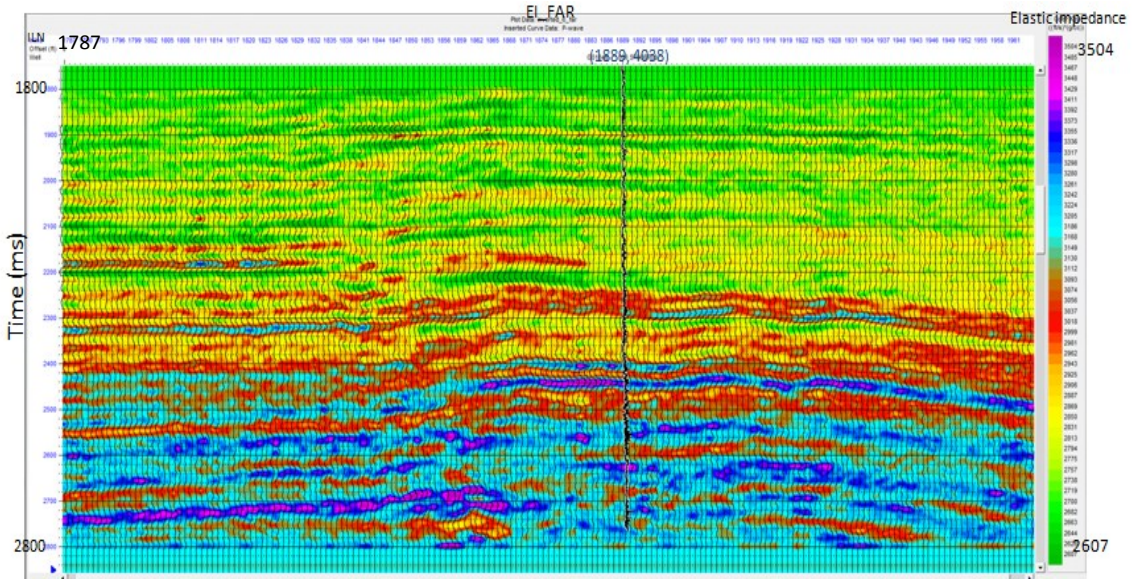

Figure 5.8: Elastic impedance volume from inversion of far-angle stack that traverses Well 2 (Crossline 4038).

5.2.2 Extended elastic impedance

Extended elastic impedance (EEI) is an extension of the elastic impedance and it is the optimum projection for a noise free, isotropic environment. EEI allows arbitrarily large positive or negative values of $\sin^2\theta$ and it also approximates several elastic parameters which include bulk modulus, shear modulus and Lamé's parameters (Whitcombe et al, 2002). EEI allows the use of a range of physically non-meaningful incident angles by substituting $\tan\chi$ for $\sin^2\theta$ in the two-term reflectivity equation. Thus, the primary variable now becomes χ rather than θ and it is varied from -90 to 90° as seen in Figure 5.9 (Whitcombe et al, 2002). The expression for the EEI is shown in equations 5.3 and 5.4.

$$EEI(\chi) = \alpha_o \rho_o [\alpha/\alpha_o]^p [\beta/\beta_o]^q [\rho/\rho_o]^r \quad 5.3$$

$p = \cos(\chi) - \sin(\chi)$

$q = -8K\sin(\chi)$

$r = \cos(\chi) - 4K\sin(\chi)$

$K = (\beta/\alpha)^2$ which is locally constant

$$EEI(\chi) = AI_o[(AI/AI_o)^{\cos\chi}(GI/AI_o)^{\sin\chi}] \quad 5.4$$

AI= acoustic impedance= $EEI(\chi=0)$

GI=gradient impedance= $EEI(\chi=90)$

$NI = 0.5\ln AI_2 - 0.5\ln AI_1$ and $B = 0.5\ln GI_2 - 0.5\ln GI_1$

$RC(\theta) = NI + B\sin^2(\theta)$ and $\sin^2(\theta) = \tan\chi$

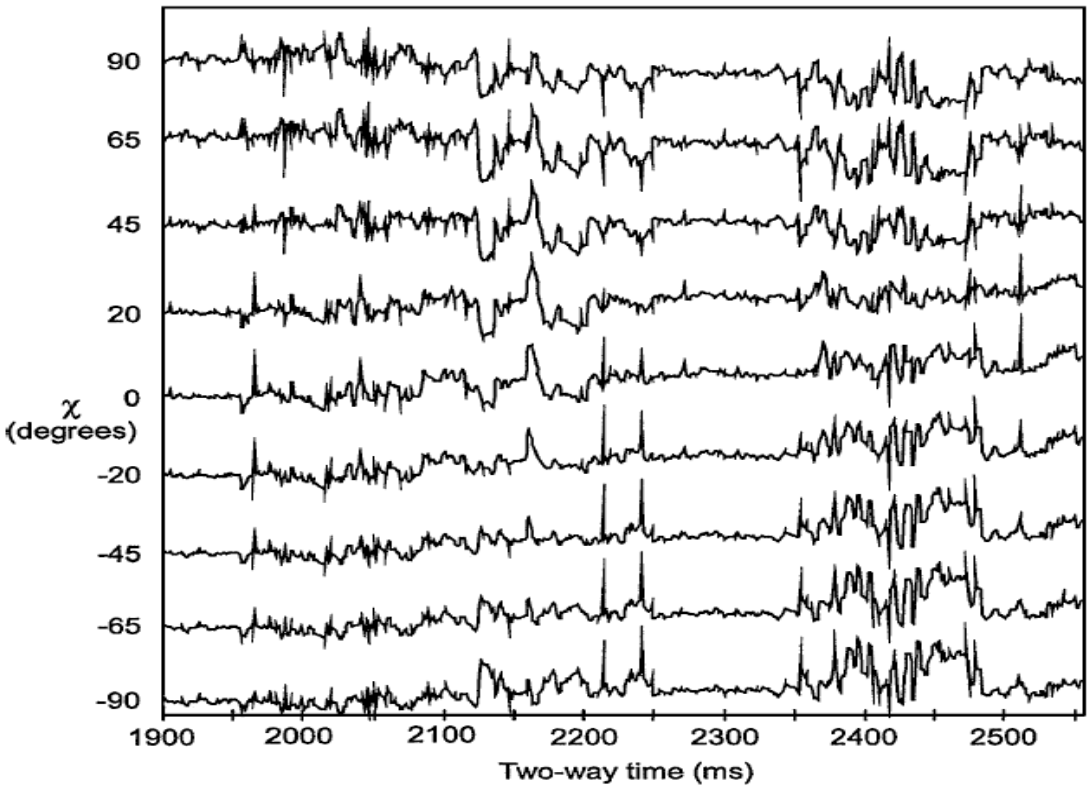

Figure 5.9: The EEI functions for various χ values. Note the inverse correlation between EEI(χ = 90) and EEI(χ = -90). (Whitcombe et al, 2002).

The EEI values at different angles χ correspond to different elastic parameters such as acoustic impedance, bulk modulus, shear impedance, Lamé parameters (μ and λ) and V_p/V_s (Figure 5.10). Hence logs for these parameters can be generated using the EEI equation and compared to similar logs generated from the well-log curves. EEI logs can be directly related to the petrophysical properties of interest. Some of these parameters can be used for prediction of lithology and fluid content of a reservoir. Whitcombe et al. (2002) stated "bulk modulus and Lamé's parameter tend to lie within an area of EEI space with values of χ from about 10° to 30°, and shear modulus lies within a range of χ from about -30° to -90°. These areas are therefore likely to be good starting points to look for optimum fluid and lithology impedance functions

respectively". Figure 5.11 is a map generated for a reservoir in the central North Sea to show lithology and fluid imaging using EEI.

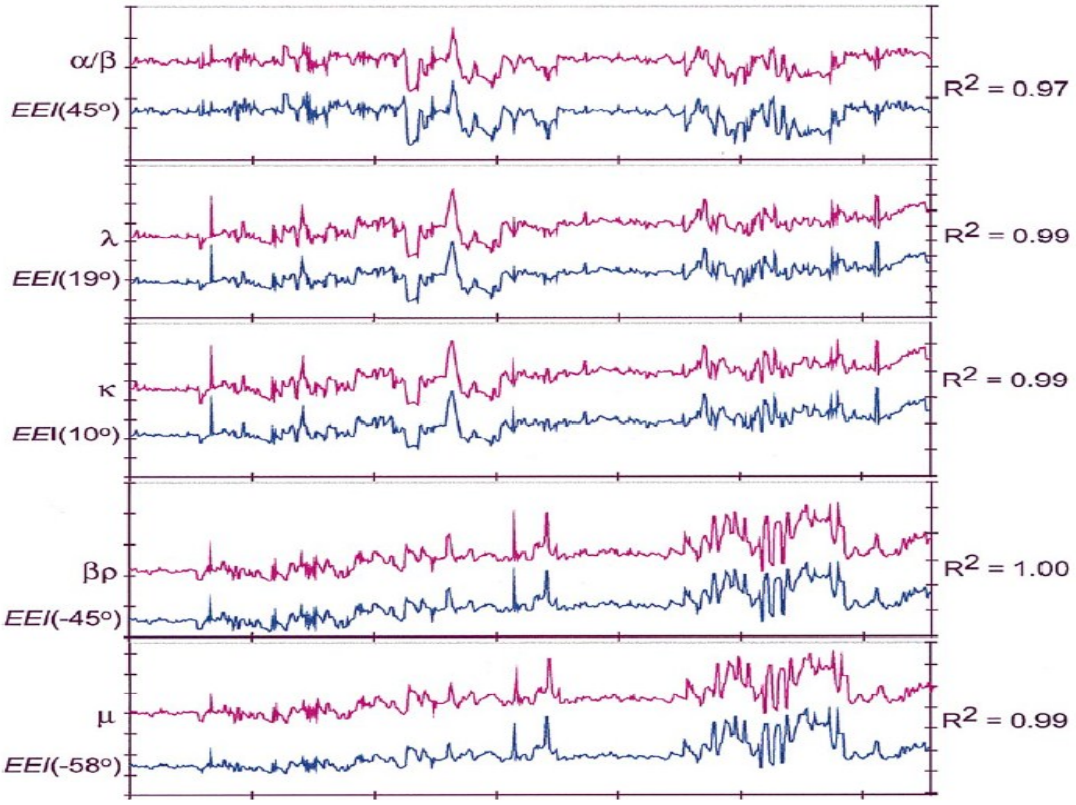

Figure 5.10: Comparisons between elastic parameters and equivalent EEI curves, showing the high degree of correlation. The EEI function is defined as a function of the angle χ, not the reflection angle θ (Whitcombe et al., 2002).

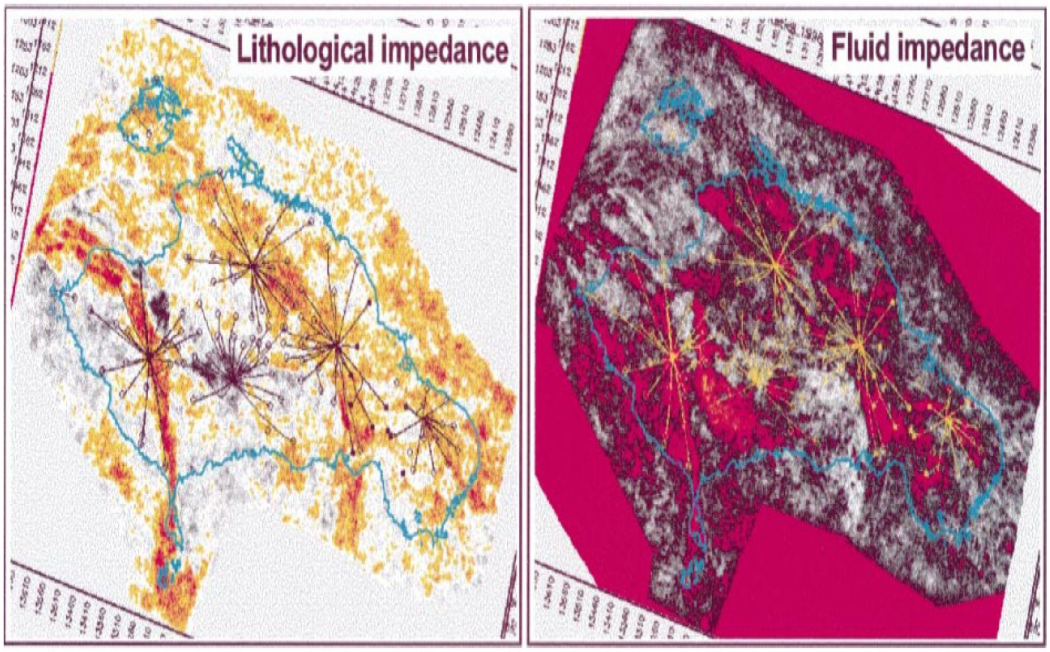

Figure 5.11: Maps generated using EEI data sets using χ values tuned to optimize the imaging of lithology (χ = -51.3°) and fluids (χ = 12.4°) respectively (Whitcombe et al., 2002).

5.2.2.1 Attributes generated using extended elastic impedance

Well-log data and seismic data are in two different domains i.e. depth and time respectively. To ensure consistency in the elastic parameters from the well logs and those from the seismic, some form of well calibration to seismic is required. The following steps summarize how I achieved this and the steps also show how EEI can be used for fluid and lithology imaging.

STEP 1:

A. Generate the seismic attributes $\alpha/\beta_{log}(z)$, $K_{log}(z)$, $\mu_{log}(z)$, $\lambda_{log}(z)$ and $SI_{log}(z)$ from the P-wave, S-wave, and density logs in the zone of interest 6300 ft – 9000 ft (~1920 m – 2743 m) using the following equations :

Ratio of P-wave velocity and S-wave velocity = α/β 5.5

Bulk modulus (K) = $\rho\alpha^2 - (4/3)\,\rho\beta^2$ 5.6

Lamé constant (λ) = $\rho\alpha^2 - 2\rho\beta^2$ 5.7

Shear modulus (μ) = $\rho\beta^2$ 5.8

Shear impedance (SI) = $\rho\beta$ 5.9

B. Determine the mean (m_{log}) and standard deviation (σ_{log}) for each of the seismic attributes defined in STEP 1A in the zone of interest.

STEP 2:

A. Using the well-log curves again, generate the seismic attributes $(\alpha/\beta)_{EEI}(z)$, $K_{EEI}(z)$, $\mu_{EEI}(z)$, $\lambda_{EEI}(z)$ and $SI_{EEI}(z)$ (Whitcombe et al., 2002) from the EEI equation shown below at χ angles of 45°, 12°, -51.3°, 20°, and -45° respectively.

$$EEI(\chi) = \alpha_o\rho_o(\alpha/\alpha_o)^p(\beta/\beta_o)^q(\rho/\rho_o)^r \quad 5.10$$

where,

α_o is the average value of P-wave velocity in the zone of interest,

β_o is the average value of S-wave velocity,

ρ_o is the average value of density,

$p = \cos(\chi) - \sin(\chi)$,

$q = -8k\sin(\chi)$,

$r = \cos(\chi) - 4k\sin(\chi)$ and

$k = (\beta/\alpha)^2$.

B. Determine the mean (m_{EEI}) and the standard deviation (σ_{EEI}) for each of the seismic attributes defined in STEP 2A in the zone of interest.

C. Normalize each of the EEI seismic attributes from STEP 2A to the well-log seismic attributes from STEP 1A. The equation below shows an example for bulk modulus:

$$K_{norm}(z) = [(K_{EEI}(z) - m_{EEI})/\sigma_{EEI}]*\sigma_{log} + m_{log} \qquad 5.11$$

D. Each of the normalized EEI seismic attributes generated in STEP 2C is plotted against their equivalent well-log derived attribute from STEP 1C to verify how well they fit. This is shown in Figure 5.12

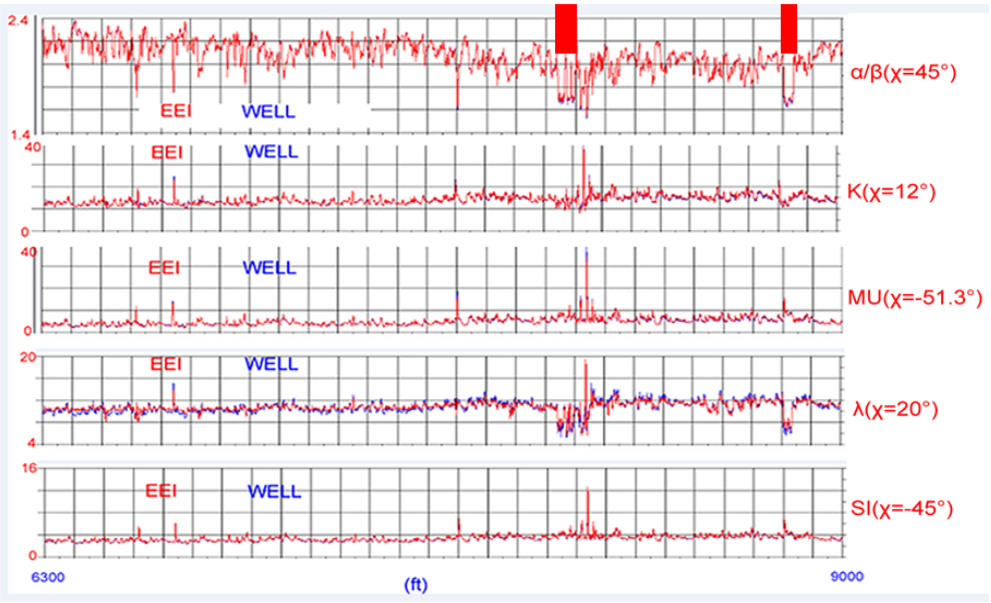

Figure 5.12: Seismic attributes derived from EEI compared to well-log derivation for Well 1. The red curves are the normalized EEI attribute curves generated from STEP 2A, the blue curves are the elastic properties generated from well-log data in STEP 1A and the red rectangles are the hydrocarbon zones.

STEP 3:

A. Generate NIP (normal-incident P-wave reflectivity), NIS (normal-incident S-wave reflectivity) and B (AVO gradient) from seismic angle stacks. Available seismic data include angle stacks [STK(θ_1,t) and STK(θ_2,t)] where the near- angle stack has an average incident angle $\theta_1 = 8.5°$ and far-angle stack, $\theta_2 = 28.5°$. From Zhou and Hilterman (2010), NIP, NIS and B are derived as:

$$NIP(t) \approx 1.11STK(\theta_1,t) - 0.11STK(\theta_2,t) \quad 5.12$$

$$NIS(t) \approx 3.18STK(\theta_1,t) - 2.51STK(\theta_2,t) \quad 5.13$$

$$B(t) \approx NIP(t) - 2NIS(t) \quad 5.14$$

B. Generate acoustic impedance AI(t) and gradient impedance GI(t) from the seismic field data NIP(t) and B(t) respectively. This is achieved by integrating (inverting) NIP(t) and B(t) to AI(t) and GI(t) respectively. In the inversion of NIP(t), an initial model (acoustic impedance) is built at the well location and it requires the sonic (P-wave) well-log curve derived from the synthetic to seismic tie, the well-log density curve and the seismic wavelet extracted after the tie of the near-angle stack to the synthetic. The well-log P-wave and density curves, which have been converted to time, are filtered to remove the high frequency leaving a low-frequency trend of the acoustic impedance. An inversion is then generated with Hampson-Russell software (H-R) on the NIP(t) trace incorporating the low-frequency acoustic impedance from the well logs. The low- frequency acoustic impedance is then interpolated over the whole seismic volume using the picked horizons. With the field data NIP(t) volume and the low-frequency acoustic impedance volume, an AI(t) volume is generated.

C. The seismic inversion of B(t) to GI(t) requires an initial low-frequency model of the gradient impedance. However, H-R doesn't have this option and a modified acoustic impedance inversion using H-R was applied. In order to generate low-frequency gradient impedance from the acoustic impedance inversion, a new density curve (ρ_n) is generated. This new density curve is derived considering the fact that an initial acoustic impedance model is required for the inversion to derive gradient impedance. An expression for gradient impedance is derived first using the EEI equation as seen below.

$$\text{Gradient Impedance} = EEI(\chi=90°) \qquad 5.15$$

$$EEI(\chi) = \alpha_o\rho_o(\alpha/\alpha_o)^p(\beta/\beta_o)^q(\rho/\rho_o)^r,$$

$$p = \cos 90° + \sin 90° = 1,$$

$q = -8k\sin 90° = -8k,$

$r = \cos 90° - 4k\sin 90° = -4k,$

$k = (\beta/\alpha)^2 \approx 0.25$

$EEI(90°) = \alpha_o\rho_o(\alpha/\alpha_o)(\beta/\beta_o)^{-2}(\rho/\rho_o)^{-1} = (\alpha/\beta)(\rho_o\beta_o)((\rho_o\beta_o)/\rho\beta),$

$\alpha/\beta = 2$, ρ_o and β_o are constants, this implies,

$EEI(90°) = C/(\rho\beta)$ and $C = 2(\rho_o\beta_o)^2$

Since I am building an acoustic impedance model for the H-R inversion, I equate the acoustic impedance of the new density curve to the gradient impedance expression, this implies;

$$\alpha\rho_n = C/(\rho\beta) \qquad 5.16$$

$$\rho_n = C/(\alpha\rho\beta) \qquad 5.17$$

This new-pseudo density curve is then used for the inversion. In the inversion of seismic B(t) to GI(t), an initial model (gradient impedance) is built at the well location and it requires the sonic P-wave curve derived from the synthetic to seismic tie, the new density curve ρ_n, the wavelet extracted after the correlation of the seismic far-angle stack to the far-angle synthetic. The P-wave and density curve (ρ_n), which have been converted to time, are filtered to remove the high frequency leaving a low-frequency trend of the gradient impedance. An inversion is then run on the B(t) trace incorporating the low- frequency trend. After examining the inversion at the well location, the low-frequency trend of the gradient impedance is interpolated over the whole seismic volume using the picked horizons and a GI(t) volume is then generated.

D. After the seismic AI(t) and GI(t) are derived from the field data, the seismic attribute volumes α/β-(t), K-(t), μ-(t), λ-(t) and SI-(t) are generated using equation 5.18 (Whitcombe et al., 2002) below with χ values of 45°, 12°, -51.3°, 20°, and -45° respectively. Figures 5.13 to 5.17 show these seismic attribute volumes.

$$EEI(\chi) = [AI_o(AI(t)/AI_o)^{\cos(\chi)} (GI(t)/AI_o)^{\sin(\chi)}] \quad 5.18$$

where AI_o is the average value of AI at the well location.

Then, the mean (m_t) and standard deviation (σ_t) at the zone of interest is determined for each of the seismic attribute traces.

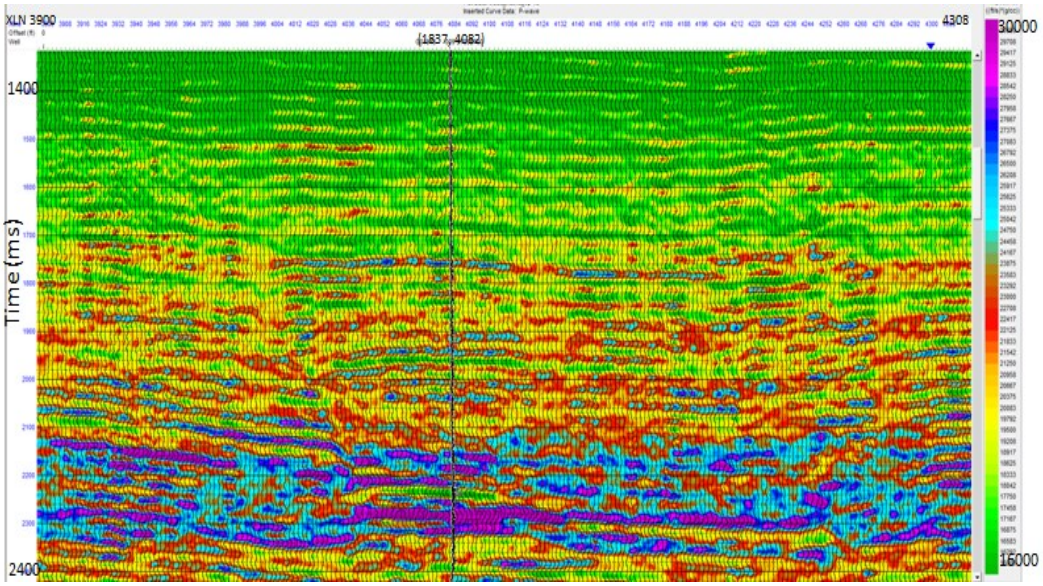

Figure 5.13: V_p/V_s seismic attribute volume for Well 1 calculated at angle χ of 45°.

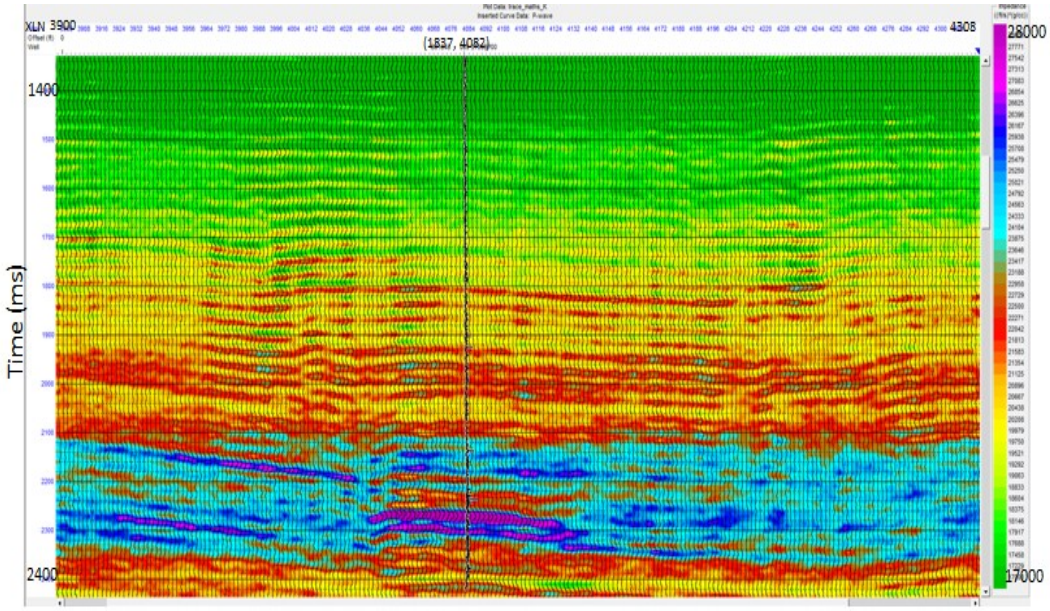

Figure 5.14: Bulk modulus seismic attribute volume for Well 1 generated at χ value of 12°.

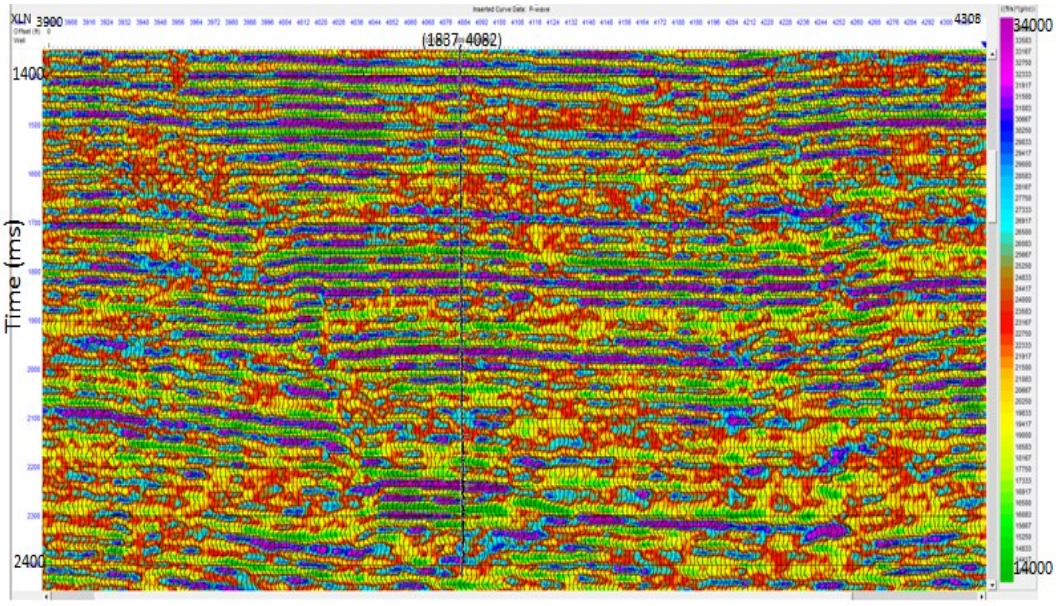

Figure 5.15: Shear modulus seismic attribute volume for Well 1 generated at χ value of −51.3°.

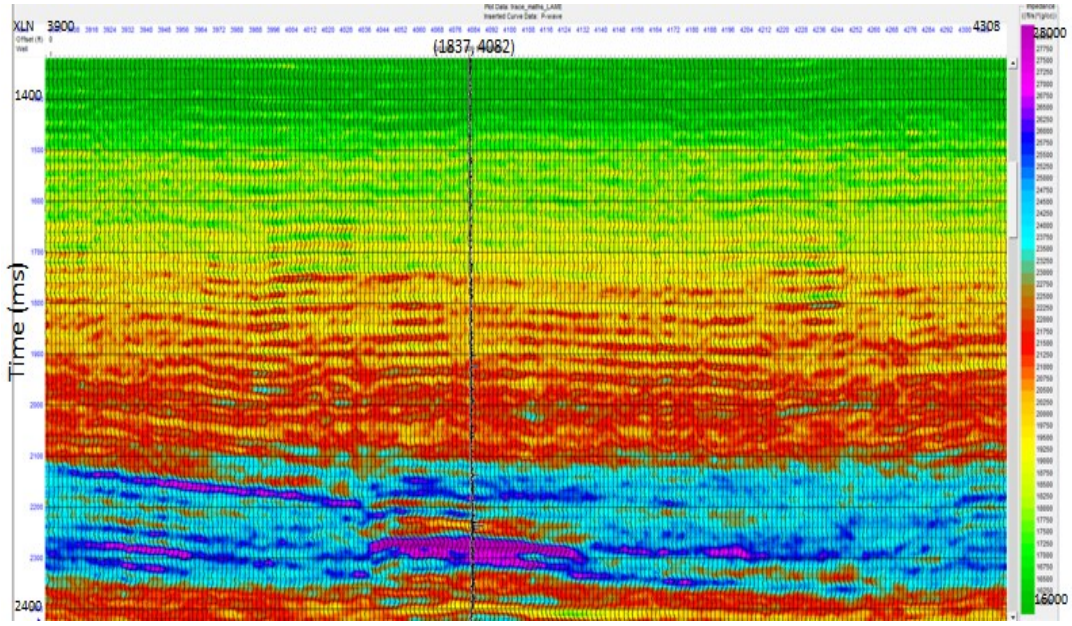

Figure 5.16: Lamé constant (λ) seismic attribute volume for Well 1 generated at χ value of 20°.

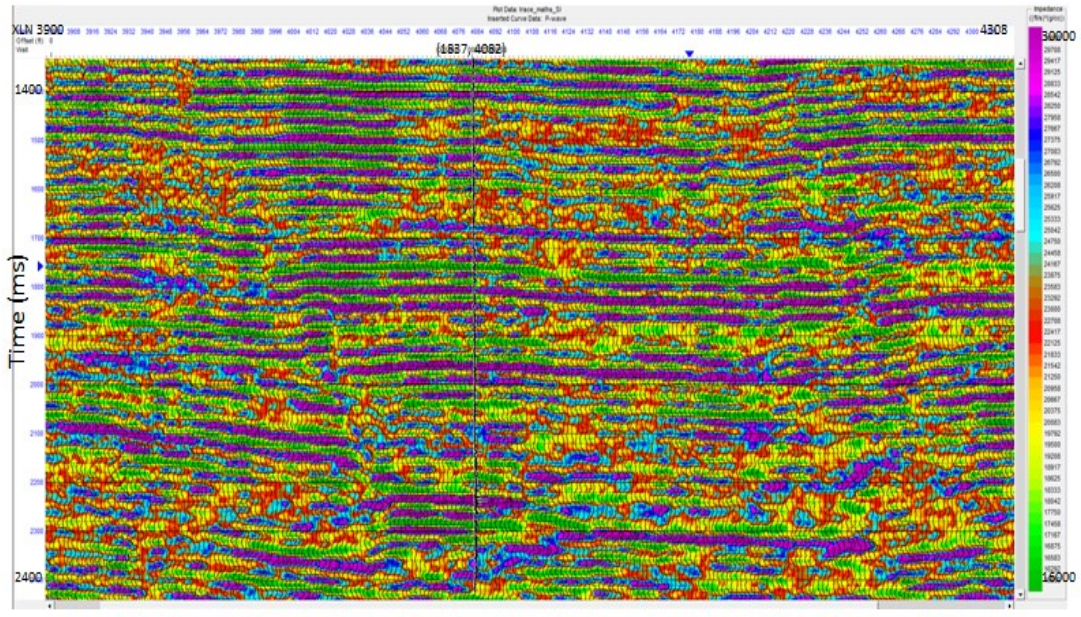

Figure 5.17: Shear impedance seismic attribute volume for Well 1 generated at χ value of −45°.

STEP 4:

A. There is a need for the calibration of the seismic attributes (field data) generated in time (t) to the ones in depth (z). To achieve this, the depth-time curve generated with the corrected P-wave curve after the well-to-seismic tie is used. The equivalent two-way time for each of the depth values in the zone of interest (6300–9000 ft) is determined. A curve of each of the seismic attributes (derived from the well log in STEP 1A) against the equivalent time is then generated. There are two problems associated with this, first, the number of data points in the depth domain is more than the ones in the time domain (different frequency contents) and second, the numerical values of each of the seismic attributes (field data) in the time domain is greater than the ones in the depth domain.

   (i) To solve the first problem, the value of a seismic attribute (derived from the well-log in STEP 1A) at a particular time is derived by taking the average of the same attribute over a certain depth range (equivalent time range). Then, the mean (m_z) and standard deviation (σ_z) of each of the new seismic attribute is determined in the zone of interest.

   (ii) The second problem is solved by normalizing the seismic attributes (field data) from 3D to the seismic attribute (well-log curves) from step 4A(i). This is achieved by using the equation below, an example is shown for the bulk modulus:

$$Knorm(t) = [(K(t) - m_t)/\sigma_t]*\sigma_z + m_z \qquad 5.19$$

B. To check the accuracy of the seismic attributes curves generated in step 4A(i) above, a smoothed curve is generated. There is a difference in frequency content between the seismic attributes from 4A(i) and its equivalent in depth as seen in their different number of data points because data from the well are sampled at every 1 ft (~0.3048 m) while the ones from seismic are sampled at every 6 ms. Hence, the attributes from the well is smoothed to the ones from the seismic to generate new seismic attribute curves. A smoothing function equal to 30 ms is used.

STEP 5:

A. Curves from STEP 4B (smoothed curve), 4A(i) i.e. $\alpha/\beta(t)$, K(t), SI(t), MU(t), $\lambda(t)$ and 1A (plotted in equivalent time) are then plotted together. Figure 5.18 shows the results.

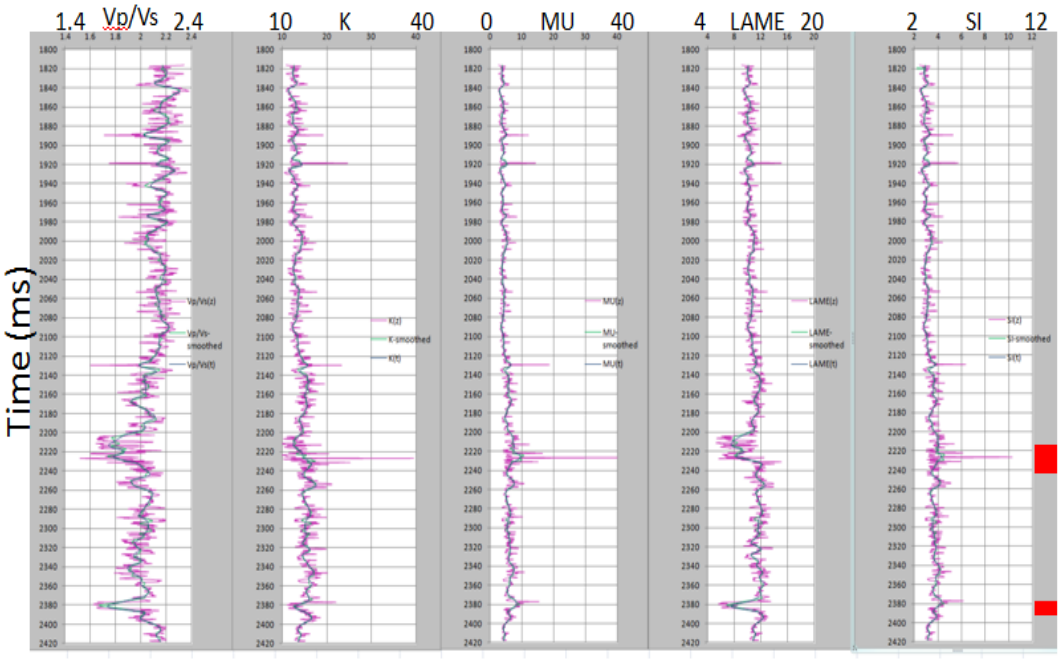

Figure 5.18: Comparison of attributes derived from well log data in time equivalent (purple color), attributes smoothed in STEP 4B (green color) and attributes (well-log curve) from 4A(i) (blue color). The red rectangles represent the hydrocarbon zones (Well 1).

B. Curves from STEP 4A(i) and 4A(ii) i.e. α/β-seis, K-seis, SI-seis, MU-seis, and λ-seis are also plotted together to see the fit. This is shown below:

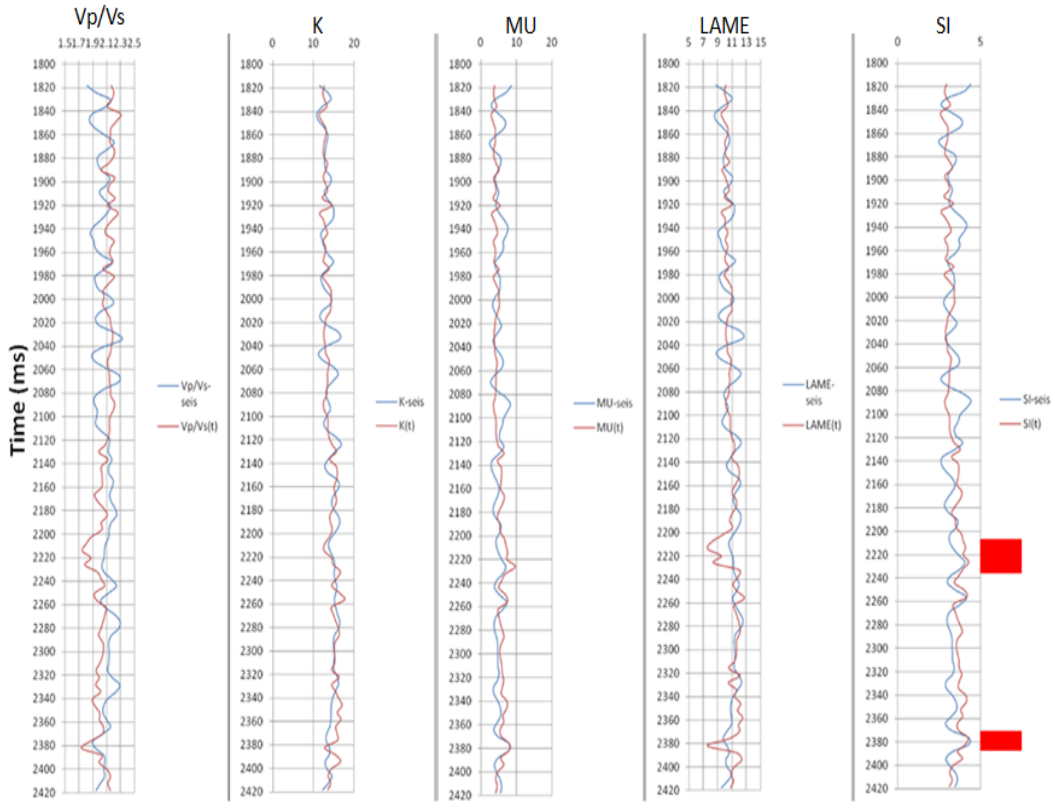

Figure 5.19: Comparison of seismic attributes derived from the seismic field data (blue color) to the ones derived from the well-log curve in time (red color) in Well 1.

5.3 Comparison of different inversion methods

The different inversion methods have certain advantages over each other and each one also has their own errors. The two inversion methods I used in this research are elastic impedance inversion and extended elastic impedance inversion. Elastic impedance has its advantages especially in an environment with a class 2 AVO anomaly where acoustic impedances of gas-saturated sand and surrounding shale are approximately equal. The elastic impedance volume that I generated at the near angle (8.5°) fails to discriminate between the reservoir sand and the shale surrounding it (Figure 5.5) while the elastic impedance volume generated at far angle (28.5°) was able to discriminate between the gas-saturated reservoir and the shale surrounding the reservoir (Figure 5.6)

The second method of inversion used in this research is the extended elastic impedance inversion. This method helps to provide a maximum discrimination between fluids and lithology and thus gives a better characterization of a reservoir. The method achieves this by modifying the definition of elastic impedance beyond the range of physically meaningful angles which ranges between -90° and +90° (Whitcombe et al, 2002). This technique helps to concentrate on the reservoir and thus optimize the lithology and fluid content of a reservoir. The EEI results will be presented in the next section.

CHAPTER 6

DISCUSSIONS AND CONCLUSIONS

6.1 Discussions

In the course of this research, High Island data (seismic and well logs) have been investigated for hydrocarbons using 3D seismic interpretation methods, well-log analysis, AVO modeling, and analysis by elastic impedance inversion and extended elastic impedance inversion methods.

Three-dimensional interpretations of the seismic data show the structural features of the reservoir and the study area in general. In this research, I did a careful inspection of the seismic data provided and identified prospective reservoirs by looking at anomalies on both near and far-angle stacks and correlating these anomalies to available well-log data. Due to the type of AVO anomaly (Class 2) observed in my study area and the characteristic large amplitudes on the far offsets as compared to the near offsets, I picked three horizons on both near- and far-angle stacks. These horizons were picked on all inlines and crosslines of the 3D seismic data. In picking these horizons, I had to identify the different faults in the area and this helped to guide me in mapping the horizons across fault planes. Using these horizons and faults, I generated three surfaces which are in turn used to create the root-mean-square (RMS) amplitude attribute (Figures 3.8 to 3.13). Figures 3.8 and 3.9 show the variations in amplitude on both near- and far-angle stacks and as expected larger amplitudes are observed on the far seismic as compared to the near seismic at Well 1. Also, I interpreted the different faults that bound the reservoir thereby, acting as traps for the hydrocarbon in the reservoir. I generated another attribute, variance which is an edge detector and helps to map faults better.

The reservoir sands at Well 1 have an average thickness of about 31ft (~9 m) and they are characterized by low bulk densities, high relative P-wave velocities with respect to surrounding

shale, higher resistivities, S-wave velocities, and porosities compared to the overlying shale. The cross-over effect of the neutron porosity and density porosity logs shows that the reservoir is a gas-saturated sand. The acoustic impedance logs I generated for both wells could not differentiate the gas-saturated reservoir from the surrounding shale, hence, I generated elastic impedance logs between 0° and 40° which helped to delineate the gas-saturated reservoir better.

Fluid substitution also shows how the reservoir properties change with the presence of different fluids. The addition of brine to the reservoir increases density and P-wave velocity and slightly decreases S-wave velocity (Figures 4.12 and 4.13). AVO modeling in the presence of gas increases the amplitude with offsets/angle. The amplitude variations with offset observed are typical of a Class 2 environment. Initial AVO models generated for gas- and brine-charged reservoir in Well 1 and Well 2 using the Hampson-Russell software did not show any appreciable difference between the gas- and brine-saturated AVO signatures. Detailed modeling using the TIPS software was able to show a clear distinction between the gas-charged and brine-charged reservoir of the two wells (Figures 4.20, 4.21, and 4.22). In-situ gas-saturated AVO model shows an increase in amplitude with offset (Figures 4.20, 4.21, and 4.22).

Elastic impedance and extended elastic impedance inversions were carried out to help identify and confirm Well 1 and Well 2. Two different wavelets (near and far) are subsequently extracted at each well. A low-frequency model is built initially before conducting an inversion on the whole seismic data, as this is required because of the disparity in frequency contents of well log and seismic data. Elastic impedance volumes were generated at both near and far offsets/angles. The near-angle stack was inverted to generate elastic impedance volume at 8.5° (EI_NEAR) while the far-angle stack was inverted for elastic impedance volume at 28.5° (EI_FAR). These volumes were generated separately; the elastic impedance volume at near angle requires the near wavelet for its inversion while the volume generated at far angle requires the far

wavelet. The EI_FAR volume delineates the hydrocarbon reservoir better than the EI_NEAR volume, the hydrocarbon reservoirs are located at 2240 ms and 2380 ms on the EI_FAR volume (Figures 5.5 and 5.6); this supports what Patrick Connolly said in his 1999 paper. This elastic impedance inversion method is very useful in a Class 2 environment for delineating a hydrocarbon zone because acoustic impedance value of gas sand and surrounding shale is approximately equal and discriminating between them is difficult. Elastic impedance value decreases with increase in offset within a hydrocarbon reservoir. The results from the elastic impedance inversion have showed the importance of conducting an elastic impedance inversion especially in a Class 2 environment where acoustic impedance alone cannot delineate hydrocarbon zones.

Horizon slices between time intervals of 50 ms above and 50 ms below (average time window) Horizon 1 were generated for the two inverted volumes (Figures 6.1 and 6.2). On these two horizon slices, the reservoir bounds are shown by the black dashed lines and as can be seen, the reservoir is better delineated on the EI_FAR slice (Figures 6.1 and 6.2) and this bounded region also correspond to the same area with high amplitude on the amplitude map in Figure 3.15. Finally, I carried out an extended elastic impedance (EEI) inversion in this research. To achieve this, I had to generate EEI logs for the following attributes (V_p/V_s, bulk modulus, Lamé constant, shear modulus, and shear impedance) and to check how accurate these attribute logs are, these new logs are compared to the attribute logs generated from the well. The comparison has a reasonable fit and the logs show the presence of gas in the reservoir intervals (Figures 5.12 and 5.18). Additionally, I generated seismic attribute volumes for these five attributes and their respective horizon slices generated in the time intervals of 50 ms above and 50 ms below (average time window) Horizon 1 are seen in Figures 6.3 to 6.7. Values of V_p/V_s are very low at the reservoir as is expected of a gas-saturated reservoir, values of bulk modulus and Lamé constant (λ) are relatively low as expected in a gas zone, all these three attributes (V_p/V_s, bulk

modulus and Lamé constant) are indicative of fluid type. Shear modulus and shear impedance values are high as is expected for this reservoir, these two attributes are in turn indicative of lithology. Figure 6.8 shows seismic attribute volume of shear modulus with gamma-ray curve inserted, it is observed that regions with low gamma-ray readings indicating sand units corresponds with high shear modulus values while regions with low shear modulus values have high gamma-ray readings indicative of shale units especially around the reservoirs. The reservoir is bounded by black dashed lines on all the horizon slices of the five seismic attributes (Figures 6.3 to 6.7) and the bounded area corresponds to the same region with high amplitude on the amplitude map in Figure 3.15.

All of the above (3D seismic data interpretation, well-log analysis, AVO modeling, fluid substitution, elastic impedance inversion, and extended elastic impedance inversion) have helped to discriminate the gas zones. This has increased one's confidence of the presence of hydrocarbon zones.

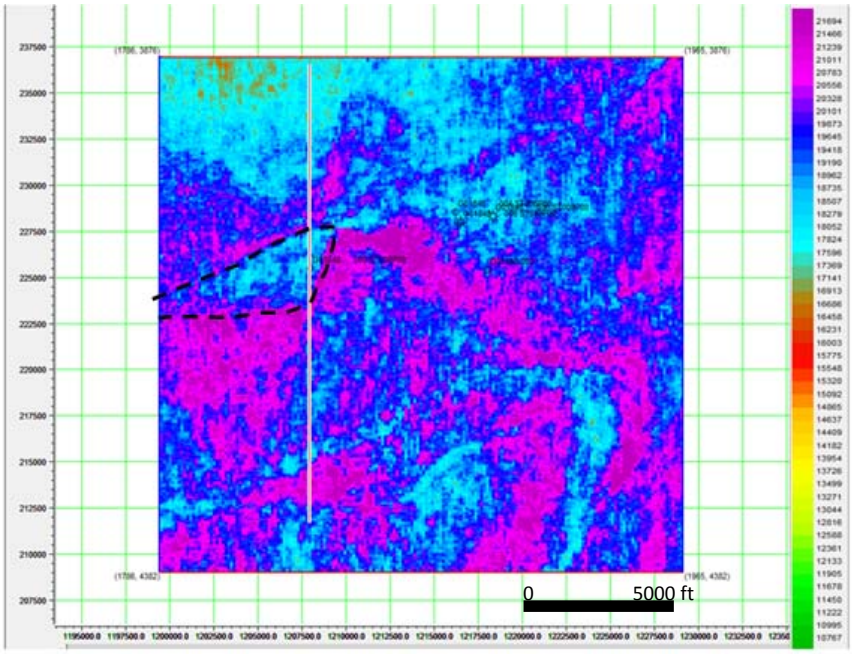

Figure 6.1: Horizon map through Horizon 1 of near-angle elastic impedance volume (Well 1).

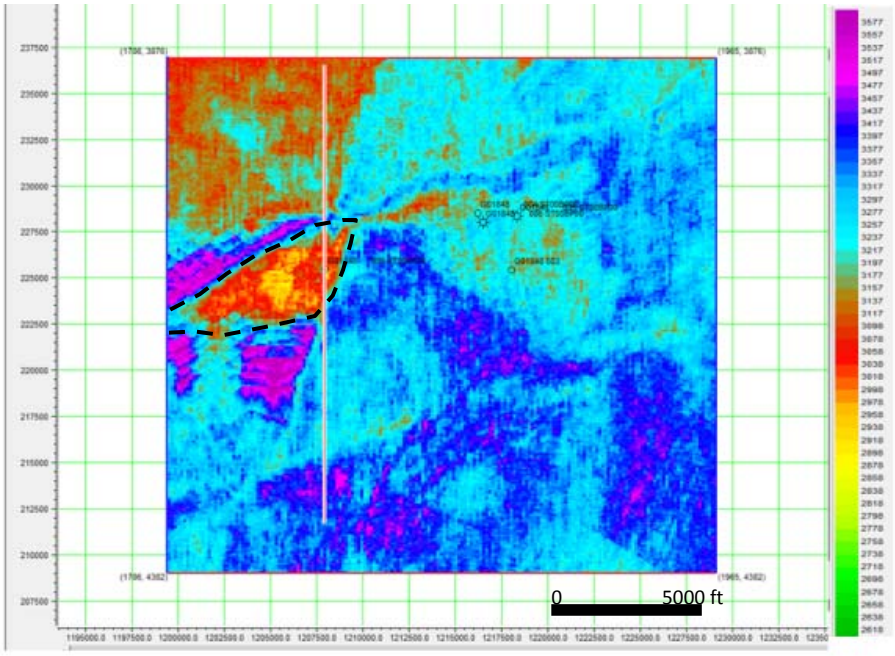

Figure 6.2: Horizon map through Horizon 1 of far-angle elastic impedance volume (Well 1).

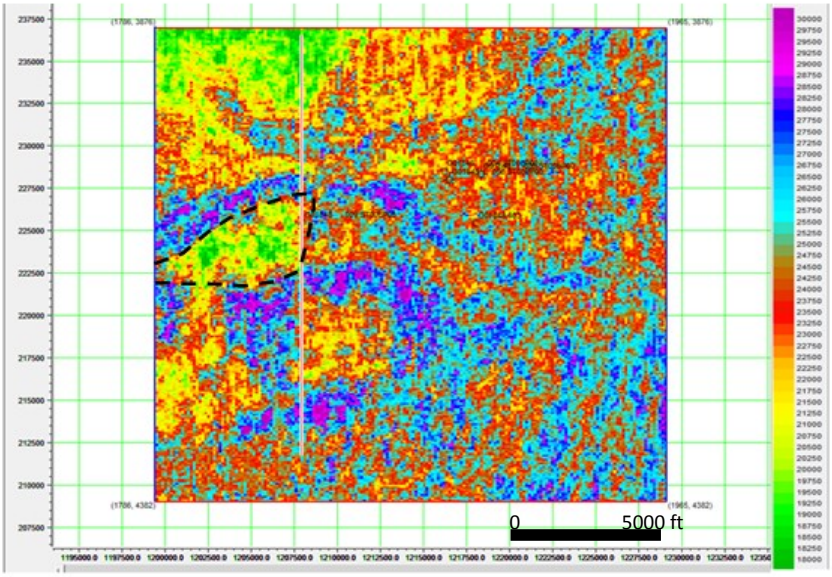

Figure 6.3: Horizon map through Horizon 1 of V_p/V_s seismic attribute volume (Well 1).

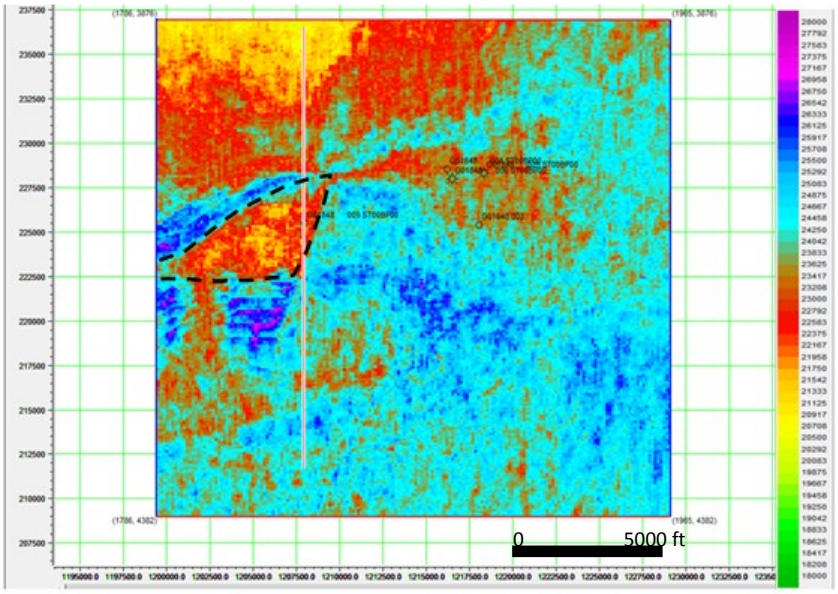

Figure 6.4: Horizon map through Horizon 1 of Lamé seismic attribute volume (Well 1).

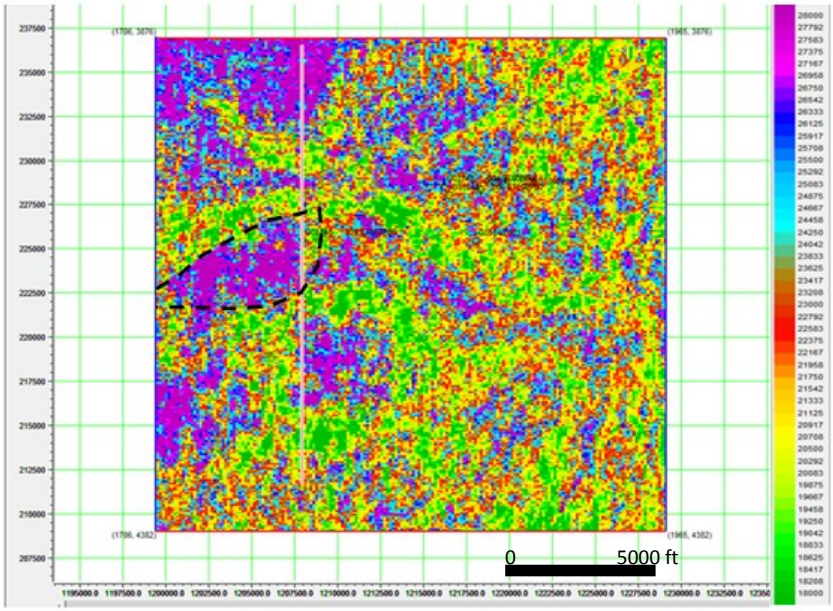

Figure 6.5: Horizon map through Horizon 1 of shear modulus seismic attribute volume (Well 1).

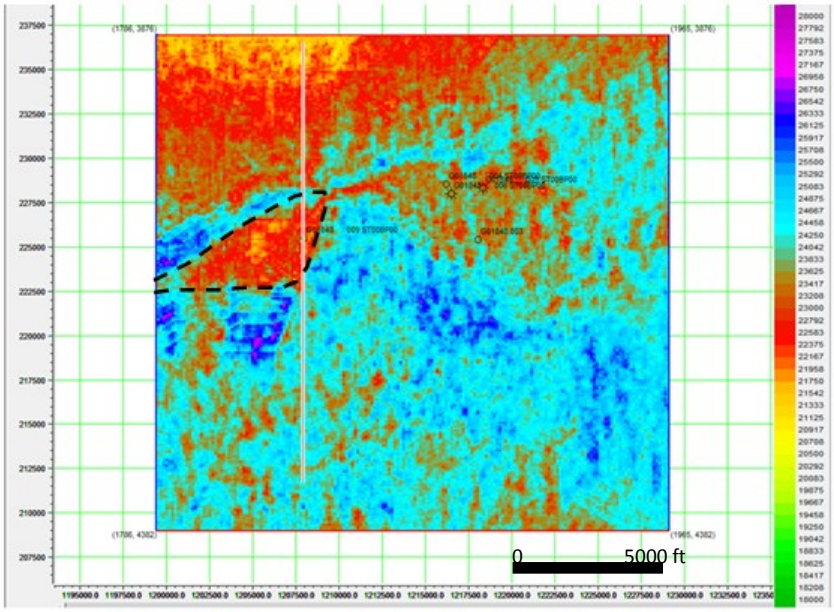

Figure 6.6: Horizon map through Horizon 1 of bulk modulus seismic attribute volume (Well 1).

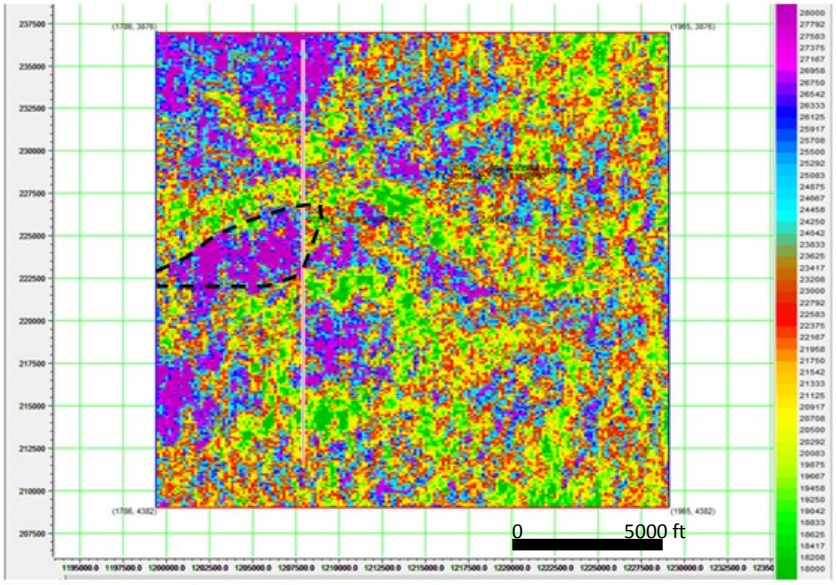

Figure 6.7: Horizon map through Horizon 1 of shear impedance seismic attribute volume (Well 1).

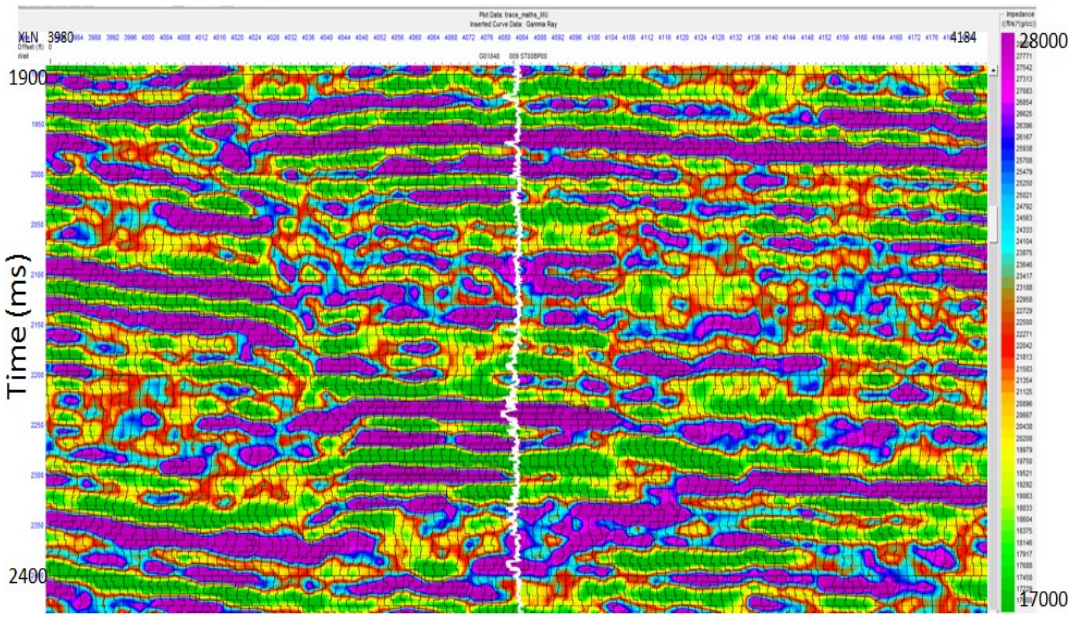

Figure 6.8: Shear modulus seismic attribute volume (Inserted white curve is gamma ray).

6.2 Conclusions

Elastic impedance logs at non-zero angles of incidence delineate gas-saturated reservoirs better as compared to elastic impedance log at an incident angle of zero degree (acoustic impedance log), hence, elastic impedance attribute helps in delineating a gas-saturated reservoir better than acoustic impedance attribute in a Class 2 environment.

Amplitude anomalies observed on seismic data were analyzed and it was determined that these anomalies were a response to the hydrocarbon present in the reservoirs. Comparison of results from fluid substitutions for gas and brine and detailed AVO synthetic models for brine- and gas-saturated reservoirs somewhat confirmed this.

Elastic impedance seismic volume generated at 28.5° and the horizon slice from this volume show a better delineation of the gas-saturated reservoir than the elastic impedance seismic volume generated at 8.5° and the respective horizon slice.

The five seismic attribute volumes (bulk modulus, V_p/V_s, Lamé, shear modulus, and shear impedance) generated from the extended elastic impedance equation and their respective horizon slices help to show a better characterization of the reservoir and hence, the determination of the reservoir's lithology (as seen on the shear modulus and shear impedance attribute volumes and horizon slices) and predicting its pore-fluid type (as seen on the V_p/V_s, bulk modulus and Lamé attribute volumes and horizon slices).

REFERENCES

Aki, K., and P. G. Richards, 1980, Quantitative Seismology-Theory and Methods, 1: W.H. Freeman and Company.

Asquith, G., and D. Krygowski, 2004, Basic Well Log Analysis: The American Association of Petroleum Geologists.

Batzle, M., and Z. Wang, 1992, Seismic properties of pore fluids: Geophysics, **57**, 1396-1408.

Berryman, J. G., P. A. Berge, and B. P. Bonner, 2002, Estimating rock porosity and fluid saturation using only seismic velocities: Geophysics, **67**, 391-404.

Boorman, C., M. Cowgill, E. Ginal, R. Mandley, J. Thompson, G. Roberts, and S. Archer, 2006, Huge potential still waiting in the Gulf of Mexico: GEO Expro Issue No. 4/5.

Bortfeld, R., 1961, Approximation to the reflection and transmission coefficients of plane longitudinal and transverse waves: Geophysics Prospecting, **9**, 485-503.

Brown, A. R., 2004, Interpretation of three-dimensional seismic data (6^{th} edition), AAPG Memoir 42 and SEG Investigations in Geophysics 9: AAPG and SEG.

Castagna, J. P., M. L. Batzle, and R. L. Eastwood, 1985, Relationships between compressional-wave and shear-wave velocities in clastic silicate rocks: Geophysics, **50**, 571-581.

Castagna, J. P., and H. W. Swan, 1997, Principles of AVO crossplotting: The Leading Edge, **4**, 337-342.

Castagna, J. P., H. W. Swan, and D. J. Foster, 1998, Framework for AVO gradient and intercept interpretation: Geophysics, **63**, 984-956.

Chiburis, E., C. Frank, S. Leaney, S. Mchugo and C. Skidmore, 1993, Hydrocarbon detection from AVO: Oilfield Review January ed., 42-50.

Connolly, P., 1999, Elastic impedance: The Leading Edge, **18**, 438-452.

Domenico, S. N., 1976, Effect of brine-gas mixture on velocity in an unconsolidated sand reservoir: Geophysics, **41**, 882-894.

Encarta. (2011). Accessed February 18, 2011, from http://encarta.msn.com/dictionary/attribute.

Fatti, J. L., G. C. Smith, P. J. Vail, P. J. Strauss, and P. R. Levitt, 1994, Detection of gas in sandstone reservoirs using AVO analysis- A 3-D case history using Geostack technique: Geophysics, **59**, 1362-1376.

Francis, A., 2002, Deterministic Inversion – Overdue for Retirement?: Petroleum Exploration Society of Great Britain (PETEX) 2002 conference, 1-8.

Geophysical Society of Houston (various authors), 1973, Lithology and direct detection of hydrocarbons using geophysical methods.

Gidlow, P. M., G. C. Smith and P. J. Vail, 1992, Hydrocarbon detection using fluid factor traces: A case history: Presented at the Joint Society of Exploration Geophysicists/EAGE Summer Research Workshop on "How useful is amplitude-versus-offset (AVO) analysis?", 78-89.

Gluyas, J., and R. Swarbrick, 2004, Petroleum Geosciences: Blackwell Publishing Company.

Greenberg, M. L., and J. P. Castagna, 1992, Shear-wave velocity estimation in porous rocks: Theoretical formulation, preliminary verification and applications: Geophysical Prospecting, **40**, 195-210.

Hamada, G. M., M. S. Al-blehed and M. N. J. Al-Awad, 2000, Nuclear magnetic resonance log evaluation of low resistivity sandstone reservoirs by-passed by conventional logging analysis: Society of Petroleum Engineers International, SPE 64406, 1-11.

Hendrickson, J. S., 1999, Stacked: Geophysics Prospecting, **47**, 663-706.

Hilterman, F., 2001, Seismic Amplitude interpretation, SEG/EAGE 2001 Distinguished Instructor Short Course No. 4: Society of Exploration Geophysicists.

Hilterman, F. J., and L. Liang, 2003, Linking rock property trends and AVO equation to GOM deep-water reservoirs: 73rd Annual meeting of Society of Exploration Geophysicists, Expanded Abstracts, 211-214.

Hilterman, F. J., J. W. C. Sherwood, R. Schellhorn, B. Bankhead, and B. DeVault, 1998, Identification of lithology in the Gulf of Mexico: The Leading Edge, **17**, 215-222.

Koefoed, O., 1955, On the effect of Poisson's ratios of the rock strata on the reflection coefficients of plane waves: Geophysics Prospecting, **3**, 381-387.

Latimer, R., R. Davidson, and P. vanRiel, 2000, An interpreter's guide to understanding and working with seismic-derived acoustic impedance data: The Leading Edge, **19**, 242-256.

Li, Xin-G, D. H. Han, J. Liu, and D. McGuire, 2005, Inversion of S_w and porosity from seismic AVO: SEG Expanded Abstracts, 1307-1310.

Liner, C. L., 2004, Elements of 3D Seismology (2nd edition): Pennwell Corporation.

Lumley, D. E., 1993, Angle-dependent reflectivity estimation: SEG Expanded Abstracts, **12**, 746-749.

MMS. (2001). Accessed May 14, 2011, from www.gomr.mms.gov.

Ostrander, W. J., 1984, Plane-wave reflection coefficient for gas sand at non-normal angles of incidence: Geophysics, **49**, 1637-1648.

Ross, C. P., 2000, Effective AVO cross-plot modeling: A tutorial: Geophysics, **65**, 700-711

Russell, B., 2005, Strata workshop: theory and exercises in seismic inversion and AVO, unpublished lecture notes.

Russell, B., and D. Hampson, 1999, AVO theory: Hampson-Russell software services limited.

Russell, B., and D. Hampson, 2006, the old and the new in seismic inversion: CSEG Recorder, 5-11.

Russell, B., K. Hedlin, F. J. Hilterman, and L. R. Lines, 2003, Fluid-property discrimination using Lame petrophysical parameters; "λρ", "μρ", and "λ/μ" fluid stack from P and S inversions; 67th Annual International Meeting, SEG, Expanded Abstracts, 183-186.

Rutherford, S. R., and R. H. Williams, 1989, Amplitude versus offset variations in gas sands: Geophysics, **54**, 680-688.

Savic, M., Verwest, B., Masters, R., Sena, A., and Gingrich, D., 2000, Elastic impedance inversion in practice: SEG Expanded Abstracts, **19**, 689.

Selley, R., 1985, Elements of Petroleum Geology: W. H. Freeman and Company.

Sen, M. K., 2006, Seismic Inversion: Society of Petroleum Engineers.

Sheriff, R. E., 2002, Encyclopedic Dictionary of Applied Geophysics (4th edition): Society of Exploration Geophysicists.

Shuey, R. T., 1985, A simplification of the Zoeppritz equations: Geophysics, **50**, 609-614.

Slatt, R. M., 2006, Stratigraphic reservoir characterization for Petroleum Geologists, Geophysicists and Engineers: Handbook of Petroleum Exploration and Production, Volume 6.

Smith, G. C., and P. M. Gidlow, 1987, Weighted stacking from rock property estimation and detection of gas: Geophysics prospecting, **35**, 993-1014.

Smith, G. C., and R. A. Sutherland, 1996, The fluid factor as an AVO indicator: Geophysics, **61**, 1425-1428.

Smith, T. M., C. H. Sondergald and C. S. Rai, 2003, Gassmann fluid substitutions: A tutorial, Geophysics, **68**, 430-440.

Trietel, S., and L. Lines, 2001, Past, present and the future of geophysical inversion-a new millennium analysis: Geophysics, **66**, 21-24.

Veeken, P. C. H., 2007, Seismic stratigraphy, basin analysis and reservoir characteristics, in Helberg, K., and Trietel, S., ed.: Handbook of Geophysical Exploration: Seismic Exploration, **37**, 509.

Verm, R., and F. Hilterman, 1995, Lithology color-coded seismic sections, The calibration of AVO crossplotting to rock properties: The Leading Edge, **14**, 847-853.

Wang, Z., 2001, Fundamentals of seismic rock physics: Geophysics, **66**, 398-412.

Widess, M. B., 1973, How thin is a thin bed?: Geophysics, **38**, 1176-1180.

Whitcombe, D. N., P. A. Connolly, R. L. Reagan and T. C. Redshaw, 2002, Extended elastic impedance for fluid and lithology prediction, Geophysics, **67**, 63-67.

Zhou, Z., F. Hilterman, H. Ren, and M. Kumar, 2005, Water saturation estimation from seismic and rock-property trends: 75th Annual International Meeting, SEG Expanded Abstract, 258-261.

Zhou, Z., and F. Hilterman, 2010, A comparison between methods that discriminate fluid content in unconsolidated sandstone reservoirs, Geophysics, **75**, 47-58.

Zimmerman, C. J., and R. E. Duren, 1992, Using the Seismic Range Equation (SRE) for AVO analysis to detect low gas saturation: SEG Expanded Abstracts, 852-855.

Zoeppritz, K., 1919, Erdbebenwellen VIIIB, On the reflection and propagation of seismic waves: Gottinger Nachrichten, I, 66-84.

Worldatlas. (2011). Accessed 27 June, 2011, from www.worldatlas.com/aatlas/infopage/gulfofmexico.